PROPERTIES OF EXTENSIVE AIR SHOWERS AROUND 10^{17} EV

BY

MATTHEW JOHN KIDD

B.S., California Institute of Technology, 1990

THESIS

Submitted in partial fullfilment of the requirements
for the degree of Doctor of Philosophy in Physics
in the Graduate College of the
University of Illinois at Urbana-Champaign, 1997

Urbana, Illinois

PROPERTIES OF EXTENSIVE AIR SHOWERS AROUND 10^{17} EV

Matthew John Kidd, Ph.D.
Department of Physics
University of Illinois at Urbana-Champaign, 1997
Tom A. O'Halloran, Advisor

2516 quality extensive air showers (EAS) were observed in coincidence using the HIRES nitrogen fluorescence detector and the CASA–MIA ground array within the energy range $10^{16.7}$–$10^{17.9}$ eV. Arrival direction, energy, location of muon content, and $X_{\max}$ were determined for each event. A predominantly heavy composition was found over the entire energy range. The muon multiplicity and lateral distribution function (LDF) out to 1200 meters were determined and found to be in good agreement with results from AKENO. The measured energy dependence of the LDF is modest.

Acknowledgements

I want to especially thank Brian Fick of the CASA–MIA collaboration. Without his help and persistence in realizing joint physics from the HIRES and CASA–MIA detectors, this work would not have been possible. I am also grateful to Brian Newport who always had an answer to every question, no matter how technical, about the CASA–MIA array. David Bird deserves a great deal of credit for kicking the HIRES Prototype into shape and laying the groundwork for joint data collection. And without Tom O'Halloran to kick me along, I might still be writing.

I want to thank the many members of the HIRES collaboration. They have spent more than enough cold nights on the hill collecting data. I give special thanks to Hongyue Dai, who explained several analysis issues in detail. Many thanks also to the CASA–MIA collaboration.

Finally, I thank Molly for understanding that just five minutes in front of a computer usually means an hour.

This material is based upon work supported by the National Science Foundation under grants PHY 93-22298, PHY 93-21949, PHY 95-12810, and by Department of Energy grants DE AC02 ER01195 and DE FG0291 ER40677.

Contents

List of Tables

List of Figures

Chapter 1

Introduction

Below 10^{14} eV, balloon and satellite experiments are able to directly measure the cosmic rays. The JACEE[20] detector has made direct measurements up to $10^{14.6}$ eV, although the statistics are very low above 10^{14} eV. Above 10^{15} eV, the cosmic ray flux is so low that direct measurement is no longer possible. The detection methods used above 10^{15} eV are all indirect. They include ground arrays, atmospheric fluorescence detection, and air Cherenkov detection. Each of these techniques measures some aspect of the of extensive air shower (EAS), which results from the impact of the primary with the upper atmosphere. From this indirect evidence, the direction, energy, and composition of the primary are determined as well as possible. General EAS behavior is also studied.

Ground arrays and atmospheric fluorescence have strikingly different advantages and disadvantages. Air fluorescence detectors measure energy well and do a fair job determining the composition and arrival direction of the primary. Ground arrays measure the arrival direction well and do a fair job determining the composition, but measure the energy very poorly. Traditionally ground arrays have relied on large statistics, whereas fluorescence detectors try to characterize each of the limited number of high energy events quite well. It is notable that the two detection methods use rather different techniques to measure energy and composition.

The HIRES fluorescence detector overlooks the CASA ground array and its companion, the buried MIA muon ground array. This is the first time an air fluorescence experiment has

been operated in coincidence with a ground array. This makes it possible to directly cross check composition and energy measurements. Furthermore, other shower properties can be more accurately determined by combining information from the two detectors. This thesis describes the analysis of some 2500 quality HIRES–MIA coincident events over the energy range $10^{16.7}$–$10^{17.9}$ eV.

1.1 The detectors

The overriding factor in designing cosmic ray detectors is the steeply falling cosmic ray spectrum. Roughly speaking, the differential flux $\sim E^{-3}$. In order to maintain the same detection rate a decade higher in energy, a cosmic ray detector must have 500–1000 times the collection area. Although this expansion in collection area can not be maintained all the way from 100 MeV to 10^{20} eV (10 EeV), the increasing size of the resulting EAS, which allows detection over a large area, makes various higher energy experimental techniques practical. While a balloon flown experiment has a typical collection area of 1 m^2, ground arrays have reached $\sim 10^6$ m^2. The proposed giant Auger ground array plans to cover 3×10^9 m^2 in each hemisphere. Unlike ground arrays which trigger directly on the EAS particles, nitrogen fluorescence detectors trigger on the istropically emitted fluorescence light. This allows detection of distant EAS. A full 2π steradian sky coverage air fluorescence detector can easily achieve 10^9 m^2 collection around 10^{18} eV (1 EeV). The same detector will have an even greater collection area for higher energy events which can be seen further away.

All ground arrays measure particle number and arrival time near the ground. A sufficiently high coincidence within a small time window indicates the particles belong to an EAS generated by an incoming cosmic ray. Some ground arrays include counters a few meters below the surface to isolate the penetrating muons from electrons and photons. Typical detector spacing is 10-100 meters with each detector having an active area on the order of 1 m^2. Shower direction is determined by fitting the arrival time of particles to a plane, with

various refinements possible. Determining the shower energy and composition is a more complicated process which will be discussed in detail later.

Many ground arrays have been built. The earliest effort was Volcano Ranch [53] which was built by the University of New Mexico. They showed the cosmic ray spectrum extended to at least 10^{19} eV. Other early ground arrays were Haverah Park [51], Sydney (SUGAR)[72], and Yakutsk [50]. The coverage of these arrays varies but all have fewer than 100 detector stations. The most recent ground arrays include Akeno which in turn is part of the larger AGASA[40] and the Chicago Air Shower Array (CASA) [12]. They have increased the number of detectors by an order of magnitude.

The Chicago Air Shower Array/Michigan Array, CASA/MIA, was designed for TeV gamma ray astronomy. It consists of a surface array (CASA) and a ground array (MIA). The muon array is used to identify muon poor events which are candidates for photon initiated air showers. Typical CASA arrival direction resolution is 0.5 degrees. Although CASA has not identified any sources, it has established upper limits for the gamma ray flux from the Crab Nebula [13], Cygnus X3 and Hercules X1 [14], the galactic plane [17], and supernova remnants [15]. The large quantity and overall quality of the CASA/MIA dataset casts considerable doubt on reported sources from other arrays with smaller collection areas and fewer detectors.

The basic design of CASA/MIA is well described in several locations [12, 49, 47]. Very briefly, CASA consists of 1089 detector stations, 1.49 m^2, laid out in a 0.25 km^2 grid. Each station consists of 4 counters with a 6-bit ADC. MIA consists of 1024 muon counters, grouped in 16 patches of 64, buried 3 meters below the surface.

The University of Utah has been a pioneer in the observation of cosmic rays via nitrogen fluorescence. The Fly's Eye detector [4] took data from 1982 to 1992, with a companion detector for stereo tracking completed in 1986. Fly's Eye was able to measure the spectrum and rough composition as well as look for anisotopy. These results are discussed further in the next chapter. The HIRES prototype detector was an upgraded successor to the

Fly's Eye, en route to a system of two or more full HIRES detectors. This prototype was built to overlook CASA/MIA situated 3.3 km away with the hope that interesting physics would result during the prototype phase from the coincident events. In short, the HIRES prototype detector consisted of 14 mirrors with 256 phototubes arranged in the focal plane of each mirror.

The HIRES and MIA/CASA detectors are not a well matched set for two reasons. Built for gamma ray astronomy, CASA is sensitive over the range 10^{14}–10^{17} eV, with saturation beginning at the high end. HIRES sensitivity begins somewhat below 10^{17} eV, being limited by the low intensity of the fluorescence light emitted by smaller air showers. Second, the optimal muon detector spacing for coincident studies would be about twice the current spacing. Fortunately, the muon lateral distribution function (LDF) rolls off more slowly with distance than the electron LDF. This means there are many events which trigger MIA even though the shower core falls outside the array, at the same time avoiding counter saturation. The result is about one decade in energy of useful overlap.

Chapter 2

Introduction to Cosmic Ray Physics

Cosmic Ray Physics has traditionally been the haunt of those seeking higher energies than those available at particle accelerators and those in search of unique astrophysical information. Both the positron and the muon were first found in cosmic ray tracks. Particle multiplicities, notably the electromagnetic (e±, γ) to muon ratio have long been studied by ground arrays. The highest energy p-air inelastic cross section, σ^{inel}_{p-air}, was estimated by the Fly's Eye detector[21].

Those seeking accelerator like results near or beyond current accelerator energies must contend with several difficulties. The "beam" is neither unidirectional, monoenergetic, nor particularly intense at the energies of interest. Since it is impossible to build an intricate detector around an a priori unknown point of interaction, it is necessary to rely on the detection of the resulting extensive air shower (EAS) in the atmosphere, where the atmosphere acts like a giant continuous calorimeter. The properties of the primary must then be inferred from a rather incomplete knowledge of the debris produced.

The initial impact of the primary with the atmosphere is quite complicated. At the highest energies, it is beyond the energies measured by accelerators. Nevertheless, most of the energy ends up in π^0 and $\pi^\pm$, which are produced in about equal numbers. Almost all $\pi^\pm$ decay via, $\pi^\pm \rightarrow \mu^\pm + \nu$ (99.987%), before reaching the ground, although this may not happen for hundreds of meters owing to time dilation. The muons are readily detectable. Since neutrinos only interact weakly, they have negligible probability of being detected from

subsequent interaction in the remaining air above ground. In calculating primary energy, the energy lost to neutrinos can only be estimated in a model dependent manner. The π^0 decay, $\pi^0 \rightarrow \gamma + \gamma$, begins the electromagnetic cascade. Pair production, $\gamma \rightarrow e^+ + e^-$, and bremsstrahlung, $e^\pm \rightarrow e^\pm + \gamma$, feed the growing EAS. The EAS continues to grow until the dominant energy loss is via ionization rather than bremsstrahlung. The electrons and photons from the electromagnetic cascade are also readily detectable by direct impact. Both the nitrogen fluorescence and the Cherenkov production from the cascading particles have been detected. These latter two detection methods have the advantage of not requiring direct impact of the shower particles with the detector. This allows greater effective spatial coverage.

For astrophysical purposes, the interesting observable quantities are the cosmic ray energy spectrum, the composition, arrival directions, and general anisotropy. The measured spectrum (see Figure 2.1) spans many orders of magnitude and follows a roughly E^{-3} power law. The slope changes from 2.7 to 3.1 between 10^{15} eV and 10^{16} eV is usually called the "knee". The reduction in the slope around 10^{19} eV, is referred to as the "ankle". The spectrum provides clues about the nature of the sources. Both slope changes are attributed to changes in the astrophysical objects accelerating the cosmic rays. Much effort has been made to measure the spectrum, but none of it is central to this thesis.

The composition is well understood by directly measured nuclei up to $\approx 10^{12}$ eV, via balloon launched and satellite experiments. There it tracks solar abundances fairly closely; however, the odd-even effect [16, 55] is not as extreme because spallation enhances the odd nuclei populations. Above 10^{12} eV, the particle flux is too low to measure directly. Therefore, the composition must be inferred from the shower properties. This is quite challenging and not nearly as accurate. Traditionally, the field employs the crude classification of *light* (proton and helium) and *heavy* or *iron*, which is usually taken to mean everything else. Occasionally the carbon, nitrogen, and oxygen range (CNO) is classified as *medium*.

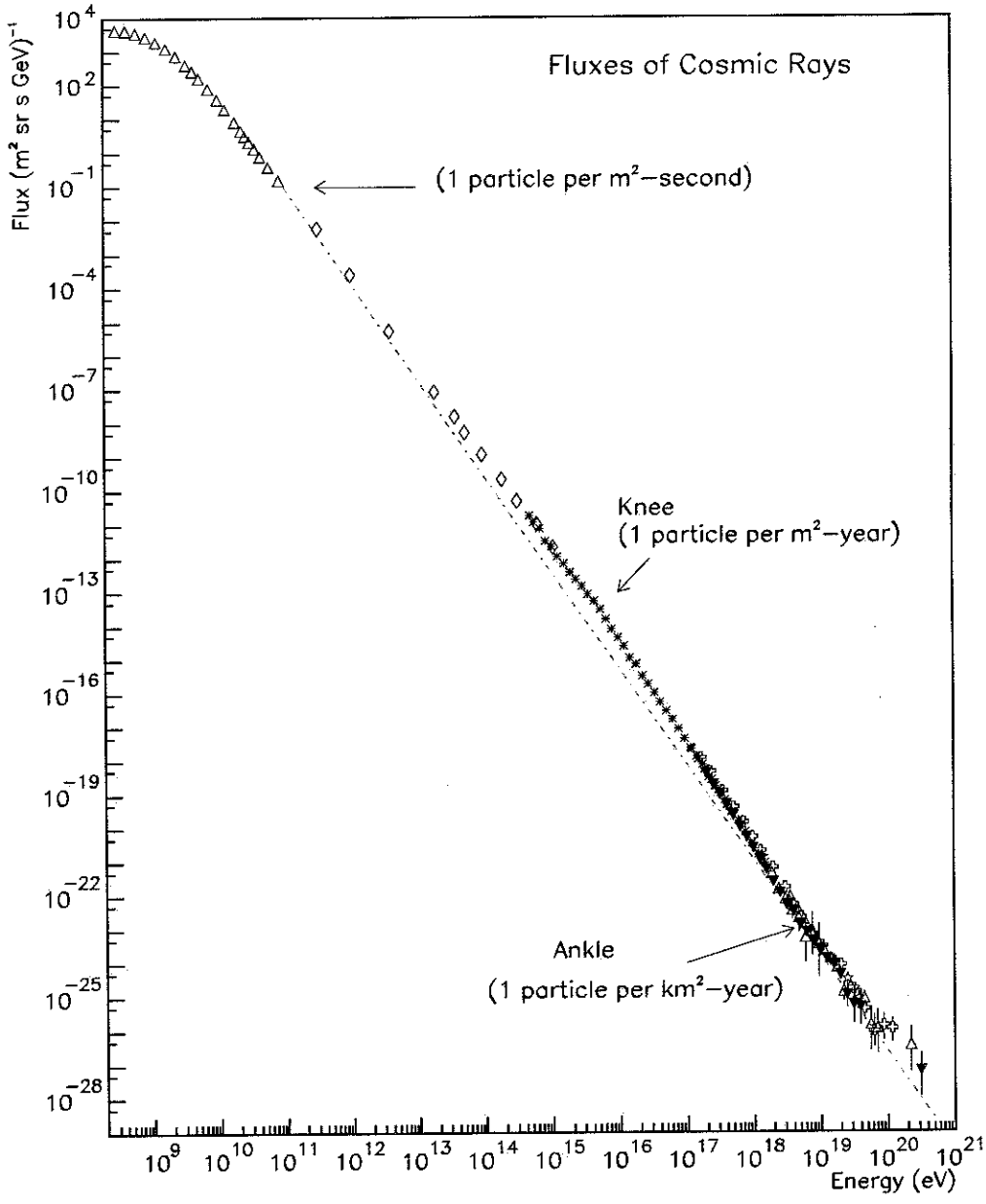

Figure 2.1: Compilation of measurements through 1996 of the differential energy spectrum of cosmic rays. The dotted line shows an E^{-3} power law for comparison. The sparse region 10^{11}–10^{14} eV is the awkward gap between balloon/satellite and ground array data.

The exact origin of cosmic rays remains a mystery. This is because they are charged nuclei and as a result of galactic magnetic fields their source direction becomes unrelated to their arrival direction during their travel to earth. To understand the magnitude of the problem consider a constant magnetic field $\vec{B}$. Then the gyroradius, R_g becomes:

$$R_g = \frac{m\gamma v}{ZeB\ \sin\theta} \tag{2.1}$$

Measurements for the average galactic field using Faraday rotation, the alignment of dust grains, and the Zeeman splitting of the 21-cm neutral hydrogen line yield values of 1–10 $\times\ 10^{-6}$ G, with 3×10^{-6} G taken as a generally representative value [54]. For a 10^{17} eV proton, $R_g \sim 50$ parsecs. This is less than one tenth the thickness of the galactic nucleus. The direction of the magnetic field is known to be variable on distance scales at least that small[56].

The randomizing effects of the magnetic fields limit the cases where it is possible to look for point sources. The first case is that of uncharged particles, i.e. gamma rays and neutrons. In general, the short decay length of neutrons limits their usefulness. High energy gamma rays are more promising. They are readily produced in the acceleration region of cosmic rays. Production from electrons can occur via e^+e^- annihilation, bremsstrahlung radiation, inverse compton scattering, and synchrotron radiation. Production can also occur from nuclei, primarily through the decay of neutral pions produced when the nuclei interact with the surrounding medium.

Gamma ray initiated showers begin immediately with the electromagnetic cascade bypassing almost all of the pion production, and hence the muons. Nevertheless a few muons are produced via processes such as $e^+ + e^- \rightarrow \mu^+ + \mu^-$. In practice it can be difficult to distinguish the few photon induced showers from naturally downward muon fluctuating showers produced by ordinary cosmic rays. Furthermore, the ratio of cosmic rays to gamma rays at a given energy is about 1000. The relative scarcity of photon showers makes statistics a critical issue. Overcoming this problem is vital for CASA and all ground arrays searching

for point sources. Better understanding the muon content of such showers can only improve these efforts.

The second case where point sources may be found is for very high energy cosmic rays with energies of typically at least 10^{19} eV. Two advantages combine here. First, the cosmic rays are deflected less over the same distance. Second, photopion production is expected to become prominent around 3×10^{20} eV. This is called the Greisen–Zatsepin cutoff, which should occur because the 3°K microwave background radiation photons are blueshifted above the pion production threshold in the reference frame of such energetic cosmic rays. The Greisen–Zatsepin cutoff has not been firmly established for lack of sufficient data. The expected interaction length with the microwave background for a 10^{20} eV cosmic is about 30 Mpc. This short length and the limited bending means such high energy cosmic rays should point back to their source within a few degrees.

Because it is so difficult to observe point sources, it is more common to look for large scale anisotropy. Considering the simple model where the galactic magnetic field is basically perpendicular to the galactic plane regardless of local irregularities, one expects cosmic rays to remain generally confined to the galactic plane. This would result in an enhancement from the galactic plane. For lower energy cosmic rays above solar energies no anisotropy is seen. Given the small gyroradius of such particles, this is not unexpected. An early Fly's eye study [3] found no galactic enhancement above 0.4 EeV. Teshima [66] in 1993 reviewed the data above 10^{17} eV. No anisotropy of any type greater than 3σ has ever been reported. Huang[42] analyzed the full Fly's Eye dataset extensively and found no effects beyond 2σ for anisotropy even at the highest energies. Unfortunately, all of these studies are based on a rather limited set of data.

Somewhere around 10^{18} eV, the cosmic ray composition is expected to change. A proton at this energy has a gyroradius $\sim$ 500 parsecs. This is comparable to the thickness of the galactic disk. Particles of such energy should leak out of the galaxy. Since heavy elements have a small gyroradius at the same energy, this should lead to an enhancement

of heavy elements in the transition region. This simple picture is sometimes referred to as the Leaky Box model. Above the transition region, a large fraction of the cosmic rays may be extragalactic in origin. The Fly's Eye group saw evidence for such a transition[6]. The Akeno group found their data did not support such a conclusion[40]. The matter remains unresolved. If the Leaky box hypothesis is true, one might expect an enhancement in the supergalactic plane at very high energies. Huang [42] checked this as well and did not observe any effect, but the Fly's Eye dataset was even more limited at these highest energies.

Chapter 3

Shower Physics

3.1 Electromagnetic Component: X_0 , $X_{\max}$

A good way to understand the fluorescence technique is to view the atmosphere as a giant continuous calorimeter. After the initial impact, the shower builds up as it would in an ordinary calorimeter via pair production and bremsstrahlung, with the number of particles following a standard form. The nitrogen fluorescence, which emits about 4 photons/particle-meter, becomes distinguishable from natural background fluctuations in the sky light, the so called sky noise, above $\sim 10^{16}$ eV.

The energy region of the initial collision is beyond what is accessible with current accelerators. An additional problem is that for air showers the region of importance is the extreme forward region which can not be fully measured in accelerator experiments. Therefore, the initial collision must be based on extrapolated data and is model dependent. Three representative models which have been tried are the KNP model [48], the minijet model [37], and a statistical model [31].

The main difference between these models is the energy dependence of the *inelasticity*. The inelasticity is defined in the laboratory system as the fraction of the energy of an incident particle that is not carried out of the interaction by the fragment of the incident particle (i.e., by a fast proton or neutron in the case of an incident proton). Physically, the inelasticity is the fraction of the primary energy available for particle production. Higher inelasticity leads

to a greater particle number at shower maximum and a deeper penetration of the shower into the atmosphere. For KNP model, the inelasticity rises steadily with increasing energy. For the minijet and statistical models, the inelasticity holds nearly steady for the former, and drops rapidly for the latter. A more detailed general discussion of these three models can be found in the Fly's Eye literature [36].

Regardless of the model assumed, most of the energy goes into pions, dividing almost equally between charged and uncharged pions. This begins the electromagnetic shower cascade and muon production described in chapter 2.

The buildup of an EAS is reasonably well parameterized by the Gaisser-Hillas formula [34]:

$$N(X) = N_{\max} \left(\frac{X - X_0}{X_{\max} - X_0} \right)^{\frac{(X_{\max} - X_0)}{\lambda}} \exp\left[\frac{(X_{\max} - X)}{\lambda} \right] \tag{3.1}$$

Both X_0 and $X_{\max}$ are in units of g/cm^2. X_0 refers to the point of initial impact in the atmosphere. $X_{\max}$ refers to the location of shower maximum, where the number of charged particles reaches its maximum value before ionization losses dominate. $N_{\max}$ is a scaling factor which gives the number of particles at $X_{\max}$. Finally λ is a model dependent constant. Assuming scaling, $\lambda \approx 70$ g/cm^2.

The Gaisser-Hillas formula has its basis in calorimetry. Amaldi [1] for instance parameterizes the shower as:

$$\frac{dE}{dt} = E_0 \frac{b^{\alpha+1}}{\Gamma(\alpha+1)} t^{\alpha} e^{-bt} \tag{3.2}$$

where t is in radiation lengths, Γ is the gamma function, b is a somewhat energy dependent parameter ≈ 0.5 and $\alpha = t_{\max}/b$. If we reexpress the Gaisser-Hillas form, by arbitrarily setting $X_0 = 0$ for clarity, and work in terms of radiation lengths via, $x = X/\lambda$ and $x_{\max} = X_{\max}/\lambda$ then we get:

$$N(x) = N_{\max} \sqrt{\frac{2\pi}{x_{\max}}} \left(\frac{1}{x_{\max}!}\right) x^{x\max} e^{-x} \tag{3.3}$$

The first three factors are constants. The remaining functional form is essentially identical to the Amaldi form.

The average value of X_0 depends on the composition of the primary, with heavier elements interacting higher in the atmosphere, i.e. lower values of X_0 . A simple way to understand this is to consider a heavy atom as a bunch of independent nucleons traveling in the same direction. Once one interacts with the atmosphere, the nuclear mess begins. With more nucleons it is statistically more likely that one will interact earlier. This picture is called the superposition model.

Typical values of X_0 for proton primaries are 78 ± 80 g/cm^2 at 10^{14} eV and 71 ± 71 at 10^{15} eV. These values are taken from a study [46] of shower development by Karlsruhe group using their detailed CORSIKA simulation. Their errors are somewhat misleading because the distribution is exponential rather than gaussian. The hadronic model dependence is less than 5 g/cm^2. X_0 is less certain at 10^{17} eV, but should be around 50 g/cm^2.

Using the superposition model and an $A^{2/3}$ cross section dependence, iron primaries would be expected to interact almost immediately at around 5 g/cm^2 at 10^{17} eV. In practice, such early interaction should lead to much lower $X_{\max}$ fluctuations for iron primaries than were experimentally seen by the Fly's Eye. This discrepancy can not be written off as poor understanding of detector related $X_{\max}$ fluctuations, because the difference in reconstructed $X_{\max}$ between the two sites for events observed in stereo provides a direct measurement of detector related $X_{\max}$ fluctuations. A value of 20–40 g/cm^2 is consistent with the Fly's Eye data. CORSIKA results extrapolated to 10^{17} eV suggest a value of at least 10 g/cm^2.

Experimentally, X_0 is not directly observable because the shower does not build up to a detectable level until several radiation lengths. Although X_0 can be inferred directly after fitting the Gaisser-Hillas form, the resulting statistical error from the fit is very large. Being unable to measure X_0 directly is not a problem because better composition discrimination is

available from $X_{\max}$. Considering the above, the X_0 separation for proton and iron primaries is less than 40 g/cm^2. Fortunately, the separation grows to around 100 g/cm^2 for $X_{\max}$. Once again the superposition model provides a basic explanation. The relationship between X_0 and $X_{\max}$ is energy dependent, with $X_{\max}$ increasing about 55 g/cm^2 per decade in energy. This 55 g/cm^2 elongation rate, $(dX_{\max}/d(\log_{10} E))$, is also almost independent of the nuclear model used. Gaisser [36] gives 55±1, 52±2, and 60±2 g/cm^2 for the KNP, minijet, and statistical models respectively. These numbers are nearly independent of composition. Using the superposition model, an iron primary generates 56 independent showers with 1/56th the primary energy. An elongation rate of 55 g/cm^2 implies a change of the proton–iron $X_{\max}$ from the X_0 separation by $55 \times \log_{10} 56 = 96$ g/cm^2. More precise monte carlo simulations of the expected proton–iron separation for the three models by Gaisser [36], yields 97, 98, and 92 g/cm^2 for the KNP, minijet, and statistical models respectively.

Since the elongation rate and composition separation for $X_{\max}$ are almost independent of the model used, the only discrimination the fluorescence technique makes between the models is the mean value of $X_{\max}$ for showers of a fixed energy and composition. The biggest difference is 39 g/cm^2 between the KNP and statistical models. The Fly's Eye $X_{\max}$ distribution was extremely inconsistent with the statistical nuclear model. This can be stated with considerable confidence, because the Fly's Eye results spanned most of the proton–iron separation leading to data being far out of bounds of the model for the iron dominated energies. The KNP and minijet models only have a difference of 10 g/cm^2 which was too small for Fly's Eye to discriminate well, although the KNP model fits the data slightly better.

Finally, it has been noted above that X_0 varies considerably. The shower development also varies. Although one might expect a larger RMS for $X_{\max}$, than for X_0, there turns out to be little difference in monte carlo simulations.

3.2 Muon Component

3.2.1 Variation with Energy

Shower muon production depends on the primary composition and energy. One set of simulations [30] up to 10^{18} eV per nucleon suggests that the muon multiplicity for muons with $E > 1$ GeV and a primary fixed composition goes as the 0.86 power of energy. The AKENO group [40], gives $N_e \propto E^{1.11}$ and $N_\mu \propto N_e^{0.77\pm0.02}$ over the range $10^{16.5}$–$10^{19.5}$ eV, where N_e is the number of electrons at the ground. They combine these and obtain $N_\mu = 10^{-8.38\pm0.35}\ E^{0.84\pm0.02}$. The threshold for their muon detectors is 1 GeV. The large error in constant term is representative of various attempts to find this relationship solely with a ground array.

The range of exponents predicted by different hadronic models can be surmised from detailed simulations at lower energies. The Karlsruhe group studied five models using their thorough CORSIKA shower monte carlo. They present a study [46] of showers at 10^{14} eV and 10^{15} eV, with both proton and iron primaries. Each category has 500 showers. The exponents for muons with $E_\mu > 0.3$ GeV range range from 0.86–0.92.

A major goal of this work is to provide a good experimental determination of the N_μ – E power relationship.

3.2.2 Variation with Composition

Theoretical models predict that for the same energy, heavier primaries will produce more muons. The expected difference between iron and proton primaries is a factor of ~ 1.8. There are two major reasons for this. First, consider the implications of the superposition model. For heavier nuclei, the energy per nucleon is A^{-1} lower than for a proton primary. Because $N_\mu(E)$ goes like a power law with an exponent slightly less than one, this leads to higher muon production assuming the superposition model. Mathematically this gives an iron to proton ratio of $A(E/A)^{0.86}/E^{0.86} = A^{0.14} = 56^{0.14} = 1.76$. Second, the tendency for iron to interact higher in the atmosphere, increases the probability that the generated pions

and kaons will decay into muons rather than interact with the atmosphere. This follows from the decreased atmospheric density at high altitudes. Also the earlier pion production decreases the chance that the pion will reach the ground without decaying or interacting; however, this effect is rather small because the atmosphere is many times the attenuation length for decay or interaction.

The superposition model is known to be inexact. Unfortunately, the difficulty of simulating very large shower cascades together with the issue of model dependence limits improvements. Bozlev [18] has run simulations which show a departure from the superposition model in favor of additional muons for heavy elements. He compares primaries with atomic number A whose *nucleons* have the same energy. In this case if $\overline{n}_A$ is the average number of muons generated for A nucleons, the superposition model predicts that:

$$\frac{\overline{n}_A/A}{\overline{n}_1} = 1 \tag{3.4}$$

For iron, with $E_{\text{nucleon}} = 10^{16}$ eV, corresponding to a 5.6×10^{17} eV shower, he obtains 1.12 ± 0.31 for the above ratio. In addition to the large error bar, these simulations were conducted for very high energy muons ($E > 200$ GeV) which probably limits the usefulness of this result. The CORSIKA based results also shed some light on departures from the supposition model. After deriving the N_μ – E relationship for each model based on the 10^{14} and 10^{15} eV results, the actual N_μ iron result at 10^{15} eV can be compared with that predicted from the proton result at 10^{15} eV using the superposition model. Four of the hadronic models predict 5–10% fewer muons than the superposition model. The fifth, VENUS, predicts 6% more than the superposition model.

The fact that the muon multiplicity depends on composition suggests a correlation between X_{max} and N_μ , where N_μ is the muon multiplicity at a fixed energy. This work will explore this relationship.

3.2.3 Lateral Distribution

The muon lateral distribution has long been of interest to researchers. Greisen [38] gave the form:

$$\rho_\mu(R) = N_\mu \, (C_\mu/R_0^2) \, r^{-\alpha} \, (1+r)^{-\beta} \tag{3.5}$$

where $r = R/R_0$, where R_0 is a characteristic distance, and C_μ normalizes the probability and is given by $C_\mu = \Gamma(\beta)/2\pi\Gamma(2-\alpha)\Gamma(\alpha+\beta-2)$. Greisen gave $R_0 = 320$ meters, $\alpha = 0.75$, and $\beta = 2.5$, and $C_\mu = 0.262$. Plugging these in, the lateral distribution becomes:

$$\rho_\mu(R) = N_\mu \, (R/320)^{-0.75} \, (1+R/320)^{-2.5} \cdot 0.262 \tag{3.6}$$

The AKENO/AGASA group has checked [40, 39] this form and found good agreement within 800 meters of the shower core over the range $10^{16.5}$–$10^{19.0}$ eV. They found the optimal parameters to be $\alpha = 0.75$, $\beta = 2.52 \pm 2.02$ and $\log(R_0) = (2.39 \pm 0.05) + (0.58 \pm 0.04)(\sec\theta - 1)$. The latter term in the R_0 expression is a minor adjustment for nonvertical showers. For vertical showers this formula gives $R_0 = 245$ meters.

Beyond 800 meters from the shower core, they reported a faster falloff than the Greisen form. They proposed modifying the Greisen form by adding a rolloff factor. Their form became:

$$\rho_\mu(R) = N_\mu \, (C'_\mu/R_0^2) \, r^{-0.75} \, (1+r)^{-\beta} \, \{1 + (R/800\text{ m})^3\}^{-\delta} \tag{3.7}$$

where $\delta \sim 0.6$ and the normalization C'_μ is numerically computed to be 0.325 for $\alpha = 0.75, \beta = 2.52$. This form shall hereafter be called the AKENO lateral distribution.

Other experiments have also examined the muon lateral distribution but their results seldom extend reliably past 1000 meters. For example, the Haverah Park array data [10] is largely within 1000 meters, although one plot shows three points with low statistics in the

1000–2000 meter range. Although their evidence is less compelling than that of AKENO, they also see a lower density than the Greisen formula prediction beyond $\sim$ 1000 meters.

A comparison of HIRES–MIA data and the AKENO and Greisen lateral form will be made in chapter 9.

There is also considerable interest in the long range lateral distribution, beyond 1000 meters. A strong practical motivation is the proposed construction of the giant AUGER ground array. Obtaining the long range distribution has been difficult because stand alone ground arrays require the event to fall within or very near to the array in order for the core to be accurately determined. The HIRES–MIA combination allows a more precise reconstruction of the core for events falling far outside the MIA array. However, it is unfortunate that the thickness of the shower arrival front becomes large enough and the density low enough that it becomes difficult to distinguish true intime muon from out of time accidentals. The best compensation for this problem requires more work. No results will be presented here.

3.2.4 Fluctuations at the ground

The expected fluctuation in the number of muons arriving at the ground for showers initiated at fixed energy and composition primary is not well known because it requires having a detailed and accurate shower monte carlo at $\sim 10^{17}$ eV. Otherwise it becomes difficult to be sure one is actually examining fluctuations. In addition, time saving mechanisms such as thinning the shower by tracking only some particles may not work well. Thinning is much more reliable for studying average quantities rather than fluctuations.

More work needs to be done to get a good answer for the expected muon fluctuations for the HIRES–MIA dataset. The lower energy Karlsruhe CORSIKA simulations at least allow an upper limit to be set, since larger showers will have lesser fluctuations. The N_μ distributions are reasonably gaussion in $\log(N_\mu)$. For iron primaries the σ_{N_μ} is $\sim$ 33% and $\sim$ 26% for 10^{14} eV and 10^{15} eV showers respectively. The corresponding results for iron primaries are 11% and 10%. The hadronic model dependence of σ_{N_μ} is slight, $\delta\sigma_{N_\mu}/\sigma_{N_\mu}$

less than 20%, where $\delta\sigma_{N_\mu}$ is the difference between the models. Also some probably minor adjustment is needed to account for the difference in the MIA array altitude and the 110 meters above sea level assumed in the simulations.

3.2.5 Energy Distribution

The energy distribution of the muons at ground level is important in order to compare observations between ground arrays with different thresholds. 1 GeV is a realistic minimal detector threshold to insure sufficient shielding from electrons and other shower particles.

Figure 3.1 shows the Karlsruhe muon energy spectrum for proton primaries. Their simulations only track muons down to 0.3 GeV. It is clear that very few muons are neglected from this cutoff. Table 3.1 reexpresses Karlsruhe data in terms of the fraction of muons falling in the range 0.3–1.0 GeV. This will come in handy later for estimating the systematic uncertainty in N_μ arising from the uncertainty in detector threshold energies.

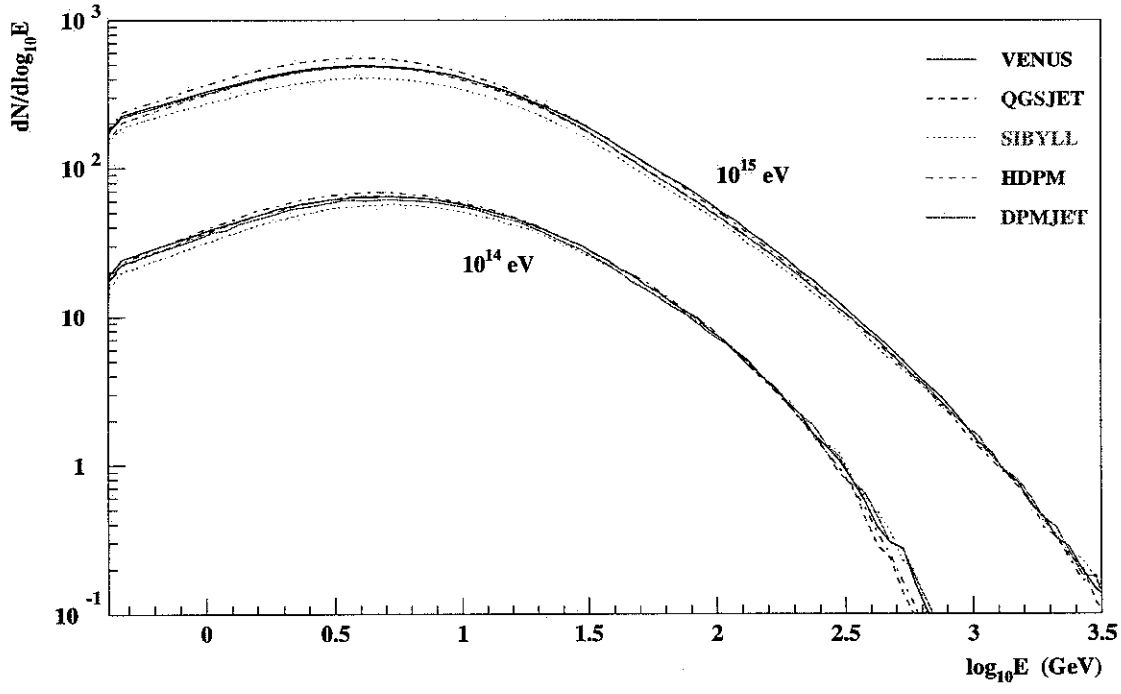

Figure 3.1: Energy spectrum of muons arriving at the ground (110 m a.s.l.) for 10^{14} eV and 10^{15} eV iron generated showers. The different lines show CORSIKA simulation results for different hadronic models.

Table 3.1:

Percent of Total Muons with energy 0.3–1.0 GeV				
	10^{14} proton	10^{15} proton	10^{14} Fe	10^{15} Fe
VENUS	15.3	17.7	11.4	13.5
QGSJET	15.1	17.2	10.9	13.0
SIBYLL	15.9	18.1	10.8	13.6
HDPM	15.9	18.2	11.0	13.3
DPMJET	15.6	17.2	11.1	13.5

Chapter 4

Detectors

The HIRES prototype is not adequately described in any of the literature. The Fly's Eye NIM paper [4] describes many of the issues important in designing a fluorescence detector. The original 1990 HIRES construction proposal [67] laid out general plan for a three site HIRES but lacks many details specific to the eventual evolution of the HIRES prototype. The 1991 operations proposal [68] gave an update, but at a time when only two of the 14 mirrors had been installed. The 1993 Staged Construction Proposal [69] discussed sky noise, early data processing, plane fitting, and laser shot studies, following operations with the full 14 mirror prototype. It did not however describe the Prototype setup. The discussion below will describe specifically the 14 mirror HIRES Prototype. MIA and CASA are well documented elsewhere and therefore will only be described briefly.

4.1 HIRES Prototype

4.1.1 Overview

The Prototype detector began full 14 mirror data collection in March 1993 and collected data until November 1996, after which it was reconfigured and incorporated into the full HIRES detector with only minor changes. The detector was situated upon a hill in the Dugway Proving Ground Army base amidst the western Utah desert. Its GPS determined location was $40^\circ\,11'\,43''$ latitude, $112^\circ\,50'\,9''$ longitude, 1597 meters above sea level. This is equivalent to an atmospheric depth of 860 g/cm^2. Figure 4.1 shows an overview of the

physical site. Seven buildings held two mirrors and two phototube clusters each. Five buildings were sheds with electronically controlled doors. The other two were corncrib silos used for mirrors which were oriented towards high elevations. The electronics was divided between the mirror buildings and the central trailer.

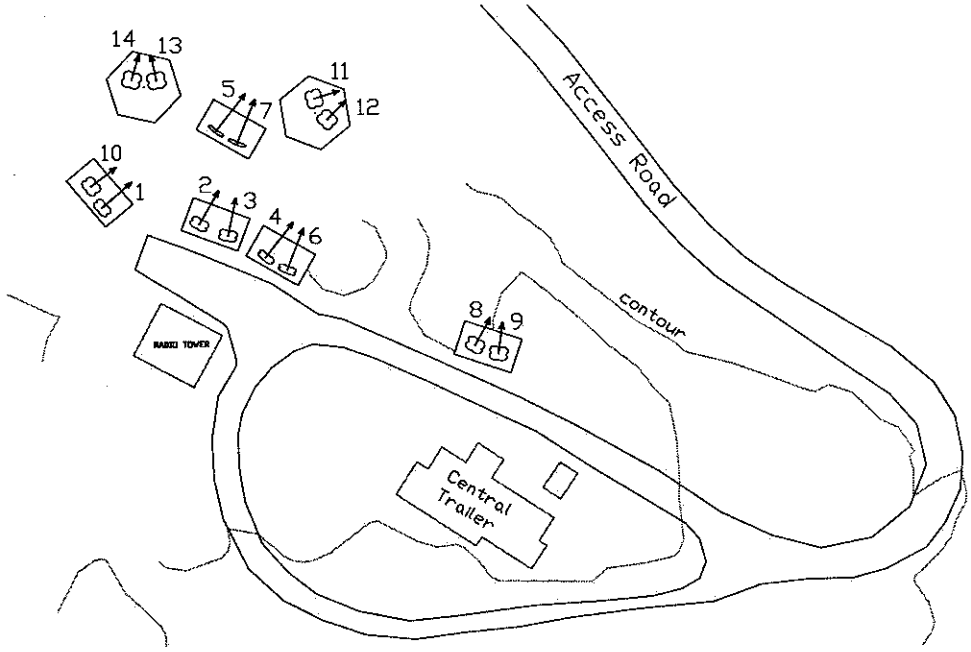

Figure 4.1: HIRES1 Prototype physical layout

Figure 4.2 show a rough outline of the HIRES system. Fluorescence light from the shower is collected by each mirror and focused onto a cluster of photomultiplier tubes. The PMT signals are processed by a mirror electronics crate. The central timing crate records the absolute trigger time. Tube data is collected from each mirror crate by the central computer and stored to disk.

Figure 4.3 shows a much more detailed block diagram of the data acquisition system components and communication. The data acquisition subsystems, grouped according to function, are:

- Photomultiplier Tubes and Cluster
- High Voltage Distribution

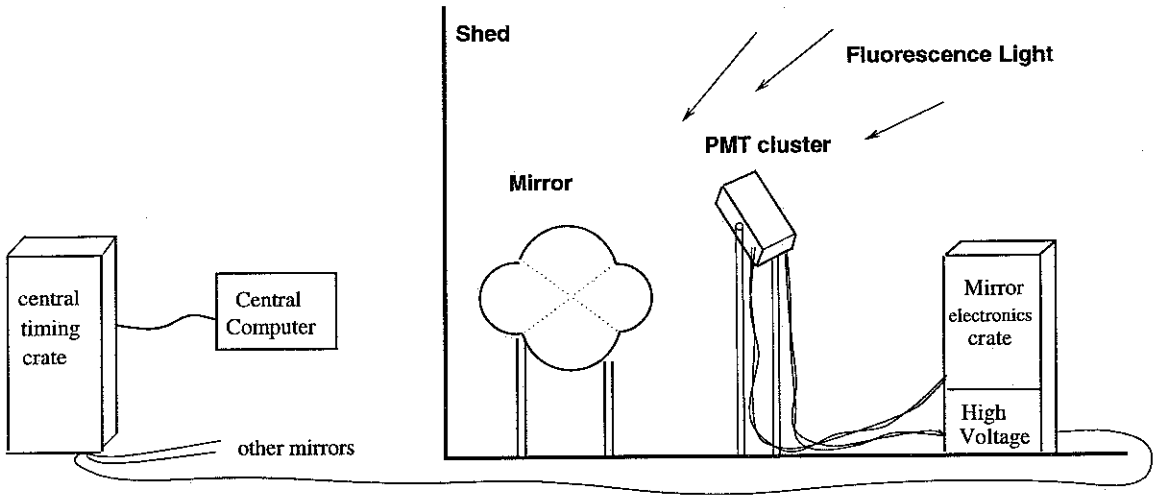

Figure 4.2: Basic HIRES operations diagram

- Mirror Electronics Crates
- Central Timing Crate
- Data Storage
- Intersite Flasher

Each of these subsystems is discussed in turn below.

The basic system unit is the mirror data acquisition system. Mirror systems are located remotely two per shed to minimize data cable length to less than 10 meters/channel. Each mirror system consists of a mirror, a cluster of photomultiplier (PMT) tubes in the focal plane of the mirror, the cluster related electronics, and the mirror electronics. The PMT cluster consists of 256 hexagonally packed PMTs which observe a $16° \times 13°$ night sky patch for photons generated by extensive air shower nitrogen fluorescence. The PMTs convert the light into electrical signals and pass these waveforms into the pulse measurement system located in the VME crate. The cluster related electronics include the power supplies for phototube preamp power and phototube high voltage, and the high voltage distribution system.

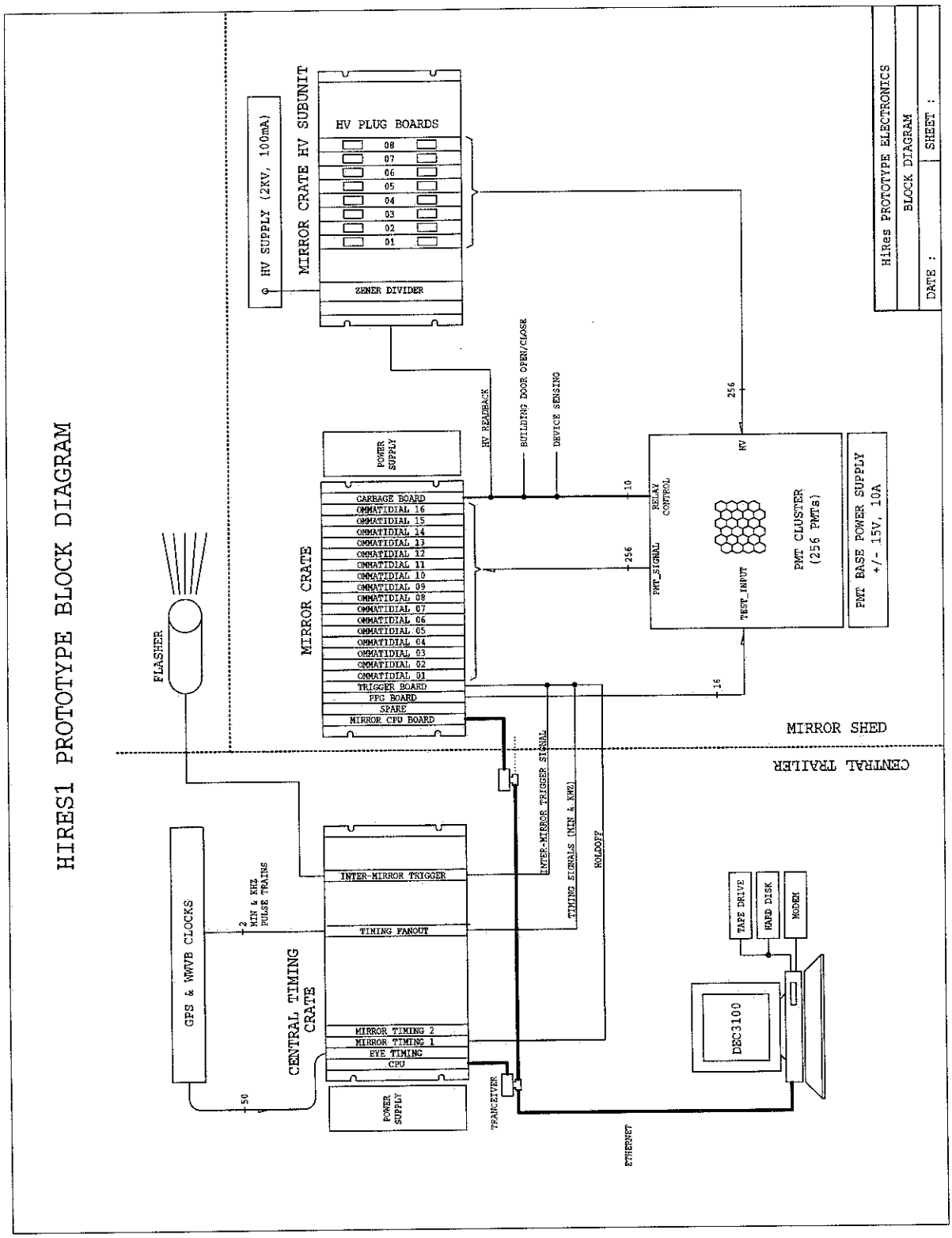

Figure 4.3: HIRES1 Prototype detailed block diagram

The mirror electronics are located in a single VME crate associated with each mirror/-cluster. The VME crate contains all the electronics necessary for measuring phototube waveform characteristics. The crate contains 68030-based VxWorks Force controller, 16 data acquisition boards (named 'ommatidial' boards), a Trigger board, a programmable pulser board (PPG) and a sensor/relay board (referred to as the 'Garbage' board). Each ommatidial board (OMB) processes one *subcluster* of 16 PMTs. All communication with the VME crates, except the direct trigger timing line and a timing pulse train, is carried over an Ethernet line attached to the central data acquisition computer.

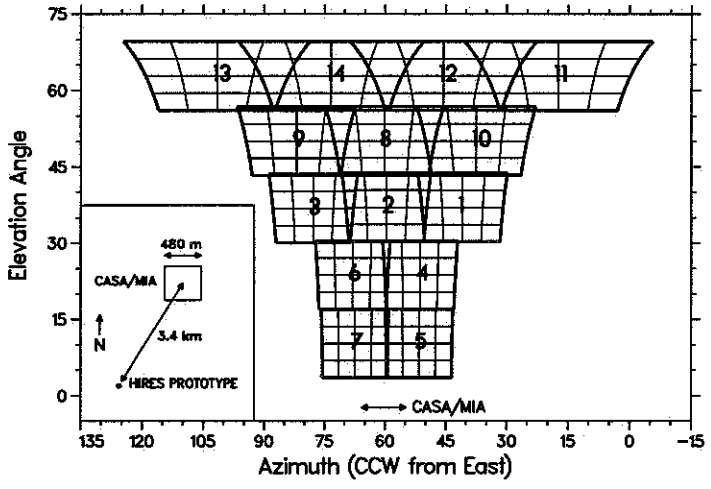

Figure 4.4: HIRES Prototype Field of View. CASA–MIA appears in the center of the FOV. The inset shows the spatial relationship between the HIRES prototype and CASA–MIA

The HIRES prototype consists of 14 of these basic mirror DAQs. Figure 4.4 shows the field of view of the 14 mirrors as well as the division of each mirror into subclusters. The projection of rectangular clusters onto a spherical field of view results in increasing overlap between mirrors at high elevations. All together the 3584 phototubes view 0.81 steradian. The figure inset shows the relation of the HIRES detector to CASA–MIA. CASA–MIA is centered in the HIRES field of view and appears 8 degrees wide.

The operations trailer contains a single central timing (CT) VME crate and the central data acquisition computer. The CT crate allows time synchronization between all the mirror crates. It contains the master clock and records times from each mirror's direct trigger line. It also handles the neighboring mirror trigger. The central data acquisition computer is a UNIX based Decstation 3100. This machine stores the data to disk and controls the VME crates.

When the detector is in operation, the central data acquisition computer continually pulls in data and status information from each mirror crate and timing information from the CT crate. These are referred to as HIRES packets, which are implemented at the network Transport layer via UDP. This data is stored to disk. No effort is made in real time to match up the data and timing packets. This is done offline as discussed in chapter 5.

4.1.2 Photomultiplier Tubes and Cluster

The HIRES Prototype uses hexagonal phototubes to provide full close packing coverage of the cluster face without the use of Winston cones. Seven of the prototype mirror clusters (2,4,5,6,7,8,13) use EMI 9974KAFL photomultiplier tubes. The remaining seven use Phillips XP3062/FL photomultiplier tubes. All phototubes are 40 mm in diameter and are situated to subtend a 1° aperture. Individual phototubes are soldered directly to a high voltage bleeder chain/preamp printed circuit board. The preamp adds a gain of 100 onto the phototube pulse and then generates a differential signal. This means that the DC sky noise contribution has no impact on the signal, although sky noise fluctuations obviously do. Each preamp circuit board has an external test input which allows electronic calibration of the full data acquisition system with no high voltage applied to the phototubes. Each phototube is wrapped in magnetic shielding metal.

The entire phototube/circuit board assembly mounts into a cluster frame with a 256 socket backplane which distributes power and test signals to the circuit boards and transmits phototube pulses from the circuit boards to the ommatidial boards. High voltage is

distributed to each tube through 256 20 gauge high voltage wires divided among 16 connector blocks. This is done to avoid signal contamination.

A single custom made ultraviolet filter mounts directly on the cluster face. The filter is mounted on a hinge to allow easy access for replacing tubes. Heat buildup is removed by a cooling fan on top of the cluster. To aid heat removal, the sides of the cluster are bonded with a heat conducting paste and an aluminum sheet runs vertically through the center of the cluster. A temperature sensor is set at the center of the cluster.

4.1.3 High Voltage Distribution

For each mirror, a positive high voltage distribution system provides the power necessary to drive the cluster's 256 PMTs. The system is a simple zener voltage divider chain, powered by a single 2 kV 100 mA supply, allowing 900–1500 V selectable in 25 volt steps. The zener taps are fed into a matrix plug board which allows each tube to tap into the desired voltage for that tube. Each tube is therefore hardware programmable to within 12.5 volts of its optimal gain balanced voltage as determined by calibration. This scheme is inconvenient but very cheap. In practice the phototube gains are very stable, requiring adjustments less frequently than once a year. A VME crate controlled high voltage readback system is incorporated for each channel of every cluster, allowing set voltage verification.

During voltage calibration it is very handy to have a programmable power supply. In addition to the HV plug boards, the HV connectors are designed to fit into a 256 channel programmable LeCroy 1440 unit which can be moved from mirror to mirror. This allows quick calibration.

4.1.4 Mirror Electronics Crate

A VME crate provides the platform for the mirror electronics. This crate contains 16 ommatidial boards, a Trigger board, a 68030-based VxWorks Force controller (the Mirror CPU board), a programmable pulser (PPG), and a sensor/relay board ('Garbage' board). The

first three boards are discussed below. The PPG is a simple pulse injector used for diagnostic and calibration purposes as discussed in chapter 6. The 'garbage' board handles the high voltage readout system, controls preamp power to individual PMT subclusters through the cluster relay board, opens and shuts shed doors, and monitors crate temperature.

PMT Charge and Timing

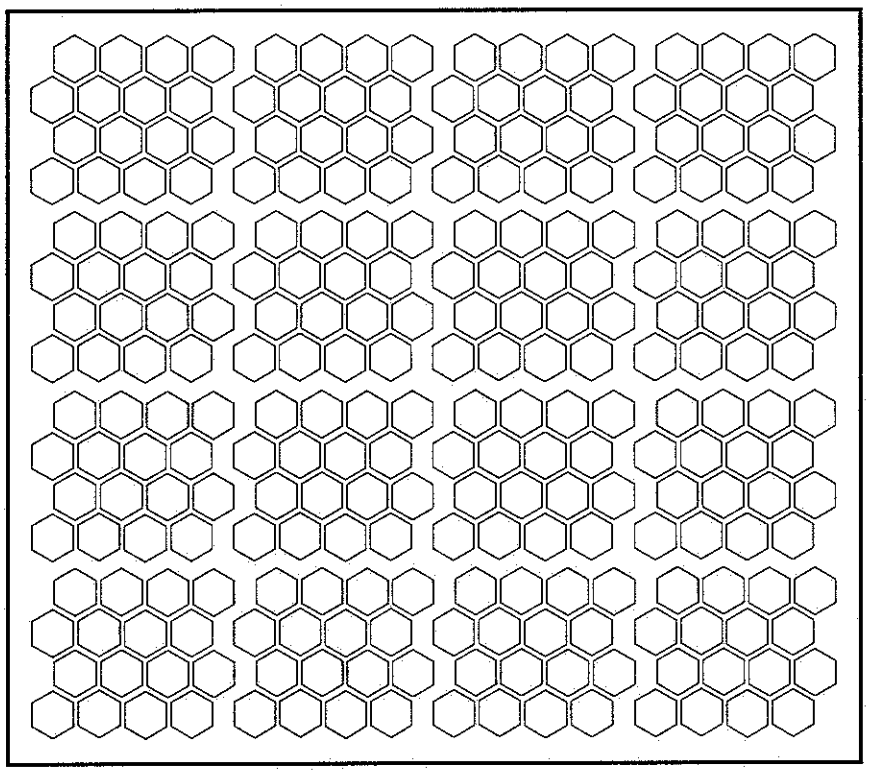

Figure 4.5: Division of a mirror cluster into 16 subclusters of 16 phototubes each. Each ommatidial board is responsible for processing signals from one subcluster. N.B. In the actual cluster there is no physical separation between subclusters.

Each ommatidial board stores the integrated waveform charges and waveform leading edge arrival times above threshold for a 4×4 subcluster of phototubes (see Figure 4.5). Figure 4.6 shows a block diagram of the ommatidial board operation. The input signal of each tube is split into a trigger/timing component and a charge integral component. The trigger component is shaped by either a 100 nS 1-pole RC filter or a 375 nS 3-pole LC bessel filter in order to suppress background noise. This is software selectable. Threshold triggers,

Hires1 Ommatidial Board Electronics

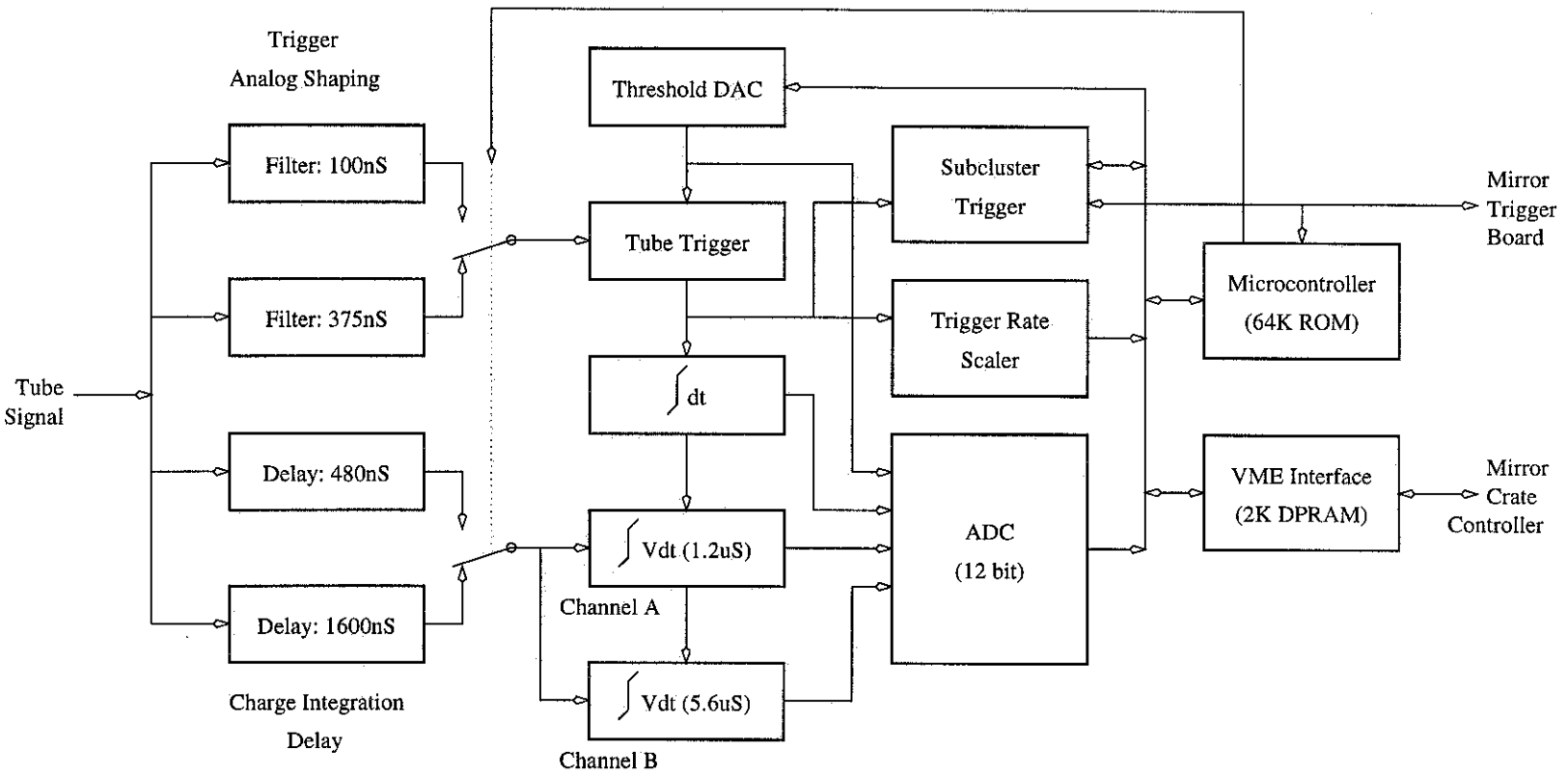

Figure 4.6: Ommatidial board block diagram

located after the filters, initiate phototube timing and pulse height integration. A choice of delays lines, 480 nS or 1600 nS, corresponding to the choice of shaping filter, insure that none of the charge integral component is missed. Phototube timing is measured by charging a capacitor with a constant current source from the time of the threshold crossing to the mirror level trigger time, and then measuring the charge in the capacitor. A larger charge indicates an earlier trigger.

Following the delay line, the charge integral component is split into two channels, designated **A** and **B**. The two channels have different integration time periods. This is desirable because HIRES event signals have the unusual property that their time width is roughly proportional to the distance of the shower from the detector because each tube subtends a fixed angular range in the sky. A large gate width is not desirable for nearby showers because only an integrated signal is recorded; therefore, a larger gate width means the cumulative effect of the night sky background fluctuations will be unnecessarily large. For a point source shower detected with perfect optics, the time required to cross a tube from one corner to the opposite corner is ≈ 60 nS/km. However, optical effects (see section 6.3.2) add an additional 70–200 nS/km depending on how far the tube is from the center of the cluster. The ~ 100 meters finite vertical extent of the shower also increases the crossing time, but this effect is small compared to the optical effect and actually decreases with shower distance. The chosen gate widths of 1.2 μS and 5.6 μS provide an adequate compromise between not clipping any of the waveform while keeping the sky noise contamination low when possible.

The charge integrals are stored capacitively identical to the timing component. An analog multiplexer fans the 48 storage capacitors (2 charge and 1 timing per tube) into a 12-bit ADC for readout by the 80188 microcontroller chip. A 16-bit scaler monitors the trigger rate for each PMT. Individual phototube thresholds are dynamically adjusted through a DAC by the microcontroller to maintain a constant singles rate.

Trigger

Each ommatidial board stores the time and charge integral information for each of the 16 subcluster PMTs. Whenever a subcluster PMT crosses threshold, constant current time charging begins for that PMT and the PMT's individual trigger flag is set for at least 25 μS. During this 'holdoff time', the PMT's integrated charge is saved and the tube is not permitted to retrigger. If a mirror level trigger is not formed within 25 μS of the tube trigger time, the tube trigger flag is cleared along with the tube timing and integrated charge information.

Both the subcluster and mirror level triggers are asynchronous. For each subcluster the 16 PMT trigger flags form the input address for a 64K $\times$ 8-bit EPROM, which serves as a lookup table. Each bit at the address corresponding to a given trigger flag pattern, indicates whether the subcluster has triggered according to one of the preprogrammed patterns. The specific bit used for the trigger is software settable. The possible subcluster minimal trigger patterns are:

- any tube
- any two tubes
- any three tubes
- any two hexagonally adjacent tubes
- three tubes with at least two hexagonally adjacent
- all tubes

A subcluster remains triggered only as long as there is a pattern of PMT trigger flags meeting the trigger condition.

During normal data collection, all subclusters are set to 'three tubes with two adjacent' and a phototube singles rate of 200 Hz. Calibration processes use some of the other subcluster trigger requirements.

The subcluster triggers in turn form the input address for another 64K $\times$ 8-bit EPROM on the crate Trigger board. This also acts as a lookup table. The possible minimal cluster

patterns are the same as the subcluster patterns given above, except that adjacent means orthogonally plus diagonally, rather than hexagonally. When a mirror trigger is formed, the 'holdoff' time for all triggered tubes is extended an additional 10 μS, i.e. charge integral and time information is retained 10 μS for all triggered tubes. Additional triggers are permitted for tubes which have not triggered already. This allows the track to finish crossing the mirror. At the end of this period, a mirror trigger signal is sent to central timing crate so that the absolute mirror time is recorded to within 25 nsec. Immediately afterwards, the mirror crate experiences a dead time $\sim$ 8 mS, while the time and charge information is read by the Mirror CPU board for *any* PMT whose trigger flag is set, i.e. any PMT which has received a hit in the past 35 μS. This includes triggered PMTs belonging to subclusters which did not generate subcluster triggers.

Typical run conditions result in 30–120 mirror level triggers/minute-mirror.

Each mirror also receives subcluster trigger information from adjacent mirrors to trigger on a track which is fully detected in one mirror, but only clips a single subcluster edge in an adjacent mirror. This 'neighbor' trigger was not added until October 1993.

Mirror CPU

The Mirror CPU board is the primary interface between the central computer and the crate's ommatidial boards, Trigger board, PPG board, and Garbage board. It sends event and status data back to the central data acquisition computer, and receives commands to set modes and such on the other boards. The most important job is to return event data to the central computer. After reading out the time and charge information from the ommatidial boards, it attaches an event scaler, and minute/msec scalers, driven from the master clock pulse trains. This ensemble is returned as a HIRES event packet over the ethernet using UDP protocol. The scaler values aid in sorting and matching the data offline. Status information includes the tube triggers, the tube thresholds, deadtime, network performance, and the answer to operator queries such as the current trigger requirements, PPG pulse parameters, and so on. HIRES Control packets directed at the OMBs, set thresholds, require

thresholds to vary to maintain a constant tube singles rates, set optimal tube singles rates, or enable/disable tube triggering. HIRES Control packets directed at the PPG, change the pulse shape, trigger rate, and fire the pulser. Those directed at the Trigger board set the cluster trigger requirement. A few Control packets cause sophisticated processes to occur. For example, during calibration the Mirror CPU sets the OMB's trigger requirement, directs the PPG to fire multiple pulses of varying width and height, interprets the triggered signals, and returns a summary of the results to the central computer.

At the hardware level, the Mirror CPU board is a VxWorks FORCE30 based on 68030 processor. VxWorks is a sophisticated real time operating system with UNIX like features. Software specific to HIRES is downloaded from the central computer whenever a Mirror CPU board is rebooted. This give the data acquisition system considerable flexibility. It is also possible to login to a Mirror CPU board and examine the status of processes for diagnostic purposes.

4.1.5 Central Timing Crate

The central timing crate (CT) establishes the absolute time and synchronizes event mirror–to–mirror timing to within 25 nS. It also generates the intermirror trigger and triggers the intersite flasher.

The absolute time is determined from either a GPS or WWVB clock. The former is absolutely accurate to $\sim$ 340 nS, a limitation imposed by the U.S. Army. However, when two sites lock onto the same satellites the relative accuracy is reduced to $\sim$ 10 nS. The WWVB clock is only good to 1 msec and separated sites can drift by as much as 2 msec. Unfortunately, the HIRES prototype did not have a working GPS clock until Jan 1995, which means 40% of the MIA–HIRES data was collected with a WWVB clock.

Both the GPS and WWVB clocks receive a pulse every second. Between pulses time is maintained by a 40 Mhz scaler. Under the GPS system, the scaler drift, typically 1 part in 10^6, is recorded so that additional timing corrections can be made. A Timing Fanout

board generates pulse at the start of each minute and every msec. These are tracked by the individual Mirror CPU boards and packed in the event data as described above. This only establishes crude timing to aid in the sorting and matching. Mirror triggers bypass the ethernet (which is far too slow) arriving directly at CT. Each mirror latches the 40 Mhz scaler value. Additional mirror triggers arriving within 50 mS of the previous mirror, up to 128 latches, are stored as part of the same HIRES Timing packet. Each mirror trigger also latches the *ones* and *tens* values of msec value of the absolute time. This aids in sorting and matching the HIRES Event and Timing packets offline. When the Timing packet is complete it is transferred over the ethernet to the central computer. The central timing crate also generates a pulse for a Xenon flasher which lies in the line of site between HIRES and MIA–CASA, allowing an intersite trigger or confirmation. See chapter 5 for details.

4.1.6 Data Storage

The individual mirror trigger rate is about 30–120 triggers/minute. The rate increases for mirrors viewing larger elevations because the number of Cherenkov 'blast' events seen increases. Atmospheric clarity and the presence of clouds also affect the event rate. Heat lightening, often seen in the summer, can increase the rate by tenfold, which makes data taking impractical. Under normal conditions the detector rate is 8 Mb/hr, with the bulk of this being event data. The data is stored on a 2 Gb disk and removed to 8mm tape at the end of each run month.

4.1.7 Intersite Flasher

The intersite flasher provides a unidirectional way for HIRES to communicate with MIA-CASA. This is very important for two reasons. In the WWVB clock epoch site-to-site timing could be off by as much as 2 mS. The record of the flasher ('trkbit') in the MIA–CASA datastream could be used to distinguish real coincident events from accidentals. Even more importantly, MIA requires an external signal before the muon information is read out.

Usually this is a CASA trigger. But it can also be a HIRES driven trigger. This is essential because many HIRES–MIA events are too far away from CASA to trigger CASA, a result of a steeper lateral distribution rolloff for electrons than for muons.

Communication proceeds via a flasher and a receiving unit. The flasher is a Xenon flashbulb covered with a red filter to prevent backscattered flasher light from triggering the HIRES detector. It has a heating element to remove frost. The receiving unit is a converted portable Army medical unit which contains a mirror, which focuses the flasher light onto a photodiode. This signal is then amplified and directed to the MIA crate. It was also used to trigger Fly's Eye II for a period of time. The receiving unit is protected during the day by a light activated door which blocks the plastic window during the day.

4.2 MIA and CASA

The MIA detector is well described in existing literature [62, 47, 23]. Therefore, only a brief review, with emphasis on points particularly relevant to the HIRES–MIA dataset, will be presented here. CASA is also well described in two theses [49, 23].

MIA consists of 16 widely spread patches distributed within the CASA array as shown in Figure 4.7. Each patch contains 64 adjacent counters. The counters are buried three meters under ground to eliminate the electromagnetic component of the shower. Each counter is a 1.9×1.3 meter piece of scintillator in contact with a hemispherical EMI–Gencom type 9870B PMT.

The PMT signals travel back along the PMT HV lines towards the CASA–MIA central trailer. There they are decoupled by a capacitor and sent on to a discriminator. The discriminator thresholds are not varied, unlike the HIRES PMTs which must compensate for the changing night sky background. The discriminator output pulse starts a TDC. To save money, MIA was designed to record only the time each muon hit, not its pulse height. Over the time scale of one event, each counter yields a binary value. The TDC system consists of 32 LeCroy model 4291 TDCs, which have 4 nS resolution.

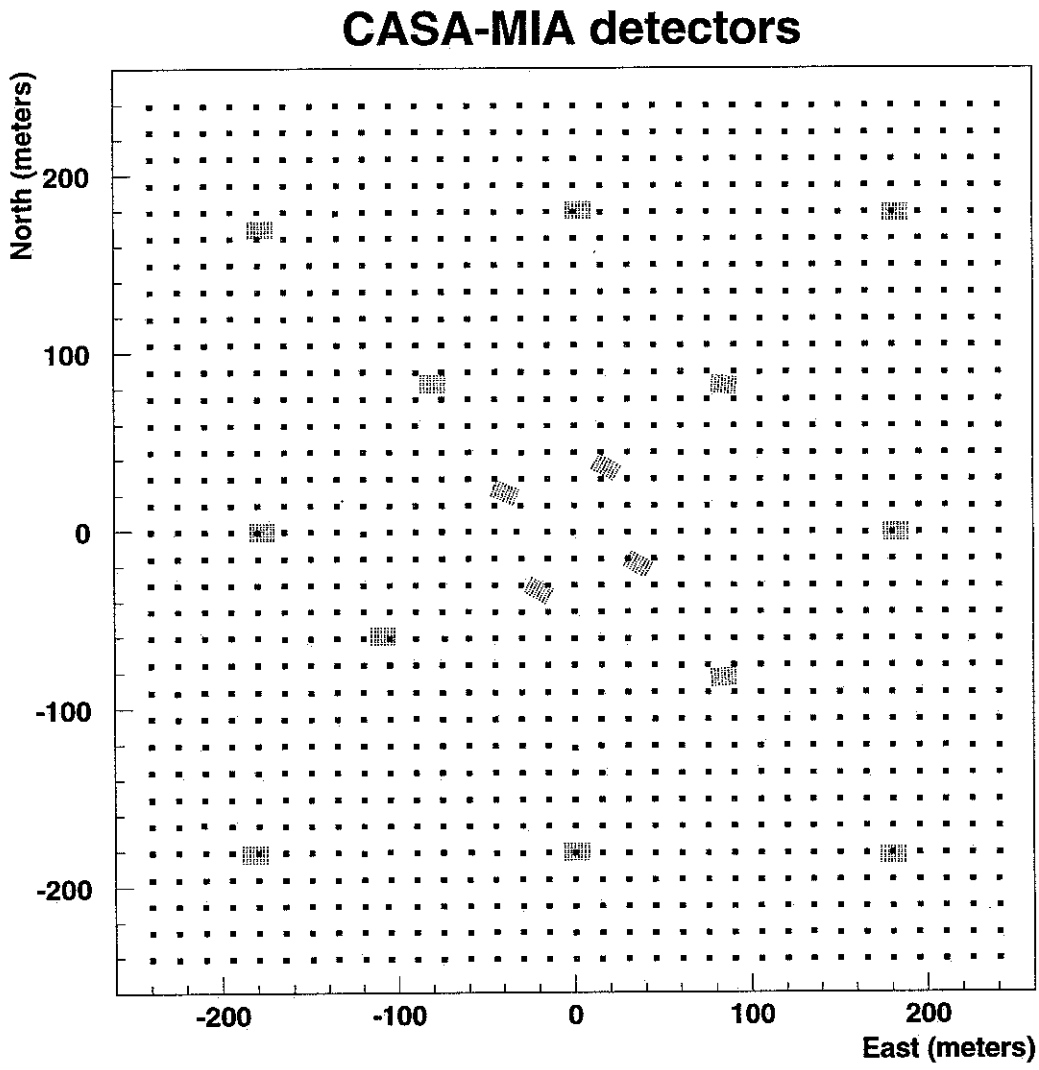

Figure 4.7: The 1089 CASA stations are spaced 15 meters apart. Each of the 16 buried MIA patches cover 158 m^2 with 64 counters. There are 1024 total MIA counters.

The TDCs are stopped by an event trigger. Therefore earlier muons have larger TDCs counts. If a counter is not stopped within 5.2 μS, it resets and awaits the next signal.

There are several situations which can cause an event trigger. The two of interest are CASA driven and HIRES driven. Any CASA trigger is automatically an event trigger and causes a readout of all MIA TDC values regardless of how many MIA counters have triggered. HIRES driven triggers are pick up by the flasher receiving unit and sent into the CASA–MIA trigger system. In order for a HIRES driven trigger to cause a MIA readout, a minimum MIA requirement must be met. This condition is that at least six patches have at least three counters hit. This ensures that the operation of HIRES does not add substantially to the MIA deadtime via accidental coincidences. It also prevents high trigger rate HIRES calibrations from completely dead timing out MIA.

The minimal MIA requirement is implemented via current sums. Each triggered counter generates a 5.2 μS pulse. A patch level discriminator triggers after three counters in the same patch trigger. This generates a 2.5 μS patch level current pulse. These in turn are summed. A final discriminator set for 6 counters triggers when the minimal conditions are met.

All HIRES–MIA–CASA triple coincidence are CASA driven because the CASA trigger will arrive before the HIRES trigger has time to arrive. Clearly, HIRES–MIA coincidences are driven by HIRES. Sometimes there are problems with the flasher or the flasher receiving unit. During the winter, ground haze or frosting of the plastic window on the receiving unit can block flasher reception. Unfortunately, one or more of these things happened fairly frequently.

The MIA turn on threshold is 1 GeV. Figure 4.8 is a GEANT simulation of a MIA detector for muons vertically incident on the center of a counter. The turn on is quite sharp. For overall counter efficiency, the MIA group quotes 93%. They made their measurement in situ shortly after installing the counters by using scintillation paddles and lead shielding above ground to detect muons which should be seen by the counters below ground. A later

1995 study[59], which attempted to measure efficiency as a function of time, indicated patch dependent counter efficiencies in the range 71% – 87%, averaging to 80% over the whole array. However, the technique used leaves considerable doubt about absolute efficiency. If the relative efficiencies in that study are to be believed, the array lost 13% efficiency over a four year period. For the analysis we use the 93% number.

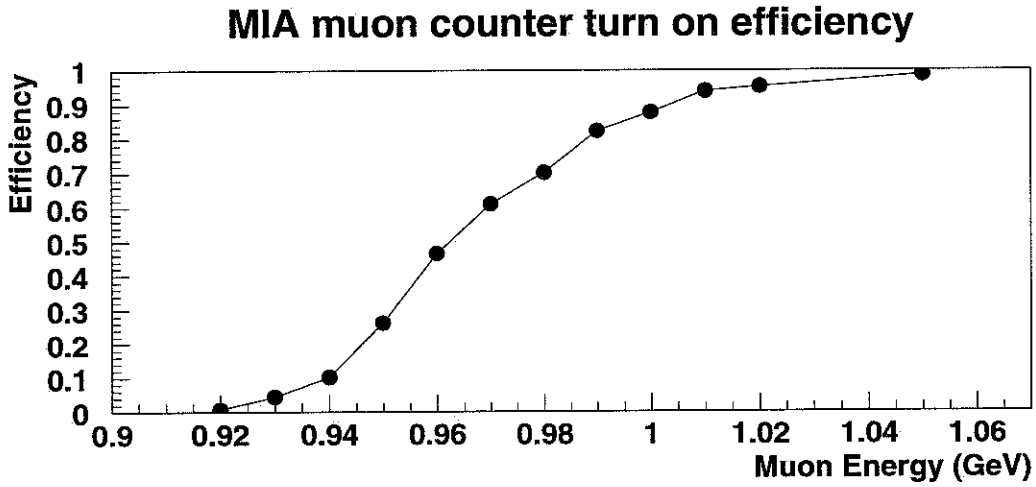

Figure 4.8: MIA counter turn on efficiency for muons vertically incident on the center of the counter modeled by a GEANT simulation.

CASA consists of 1089 (33 × 33) detector stations arranged on the surface in a rectangular grid with 15 meter spacing, as shown in Figure 4.7. The array is centered on the old University of Utah, Fly's Eye II detector. Each station consists of four counters. The total scintillator area for each station is 1.49 m^2. During the HIRES–MIA data collection period, a sheet of lead atop each station increased the detector sensitivity about 50% via $\gamma \rightarrow e^+e^-$ conversion. The counters record both timing and pulse height information.

Data from the counters is stored in a sample and hold circuit if two or more counters are hit within 30 nS of each other. A station with two hit counters is said to be *alerted.* A station with three or four hit counters is said to be *triggered.* The array is triggered if three or more stations trigger within 10 μS. When an array trigger occurs data is read out from

alerted and triggered stations. The average trigger rate is 22 Hz which results in a 1.2% deadtime.

CASA is sensitive from just above 10^{12} eV to just over 10^{17} eV, where many stations will saturate completely for an event falling directly in the array. CASA is not significant in this work for several reasons. Two thirds of the HIRES–MIA coincident events do not involve a CASA trigger. Most of the events which trigger CASA have cores outside the array and are therefore not treated by the standard CASA analysis. Events which fall in or near the edge of the array often saturate many of the counters.

Chapter 5

Dataflow

Dataflow for the HIRES–MIA dataset can be broken into three broad steps. The first includes processing which occurs whether or not the data from the two detectors is to be merged. The second involves the merging of the data to form HIRES–MIA–(CASA) coincident events. The final step consist of a series of analysis programs to determine the shower parameters discussed in chapter 3.

5.1 Basic Event Processing

On the HIRES side the basic event processing involves building events, calibrating the events, and filtering the result of the first two steps in order to pick out track like events. These procedures are detailed below.

On the CASA–MIA side the basic event processing is called PASS0. It is not necessary to "build" events for CASA–MIA because each event is read out as an entire unit after each trigger. PASS0 handles CASA channel calibration after determining channel pedestal levels, gains, and timing correction. For MIA only a timing correction is necessary since counter hits are binary in nature. Because CASA–MIA collects so much data in every 6 hour run, the data itself can be used to determine channel pedestals, gains, and timing corrections. This is well described in chapter 3 of Hans Krimm's thesis [49]. PASS0 also makes a first determination of core location, shower direction, and number of detected particles, but the HIRES–MIA

analysis does not use this information. There is a second CASA–MIA data process called PASS1 which will be ignored because the HIRES–MIA analysis does not make use of it.

5.1.1 HIRES Event Building

HIRES "events" are not built in hardware. As described in chapter 4, raw datafiles consist of HIRES data packets. The most important packets are Event and Timing packets, generated by individual mirror triggers and Central Timing (CT) respectively. Since these packets are transferred from the central computer over an ethernet they are only approximately time ordered in the resulting datafile. To build events it is first necessary to match the Event packets to the individual timing latches in the Timing packets. Then the individual mirror Event packets must be grouped into cosmic ray "events". This is done by declaring a new "event" has begun after a certain time, typically 100 uS, after the last mirror Event packet seen.

Along the way various reference and monitoring packets must be tracked and sorted accordingly. The Flag and Adjustment reference packets help establish the absolute time. The monitoring packets include Minute, Volts, GPS, Status, and Notes. Minute packets contain a once per minute mirror report specifying tubes thresholds, countrates, total mirror triggers, and other information. Volts packets contain the HV tube readback values allowing tube voltages to be checked for stability. GPS packets report status messages from the GPS clock unit, typically noting the GPS satellites visible, their status, and the timing accuracy. Status packets record the network status between the central computer and each individual mirror. Note packets record operator notes, including the operator entered weather code, as well as any command which changes the running conditions of the system.

5.1.2 HIRES Event Calibration

After event building, the "events" are calibrated in order to determine the correct firing time, and the photon number in each channel. The details of the electronics channel calibration are

given in chapter 6. The calibration data used is collected twice a night, once before the start of data collection and again after the end. Electronics channel calibration is accumulated by injecting square pulses of known width and amplitude just prior to the preamp and recording the tube response. Relative tube sensitivities within each mirror are obtained by shining a pulse of laser light, carried from the central YAG laser trailer via fiber optic, from the center of the mirror onto the cluster face. Since the YAG light output at each mirror varies, mirror–mirror gains are not factored into the calibration at this point.

5.1.3 HIRES Track Filtering

Following calibration, the events are scanned to pick out events with track like properties. This can be done using spatial and/or temporal information. Ideally the algorithm should become more sophisticated after the simplest techniques have eliminated many candidates. For simplicity the filters operate at the mirror level. If any mirror in the "event" passes through the filters then the "event" as a whole is passed.

The first filter is a Rayleigh filter. The idea is to compare the track length with that expected from a random walk for the same number of tubes. In practice all pairs of hexagonally adjacent triggered tubes are considered. A rough "direction" vector, the Rayleigh vector, is obtained by summing individual unit vectors, which are formed by drawing a vector from the earlier tube in each pair to the later tube. There are six of these basic unit vectors. In a noise event, the individual unit vectors should be uncorrelated, leading to a random walk based Rayleigh vector with length $\sim \sqrt{\mathrm{n}}$, where **n** is the number of contributing vectors. For a genuine track the individual unit vectors should point more or less along the track, such that the Rayleigh vector should have a length closer to **n**. A Rayleigh vector which is long compared to $\sqrt{\mathrm{n}}$ has a small probability for occurring by chance in a noise event. The Rayleigh filter can be adjusted by a user parameter (**plogthresh**), which gives the (minus) logarithm of the fraction of random events which are allowed to pass the Rayleigh filter. For example, a value of 3 indicates that only one random event in 10^3 events should get through.

The second filter is called Scanner. It is invoked when the result from the Rayleigh filter is borderline. It requires more processing, but takes full advantage of spatial and temporal information.

Scanner begins with a time ordered set of tubes as its input. First, it discards tubes which clearly occur before or after the event. If t_i, where $i = 1...n$ represent the tube times, scanner first finds b such that $\sum_{i=2}^{b} \max((t_i - t_{i-1}), 500\text{nsec})/(b-1)^2$ is minimized. Then it finds $a < b$ such that $\sum_{i=a}^{b} \max(t_i - t_{i-1}, 500\text{nsec})/(b-a)^2$ is minimized. If the number of remaining tubes, $(b - a + 1)$, is less than 5 the event is rejected ($ISTAT = 1$). The event is also rejected if the time covered by these tubes is less than 250 nsec ($ISTAT = 2$). This eliminates many Cherenkov blasts.

Scanner next attempts to make a basic plane fit from the remaining tubes. Two sets of tubes are formed from the start and end of the range $[a, b]$. If the number of remaining tubes is less than 30, the tubes are divided into the two sets: $\mathcal{S} = [a, (a+b)/2]$ and $\mathcal{E} = [1+(a+b)/2, b]$; otherwise, the sets, $\mathcal{S} = [a, a+14]$ and $\mathcal{E} = [b-14, b]$ are used. Then a set $\mathcal{C}$ of cross products of the tube directions for all pairs tubes with one tube taken from S and the other from E is computed. If there are more than 40 such pairs, the scanner plane fit is derived by averaging all the cross products; otherwise, a direction clustering algorithm is used. For each vector cross product $c \in \mathcal{C}$, the sum, $\sum_{c' \in \mathcal{C}}^{c' \neq c} c \cdot c'$ (if vector separation is less than 5 deg) is formed. The element of $\mathcal{C}$ with the largest sum is assumed to represent the plane normal direction. The event is rejected if all sums are zero ($ISTAT = 3$).

Tubes lying more than 3 degrees from the fitted plane are discarded. If fewer than 5 tubes remain ($ISTAT = 4$) or the distance from the first tube to the last tube is less than 5 tubes long ($ISTAT = 5$), the track is rejected. If the linear correlation of tube times with position along the track is poor ($ISTAT = 6$) or the angular track speed is too fast ($ISTAT = 7$), the event is rejected. The cut on the time-vs-position correlation is given by **sigcut**, which is a parameter derived from the input value of **plogthresh**. The angular speed is compared with a minimum **speed** parameter computed from the input **dkmcut** value. Events which

pass these tests are declared tracks ($ISTAT = 0$). Summary data on the number of events in each ISTAT category are printed at the end of nla execution.

5.1.4 Programs

The event building, calibration, and filtering process have been bundled into one group program called **nla**. The final output is a track (*.trk*) file. **nla** has two drawbacks. First, events passing the filters are written out to calibrated *.trk* files. Second, the resulting text based *.trk* files are unwieldy in size and cumbersome to use.

In 1995, the HIRES group installed an improved bank oriented data handling system. It is somewhat erroneously called the Data Summary Tape (DST) system, "summary" being misleading because most DST files contain banks describing the raw and calibrated data in addition to any processed results. Under the DST system, the functionality of **nla** was broken into three logically separate programs, **dstraw**, **dstcal**, and a rayleigh filtering program. **dstraw** builds the events from raw datafiles, writing a RAW1 bank for each event and inserting calibration and monitoring banks resembling the calibration and monitoring packets in the raw datafile. **dstcal** uses the same nightly calibration files as **nla** and adds a PHO1 bank to each event containing a RAW1 bank.

Although the DST system is cleaner and would simplify the merging described in the next section considerably, part of the HIRES–MIA data processing relies on **nla** for historical reasons. Only after the merging is complete is the resulting dataset converted to DST format for analysis processing.

5.2 Event Merging

HIRES–MIA–(CASA) event merging can only be described as a Byzantine process. There are two reasons for this. First, the CASA–MIA detector was not originally designed to work in coincidence with a HIRES detector. Second, HIRES software was not originally developed in a flexible manner.

The event merging begins with the nightly processing at HIRES. Because the CASA–MIA data collection rate is around 1 Gb/day it is necessary to identify a candidate set of MIA–(CASA) events and set these aside. This must be done within 24 hours; otherwise, the CASA–MIA data is removed to tape and the merging effort becomes considerably more difficult and bureaucratic.

5.2.1 Candidate Coincidence Selection

The candidate events are selected based on two criterion. The first is called the track bit, denoted *trkbit*. This is the flag set in the CASA–MIA datastream whenever the receipt of the flasher from HIRES requests a MIA readout or occurs within 50 uS after a MIA Common Stop. In the latter case, another detector, almost always CASA, forced a MIA readout and shortly thereafter the HIRES flasher was received. The second criterion is called a time match, denoted *timmat*. This occurs when one of the candidate HIRES times falls within 3 msec of a MIA-(CASA) event. The list of candidate HIRES times, the *mMMdDDpXX.casa*, files are generated from the HIRES events passing the nla filter. These files are automatically transfered via ftp to the CASA-MIA computers early in the morning. The time match window is so large because when the event merging began both detectors were using WWVB clocks which are good to only 1 msec. Furthermore, the WWVB clocks often drifted as much as 2 msec with respect to each other.

Data merging must await the completion of the PASS0 process on the two CASA runs (1–7 UT and 7-13 UT) which might overlap HIRES data. Since this processing requires at least five hours per file, the first part of the extraction of candidate events occurs around 19 UT. This is done by the HRMERGE program. Two types of output files are produced. The first are *RUNxxxxxx.HRMERGE* files, which contain PASS0 processed extracted events, where xxxxxxx designates a CASA run number. The second type of output is an *hrm* file of the form *HRM_yYYmMMdDD.LOG*, which contains a list of matched Jevents.

Each match in the *hrm* file is given a code of the form Fxy, where x represents the trkbit and y represents the timmat. The code 0 indicates that the trkbit or timmat did not occur. The code 1 indicates a HIRES–MIA–CASA match and 2 indicates a HIRES–MIA match. The following is a complete list of the valid match codes:

- **F11** This indicates a HIRES–MIA–CASA coincident event which both matched in time and where a flash was received from HIRES. Despite the wide time match window, later GPS based timing shows that $\sim$ 90% of F11 matches are genuine coincident events. These matches occur $\sim$ 1/hr.

- **F22** This indicates a HIRES–MIA coincident event which both matched in time and where a flash was received from HIRES. Similar the F11 case, GPS based timing shows that $\sim$ 90% of F22 matches are genuine coincident events. These matches occur $\sim$ 2/hr.

- **F01** This indicates a HIRES–MIA–CASA coincident event where a flash was received from HIRES but the event was not on the list of times transferred from the HIRES computer. These occur $\approx$ 50/hr. This is the expected accidental rate given that the HIRES event rate is 10.3 Hz, the MIA trigger rate is about 30 Hz, and the MIA holdoff time, in which the HIRES flasher may be received, is 50 uS. N.B. even though the HIRES mirror trigger rate for the whole detector is 13 Hz, there are about 1.3 mirrors/event. F01 events can also occur when light, other than that from the flasher, is accidentally scattered into the flasher receiving unit. The F01 rate serves as a sanity check on the matching process.

- **F02** This indicates a HIRES–MIA coincident event where a flash was received from HIRES but the event was not on the list of times transferred from the HIRES computer. These occur $\sim$ 2.4/hr, considerably less frequently than F01 events. The difference arises because whenever CASA trigger it forces a readout of MIA regardless of the number of muon counters hit. This behavior is necessary for doing gamma ray astronomy. On the other hand, the receipt of a HIRES flasher only causes a MIA

readout if the minimum conditions (MIA self trigger) of 3 muon counters/patch and 6 patches have been met.

- **F10** This indicates a HIRES–MIA–CASA coincident event on the list of times transferred from the HIRES computer for which no flash was received. Usually this indicates that the flasher was not working, the flasher was not turned on, or there was a problem with the receiving unit electronics. Sometimes the weather is at fault either causing the receiving unit window to frost up or via a low haze which scatters the flasher light. It is quite possible for either of these cases to occur and still have good overhead weather suitable for stand alone HIRES running.

- **F20** This indicates a HIRES–MIA coincident event on the list of times transferred from the HIRES computer for which no flash was received. These are almost nonexistent. Since by definition CASA did not force a MIA readout and HIRES did not promote a MIA self trigger to cause a readout, the only way this can happen is an accidental coincidence where some other instrument, such as the Cherenkov telescopes, promoted the MIA self trigger.

- **F03, F30, F33** These are theoretically permitted codes indicating a HIRES–CASA coincidence without MIA. Since all CASA events are supposed to force a MIA readout, these codes indicate a problem with the CASA–MIA array. Experience shows when these problems occur, they are quite serious. Any CASA–MIA run containing any matches of these type is excluded from the HIRES–MIA dataset.

5.2.2 2nd Round merge processing on the HIRES machine

Once the candidate event have been extracted from the CASA datastream, the remainder of the merging can proceed at a leisurely pace. Usually this is done once per monthly run, although each individual night is handled separately. The exception to this is that calibration information from nearby nights may be used if it is missing or invalid for a particular night.

The process begins by running **nla** on each hires raw file in a special mode which time sorts the HIRES packets into an ordered raw file one step prior to building events and imposes no cuts on the data. A special program reads the *hrm* file and extracts the desired events from the ordered raw file and places them into another raw file. **nla** is then run on this file to produce a calibrated text based *.trk* file. The **nla** filtering parameters are set such that essentially no events are discarded during this process. This is important because we now want to keep the F01 and F02 matches which did not pass the quality filtering cuts originally. It is an annoying drawback of **nla** that the production of a *.trk* file can not be carried out without throwing away tubes with fewer than 10 tubes. However this does not matter much because it is ultimately desirable to place a cut at least this restrictive early in the analysis stage.

The resulting *.trk* files are then run through a plane fitter which determines the plane containing the shower and the HIRES detector and produces a *.pln* file. This program only relies on the triggered tube directions and their amplitudes; it does not use timing information. The plane found is called the Shower–Detector plane (SD–plane). Because the mirrors are at differing locations, it is more proper to speak of the Shower–Mirror plane formed with each mirror, but for this first fit it is reasonable to treat the HIRES detector as a point detector since the mirrors are separated by tens of meters while the events are thousands of meters from the detector. By definition, the event trajectory lies within the SD–plane.

The plane fitter also flags down noise tubes. Another program removes these tubes from the dataset. Events with fewer than 10 good (i.e. not noise) tubes are also removed. It is also possible for the plane fitter to fail in which case the event will drop out of the datastream. However, in practice the plane fitter is quite robust. Far fewer than 1% of the events are discarded for this reason.

The last step on the HIRES computer is to combine the *.pln* file results with the CASA timing information and match code. The output file is then stripped of some unnecessary

text in order to facilitate easier processing on the CASA–MIA VAX machine. The result is a file of the form *yYYmMMdDD.strp*, a *.strp* file. This file is automatically transferred to the CASA–MIA machine via ftp.

The final step in the merging is combining the extracted CASA–MIA events with the extracted HIRES events. In other words, data in the *.strp* files must be combined with data in *.HRMERGE* file. This is done by a program called HRMERGE2. The resulting file is of the form *RUNxxxxxx.HRMERGE2*, with one file for each CASA run containing coincident data.

5.3 Analysis Programs

Analysis begins by converting the merged events in the *.HRMERGE2* files from the CASA–MIA data format to HIRES DST format. This is done by the program **dtod**, which combines the entire converted result into one master file.

Each event in the master DST file contains the following DST banks:

DST banks in each event of converted file	
Bank	Description
RAW1	HIRES tube qdca, qdcb, tdc values
PHO1	HIRES calibrated tube results
MUON	MIA muon counters hit and hit times
CAP0	CASA counters (present only if event is a HIRES–MIA–CASA coincidence)
CTIM	MIA–CASA latch time for event
PLN1	Crude HIRES plane fit results
CMAT	Match type (F11, F22, ...)

This file contains 43274 events, covering the period 23 Aug 1993 through 24 May 1996. Two basic cuts are imposed immediately:

1. At least 15 deg track length

2. At least 40 muons for HIRES–MIA events and at least 80 muons for HIRES–MIA–CASA events.

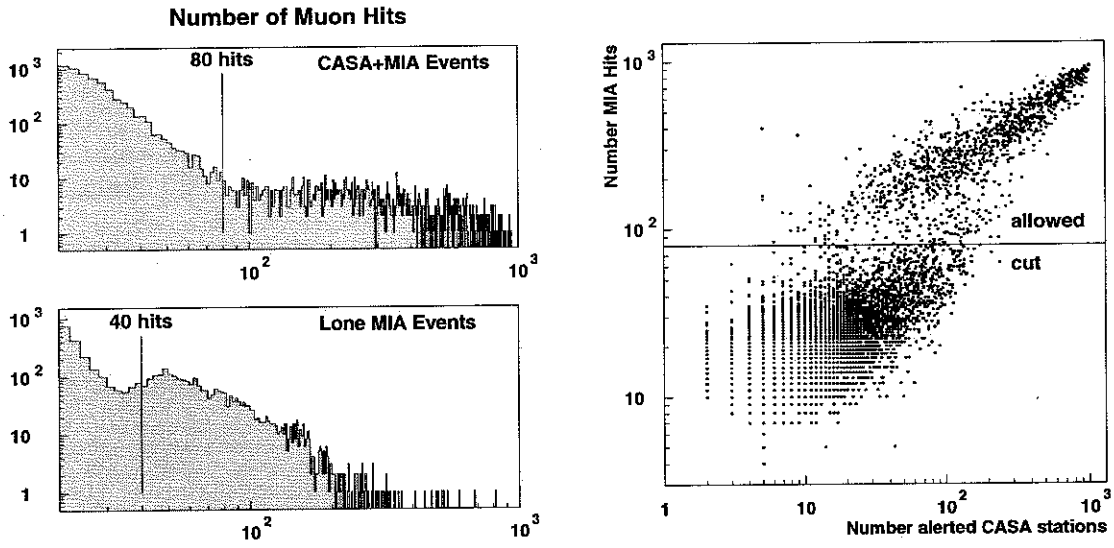

Figure 5.1: Number of muon counters in candidate coincident events. The figure on the right shows the number of muon counters vs. the number of alerted CASA boxes for candidate coincident events. Two populations are clearly present. A cut at 80 muons eliminates most accidental coincidences.

The first cut removes events which are certain to be fitted poorly due to a lack of tubes or/and limited visible track grammage. The second cut eliminates many accidental coincidences. Figure 5.1 shows the effect of the muon cut. The figure on the left shows the number of muons hits for both HIRES–MIA events and the HIRES–MIA–CASA events and the location of the cuts. The figure on the right shows the number of muon hits versus the number of alerted CASA stations for the HIRES-MIA–CASA events. Two populations are clearly present. The lower population is comprised of accidental coincidences.

Following these Basic Cuts, the 2881 events remaining are sent through four programs: **hbrd_traj.run**, **gpln**, **bindata.run**, and **pfl**. The first determines the most likely shower trajectory using information from HIRES and MIA. It also determines the number of muons in the shower. **gpln** makes very small "micro" corrections to the trajectory prior to determining the flux seen at each phototube. This is important because the tube signal recorded depends strongly on how the light crosses the phototube, loosely speaking whether the light spot goes through the center of the tube or merely clips an edge. **bindata.run** determines

the flux seen at each phototube and bins the flux arriving from the shower in 1 degree bins along the shower path. Finally, **pfl** determines the shower parameters ($X_{\max}$, X_0 , and Energy) based on the trajectory and the binned flux. Each of these programs adds one or more DST banks to each event.

5.3.1 Trajectory Fitting with hbrd_traj.run

HIRES–MIA trajectory fitting proceeds in a series of steps designed to progressively refine the result. This strategy is used in order to reduce the number of cases where the minimizing routines employed by the fitters fail. The overall strategy is to make crude trajectory fits in order to determine which muons are intime, improve the fit, and finally determine the number of muons in the shower based on the final fit. A bootstrap statistical technique is used to determine all statistical errors.

A trajectory consists of four independent values which may be parameterized in several ways. One parameterization is the core at some height (usually the "ground") and the shower direction. Another parameterization is the SD–plane normal, the impact parameter with the HIRES detector, R_p, and an impact angle, Ψ, as illustrated in Fig 5.2. The latter is a useful parameterization because the SD–plane is usually fairly well determined by plane fitting alone, while R_p and Ψ are less accurate. In the discussion which follows, *trajectory* is taken to mean the above in whatever form is most useful, while *direction* means a two parameter quantity giving only the direction of the shower.

The detailed **hbrd_traj.run** algorithm is:

Find approximate shower direction

1. Since it is known that the trajectory lies within the SD–plane, (found by the plane fitter during the merging process) the first direction guess is arbitrarily the "most vertical" direction laying within the SD–plane. Mathematically, this means choosing the vector which results when a vertical vector is rotated in the plane formed by itself and the SD–plane normal until the vector lies within the SD–plane.

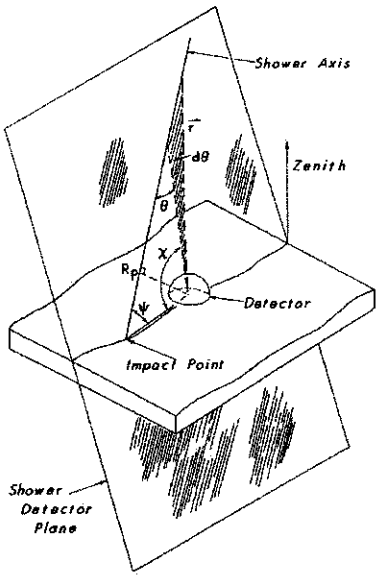

Figure 5.2: Shower reconstruction geometry

At this point the muons are assumed to arrive on a plane front, whose normal vector is this "most vertical" direction. After recalculating the muon arrival times relative to this plane front, any muon arriving more than ± 1000 nS from the median muon arrival time, is assumed to be out of time. This is a very loose cut designed to discard very obvious accidental muons without discarding any muons simply due to the arbitrary nature of the initial direction guess.

2. The times of the remaining muons are used to determine an arrival direction assuming the muons arrive on a plane front. This is done using a least squares fit. Here the arrival direction is not constrained to the SD–plane. Following the fit, the muon times are recalculated relative to the new plane front. All muons falling inside a time 345 nS time window centered on the median muon arrival time, are considered to be intime. If necessary the time window is successively widened 4 nS at a time to insure at least 20 muons fall within the intime window. All muons falling outside the intime window are assumed to be accidentals and are ignored in subsequent steps.

3. The times of the "intime" muons are used to determine a direction assuming the muons arrive on a plane front. This fit is not constrained to the SD–plane. If this result lies

more than 10 degrees from the SD–plane, the event is rejected. This usually indicates an accidental coincidence.

From here on the goal is to find a complete trajectory rather than just a direction.

Find the trajectory

1. Confine the direction found above to the SD–plane via projection.

2. Make a rough determination of R_p. At this point, the plane normal and Ψ are roughly known, the latter coming from the direction result. Therefore, in the (plane normal, R_p, Ψ) trajectory representation, only R_p is unknown. The HIRES tube times are used to determine R_p via a two parameter least squares fit. This is essentially an ordinary HIRES monocular timing fit:

$$(t_i)_{\text{expected}} = t_0 + \left(\frac{R_p}{c}\right) \tan\left(\frac{\pi - \Psi - \chi_i}{2}\right) \quad (5.1)$$

$$\chi_i = \text{viewing angle of } i\text{'th tube (see figure 5.2)} \quad (5.2)$$

$$c = \text{speed of light} \quad (5.3)$$

except that only R_p and t_0 need to be determined since Ψ is known.

3. Refit the direction assuming the muons arrive on a cone shaped front rather than a plane front. For this fit the arrival direction is not constrained to lie within the SD-plane.

The quantity T_d shown in Figure 5.3 is the average time delay of muons from the shower plane. Several experiments have determined this quantity as a function of distance from the shower core[45, 11, 60]. For the HIRES–MIA dataset, we use the form: $T_d = 0.0655\ r + 0.0001199\ r^2$, where r is in meters and T_d is in nS. This result was derived by the CASA–MIA group based on a large sample of CASA showers.

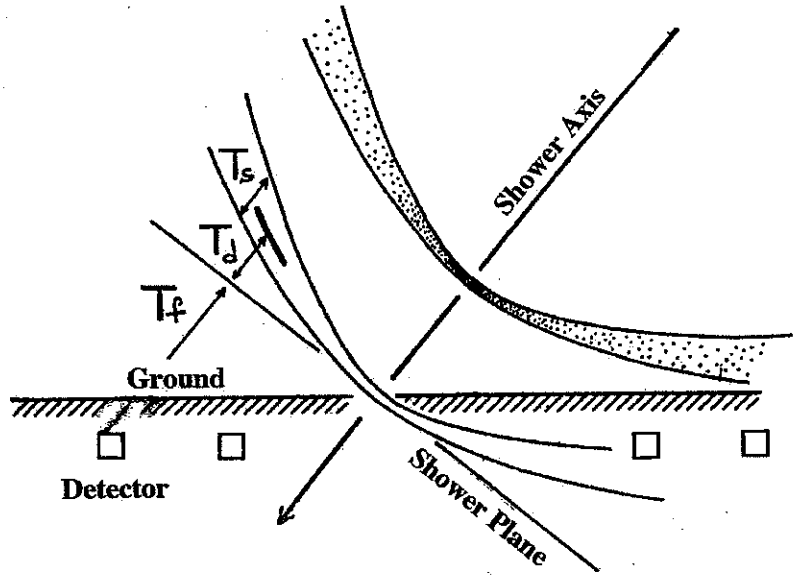

Figure 5.3: Diagram of an air shower hitting the buried muon counters. T_d is the average time delay of the shower particles from the shower plane.

4. Redetermine R_p with a HIRES monocular fit as before using the improved direction found in the last step.

5. Perform an iterative procedure restricted to the SD-plane, alternatively fitting Ψ by using the muon arrival times based on a cone front followed by fitting R_p via a monocular HIRES timing fit. The iteration ends when the R_p variation from cycle to cycle drops below 10 meters or a maximum number of tries is exceeded. In the latter case, the event is rejected.

6. Adjust the SD-plane. This is done using a tube "amplitude weighted" fit. The plane normal vector allowed to vary while R_p and Ψ are held fixed. The quantity to be minimized is:

$$\sum_{\text{tubes}} \text{Signal}_i \ \text{offpln}_i^2 \tag{5.4}$$

where Signal_i is the signal of the i'th tube in photoelectrons and offpln_i is the "off–plane" angle of the i'th tube. This is the angle between the center of the tube and the

plane formed by the mirror and the track trajectory. Since a separate plane is formed for each mirror, this fit fully accounts for parallax, unlike the original plane fit (see section 5.2.2).

7. Perform the same iterative procedure as above restricted to the new SD-plane. This may seem unclear now that a parallax based correction has been made. It just means that the iteration will only move the trajectory so as adjust R_p and Ψ in the plane formed by the trajectory found in the last step and the centroid of the detector. The result here is the final trajectory.

Find the Muon Multiplicity

Finding the muon multiplicity is comparatively easy. First, the (plane normal, R_p, Ψ) form of the trajectory found above is translated into the (direction, core) representation. The fit is a one parameter log likelihood fit for N_μ. For each N_μ guess we calculate the Poisson probability of each alive MIA counter triggering given its distance from the core and assuming the AKENO lateral distribution function. Naturally, both hit and unhit counters are factored into the log likelihood fit.

Determine the errors via bootstrap

A bootstrap technique [43] is used to determine statistical error on the trajectory. Twenty five sets of HIRES tubes, drawn from the original set with replacement, are selected. For each set the trajectory parameters and muon size are recomputed. The widths of the resulting distributions for each parameter give an estimation of the errors.

The muon counters are not replaced as part of the bootstrap technique because the binary nature of their result violates the required conditions for bootstrap. The error returned from the log likelihood is used instead.

5.3.2 Micro Correcting the Trajectory with gpln.run

gpln makes very small trajectory adjustments. These adjustments are important because the tube signal is strongly affected by how the light spot crosses the tube, i.e. whether it goes

through the center or clips the edge. Although the most accurate "path length" correction must be determined from raytracing results and empirical data, the relationship for the correction is close to:

$$\text{Signal Observed} = (\text{Maximum Signal})\ \exp\left(\frac{\text{offpln}^2}{\beta^2}\right) \tag{5.5}$$

where offpln is the angle between the tube center and the shower–mirror plane, and $\beta = 0.5$ degrees.

Consider momentarily a given mirror. Within the shower–mirror plane containing the shower and the mirror, adjusting the trajectory R_p or Ψ will not affect how the light spot crosses tubes in that mirror. Only changing the shower–mirror plane normal will have an effect. Although the shower–mirror planes vary rather slightly from mirror to mirror, they are all close to the plane formed by the shower and the average mirror position (the detector centroid). It keeps things simple to vary only two trajectory parameters. Therefore **gpln** varies the normal of the plane, which contains the shower and the detector centroid.

Unlike the plane normal adjustment in **hbrd_traj.run** which uses an "amplitude weighted fit", **gpln** uses a superior "amplitude predicted" fit. The plane normal is adjusted to minimize:

$$\chi^2 = \sum_{\text{tubes}} \frac{(\text{Signal}_{\text{observed}} - \text{Signal}_{\text{predicted}})^2}{\sigma_i^2} \tag{5.6}$$

where the predicted signal is calculated using equation 5.5. The problem with using this equation is that it appears to require knowing the maximum signal when the tube lies exactly in the shower–mirror plane. To get around this, the shower is considered to have a fixed line source amplitude within each mirror. The signals from all the tubes in a mirror are used to determine the best line source amplitude. This is clearly an imperfect technique, but for the current purpose works well. For each tube σ_i^2 is computed from the Poisson statistics and sky noise added in quadrature. For the magnitude of the signals seen by the HIRES

tubes, the difference between gaussian and poisson statistics is negligible, so in practice the former are used.

5.3.3 Binning the Light Flux with bindata

bindata arranges the tube signal data into a form useful for profile fitting. The goal is to calculate the light flux (pe/deg-m^2) arriving from the shower at regular intervals, typically 1 degree bins. Each tube is assigned to a bin and more than one tube may fall in a particular bin. This does not present a problem. Each tube in a bin is assumed to be an independent measurement of the flux at that bin. All the measurements along with their errors are combined in the standard statistical manner to give one measurement for the bin.

5.3.4 Fitting the Profile with pfl

pfl determines the shower parameters ($X_{\max}$, X_0, and $N_{\max}$) which characterize the shower development. The shower energy is readily obtained afterwards from these parameters.

Unfortunately there is no easy way to work backwards from the binned flux information to shower parameters. Therefore, the method used is to vary $X_{\max}$, X_0 , and $N_{\max}$ until the flux predictions at each bin match what is experimentally seen as well as possible. Mathematically, the following is minimized:

$$\chi^2 = \sum_{\text{bins}} \frac{(\text{bin}_{\text{predicted}} - \text{bin}_{\text{observed}})^2}{\sigma^2_{\text{bin}}} \tag{5.7}$$

Figure 5.4 shows a typical profile fit where all sources of light make a noticeable contribution. The dominant contribution here is the scintillation light. Direct Cherenkov, Rayleigh scattering, and Mie scattering are also present.

In order to predict the flux at each bin for a given $X_{\max}$, X_0 , and $N_{\max}$, the profile fitter requires:

- Model for shower development
- Model of atmospheric behavior

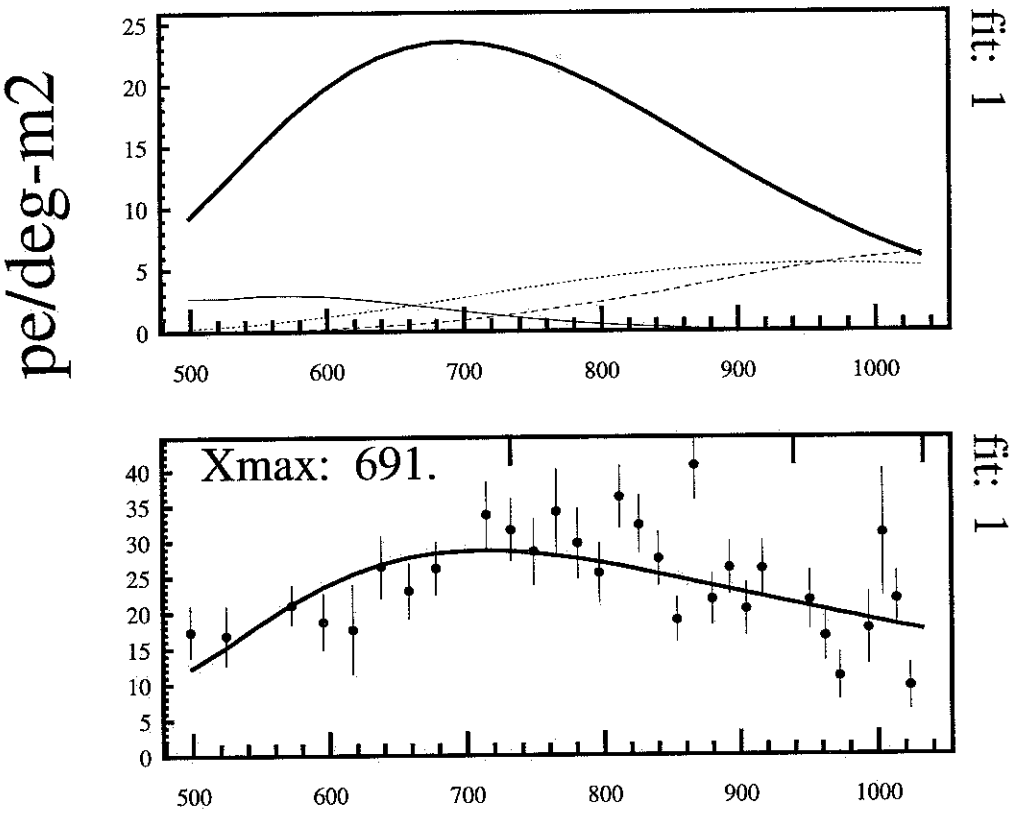

Figure 5.4: Fitted shower profile. The upper plot shows the expected light contributions from scintillation (thick solid line), direct Cherenkov (thin solid line), Rayleigh scattered Cherenkov (dotted line), and Mie scattered Cherenkov (dashed line). The lower plot shows the sum of all contributions compared with the binned tube data.

- Physics of the light production
- A few detector parameters

Shower Development

Shower development is characterized as a one dimensional shower where the particle number at each depth is given by the Gaisser–Hillas formula (see equation 3.1). Here λ is held constant at 70 g/cm^2.

Atmospheric Model

The atmosphere is treated in a fairly simple manner:

- Temperature at ground is assume to be constant
- Temperature is derated 6 °C/km
- Aerosol distribution is exponential (scale height: 1.2 km)

In principle these characteristics should be adjusted based on nightly information as discussed in section 6.6 but at the current time this is not done. For the comparatively close events such as the HIRES–MIA dataset variations in the atmosphere change the reconstructed parameters only slightly. Figure 5.5 shows the reconstruction of Monte Carlo generated events assuming drastically different atmospheric parameters. BBAER is the aerosol concentration at ground level and ATSCL is the atmosphere scale height for aerosols. Halving or doubling ATSCL has negligible impact. Halving or doubling BBAER has a greater impact, but the change in $X_{\max}$ is still not worse than 11 g/cm^2 even in this unrealistically extreme case. Similarly, the effect on the reconstructed energy is small compared to other sources of error. Figure 5.6 show the effect of assuming the atmospheric temperature at the ground is -20, -10, +10, and +20 °C different from the annual average temperature, AVTEMP, assumed in the program.

Light Production

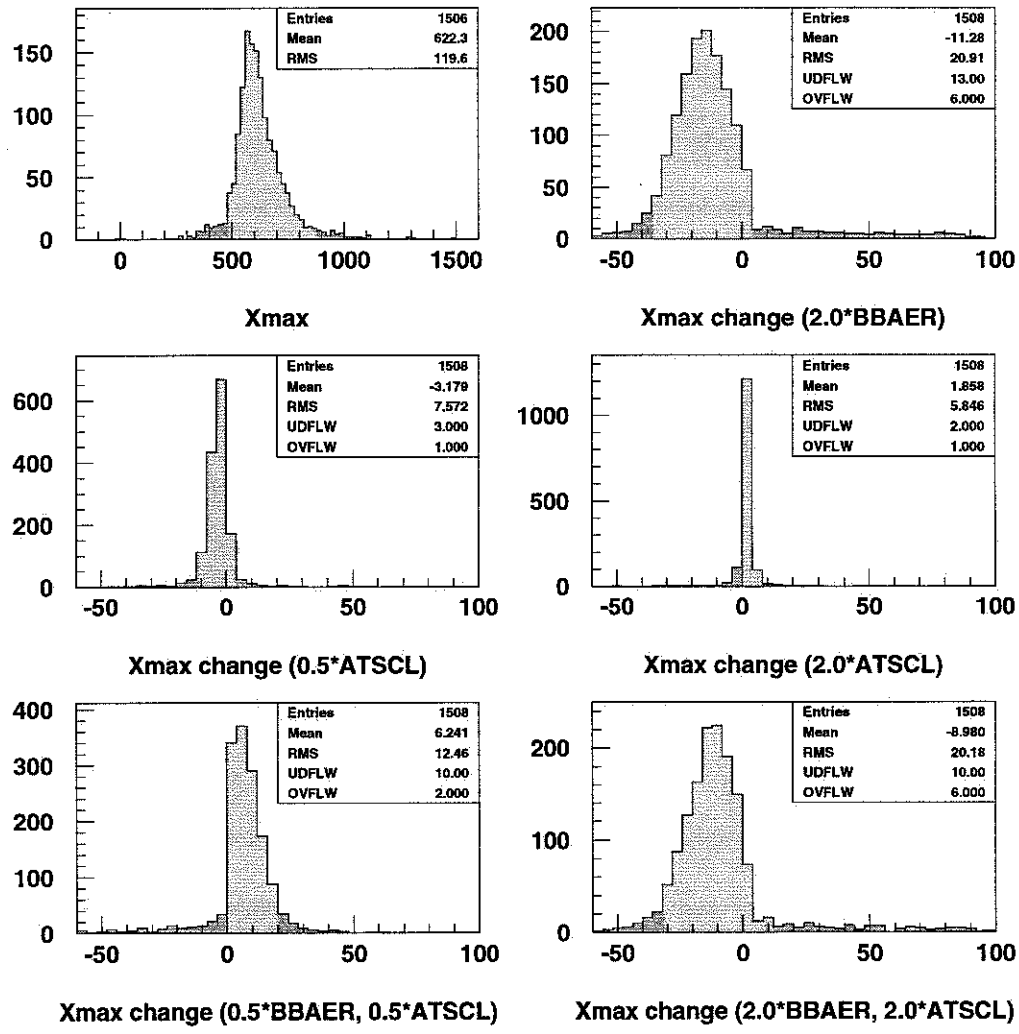

Figure 5.5: Shift in reconstructed $X_{\max}$ for part of HIRES–MIA dataset assuming different atmospheric parameters. BBAER is the aerosol concentration at ground level. ATSCL is the atmospheric scale height.

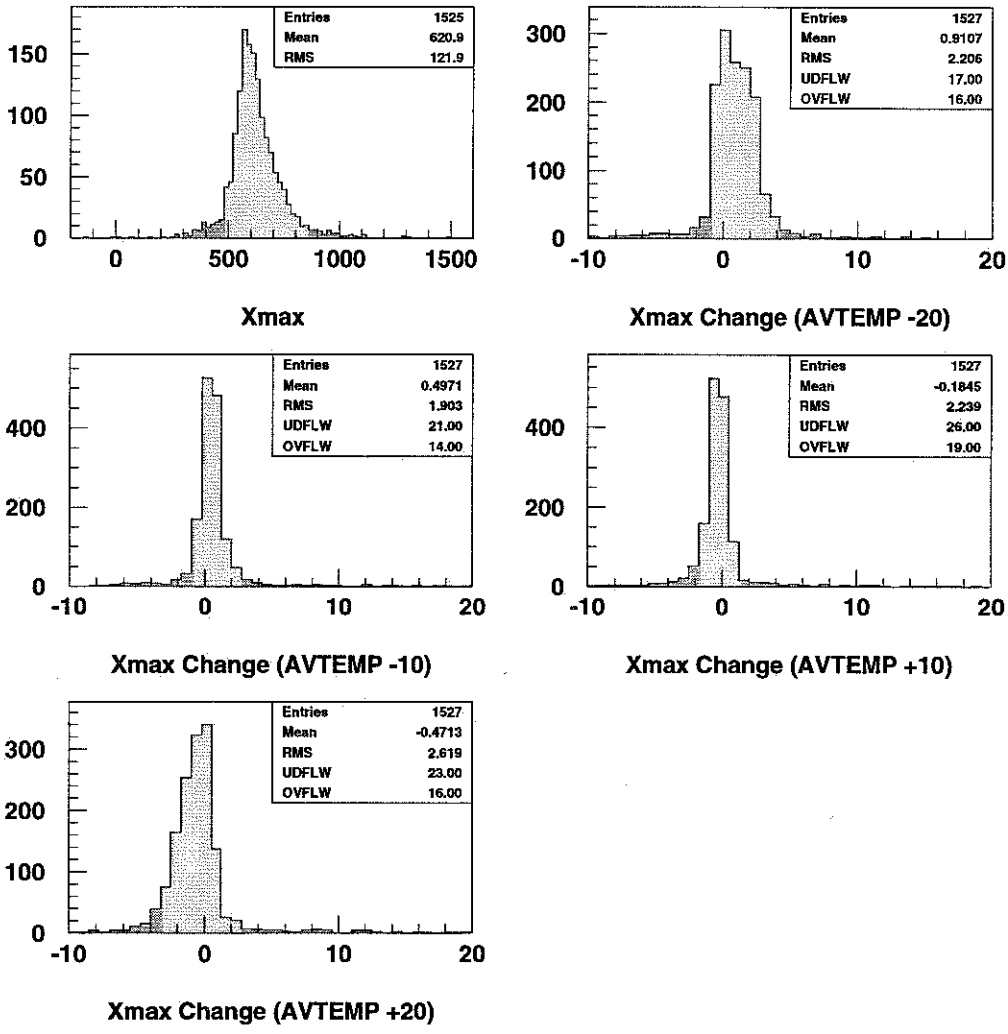

Figure 5.6: shift in reconstructed $X_{\max}$ for part of HIRES–MIA dataset assuming different temperatures at ground level. In all cases the temperature is assumed to decrease 6°C/km.

The light production physics begins with scintillation. The fluorescence yield at each point is proportional to the particle number. Bunner [19] pointed out that simple kinematic theory argues that the fluorescence yield for a band goes as $yield \sim \frac{\rho}{1+\rho B\sqrt{T}}$, where B is a constant, T is the absolute temperature, and ρ is the density. At the ground a typical band gives $\rho B\sqrt{T} \approx 31$ kg-m^{-3} $\times$ 1.85 m^3-kg^{-1}-K$^{-1/2}$ $\times \sqrt{273} \approx 900$. This is large compared to unity even high in the atmosphere where ρ is smaller. Therefore the fluorescence yield $\sim T^{-1/2}$, which is what is used in practice. There is also a mild pressure dependence. A recent Japanese result [44] showed no significant change until the pressure drops below 100 mmHG. This drop was not taken into account during profile fitting. The fluorescence decay times are all very fast, 10–50 nS.

Calculating both Rayleigh and Mie scattering requires keeping track of the Cherenkov buildup as the shower progresses. Cherenkov light production per charged particle varies along the shower because the critical energy depends on the air density, which in turn depends on the height above the ground. Adjusting for this requires assuming the energy distribution of charged particles, primarily electrons, in the shower. Although this varies somewhat as the shower progresses, a constant energy distribution was used during profile fitting.

Rayleigh scattered light is a straight function of the density of scatterers and the standard ω^4 factor for each of frequency bins. As discussed above, the aerosols distribution is characterized by an exponential. A standard phase function is used to determine the scattering.

Light attenuation between the point of production and the detector is treated by a standard attenuation formula, $\mathrm{I_{out}} = \mathrm{I_{in}} \exp(-x/\lambda_x)$ where x is the grammage between the shower and the detector and λ_x is a frequency dependent attenuation coefficient.

Detector Parameters

The necessary detector parameters needed to predict the flux seen at each phototube are:

- UV filter transmission

- Tube Quantum Efficiency vs. wavelength
- Mirror Reflectivity

These items are discussed in chapter 6.

Chapter 6

Detector Calibration

6.1 Introduction

The HIRES detector presents significant calibration difficulties. Unlike a typical particle physics experiment where the detector response to a well understood test beam can be measured, there is no test beam. This makes it necessary to understand absolute calibrations rather than just relative calibrations. Furthermore, the calorimeter, i.e. the atmosphere, can not be controlled. Instead, it must be measured and characterized at regular time intervals.

HIRES calibrations can be broken into five components: phototube response, mirror behavior, filter response, electronic response, and atmosphere. Phototube response includes the quantum efficiency as a function of wavelength, absolute gain as a function of applied voltage, temperature dependence, the 2-dimensional response function mapped across the face of the phototube, and the preamp gain. The mirror behavior includes mirror reflectivity and spot size, the latter varying with position. Filter response is a simple function of frequency. The electronic response includes electronic gain, nonlinearities at the low and high end, electronic noise, and time slewing. Finally, for the atmosphere, pressure and temperature, and humidity are measured. Cloud cover and cloud height are tracked and aerosols are measured.

MIA calibrations are comparatively simple. This is because each counter produces a binary result and all counters are permanently buried. The most important thing to understand is the muon detection efficiency as a function of muon energy. This is essentially constant around 93% beyond 1.05 GeV after rising from zero around 0.92 GeV. Punch through does occur and must be considered for CASA–MIA analysis. However, for the MIA–HIRES dataset the minimum muon cuts are high enough that any such coincidences are eliminated early from consideration. Because the cable lengths from the muon patches to the central MIA trigger unit vary with temperature and are up to several hundred meters, the lengths are measured every six hours as part of a standard CASA–MIA calibration.

CASA calibrations are fairly complicated. Since they do not bear directly on this work they will not be discussed here. A good discussion can be found in chapter 3 of H. Krimm's thesis [49].

6.2 Phototube Response

6.2.1 Phototube Test Station

In order to understand phototube response, a testing station was built at the University of Utah, as diagrammed below in Figure 6.1. Since this setup is described at length in a NIM paper [7], only a brief description will be given here.

The goals are to measure the phototube quantum efficiency, the gain as a function of voltage, and the uniformity across the tube face. The light source is either the 351 nm or 364 nm line of a Argon laser or the 325 nm line of a He-Cd laser. Most of the attenuation occurs during multiple reflections within a 2 cm thick quartz plate oriented at a 45 degree angle with respect to the incoming beam. At each surface, unwanted light beams are directed into light traps. The first transmitted beam is directed into a thermopile as one monitor of the beam intensity. The fourth beam is retained and directed towards the phototube. The light can be further attenuated along the way if required. Typical light intensity arriving at

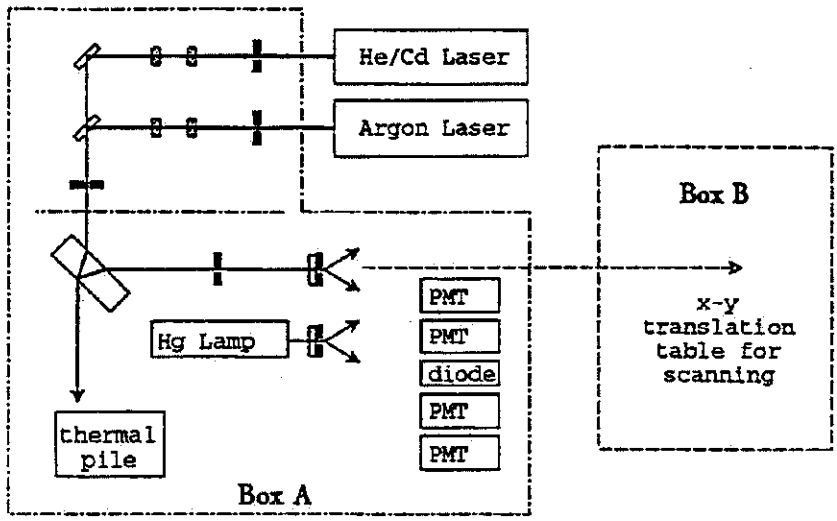

Figure 6.1: Phototube testing setup

the phototubes is 8×10^6 photons/cm^2-s, or 4.5 picoW/cm^2 at 351 nm, reduced some ten orders of magnitude from the input laser beam.

An NIST calibrated diode provides the absolute calibration for the entire system. The diodes used are linear over a very large range. For testing tube quantum efficiency and gain, a sliding tray allows the response of several tubes and the diodes to be measured in each cycle.

For scanning the tube surface the phototube to be tested is placed in a holder, which sits on top of crossed stepper motor platforms allowing computer controlled stage movement in the x-y plane. The same computer records the tube response and the beam monitor. The holder was later modified so that up to sixteen tubes could be scanned in one cycle.

The entire assembly is mounted on an optical table, painted flat black. The enclosure is aluminum anodized black. The covering lid is surrounded by multiple channel aluminum which fits snuggly into identical channel along the edge of the box.

6.2.2 Quantum Efficiency

The quantum efficiency depends on the cathode coating. HIRES contains two types of phototubes, EMI and Phillips. The quantum efficiency varies very little from tube to tube. A sample plot of a Phillips' tube efficiency measured at the factory is shown in figure 6.2. The phototube test station allows a cross check of the manufacturer at three important wavelengths in the fluorescence spectrum.

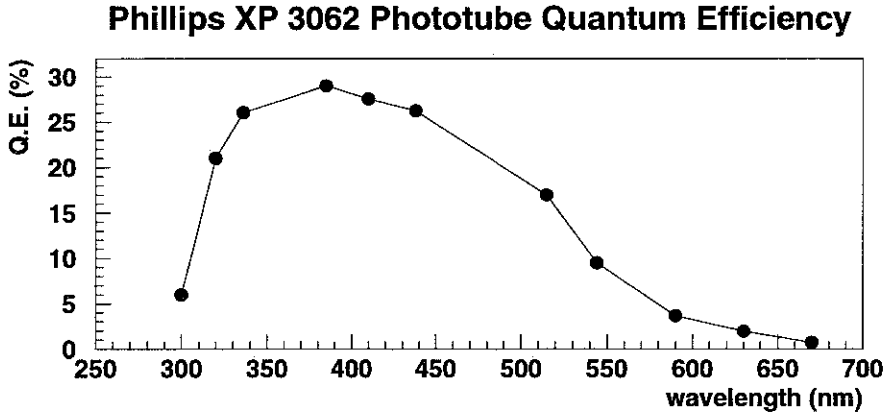

Figure 6.2: Typical Phillips XP 3062 phototube quantum efficiency as a function of wavelength

6.2.3 Gain as a function of Voltage

The gain as a function of voltage is measured in the test station described in section 6.2.1. The gain fits the functional form:

$$gain = A \times V^B$$

where A and B are determined for each tube. The distribution of measured values for all the tubes is roughly gaussian with $\ln A = -31.696 \pm .77$ and $B = 5.888 \pm .142$.

6.2.4 Temperature Dependence

The phototube gain temperature dependence is about 0.5%/°C. This is significant because the detector is operated over the ambient temperature range -15 – 40 °C. The tube clusters

are cooled with a fan in an attempt to maintain a uniform cluster temperature but no attempt is made to maintain a constant phototube temperature.

Each cluster contains a temperature sensor in the middle which is fed into the garbage board. Two additional sensors record the shed temperature and the crate temperature.

6.2.5 Response Profile

HIRES tubes were required to have a uniform response to $\pm 10\%$ across the face of tube, except for the area within 3mm of the edge. For HIRES1, the test station was used to map out a handful of tubes in order to check the manufacturer's claims. A typical accepted tube is shown figure 6.3. For HIRES2 the response profile was measured for all tubes.

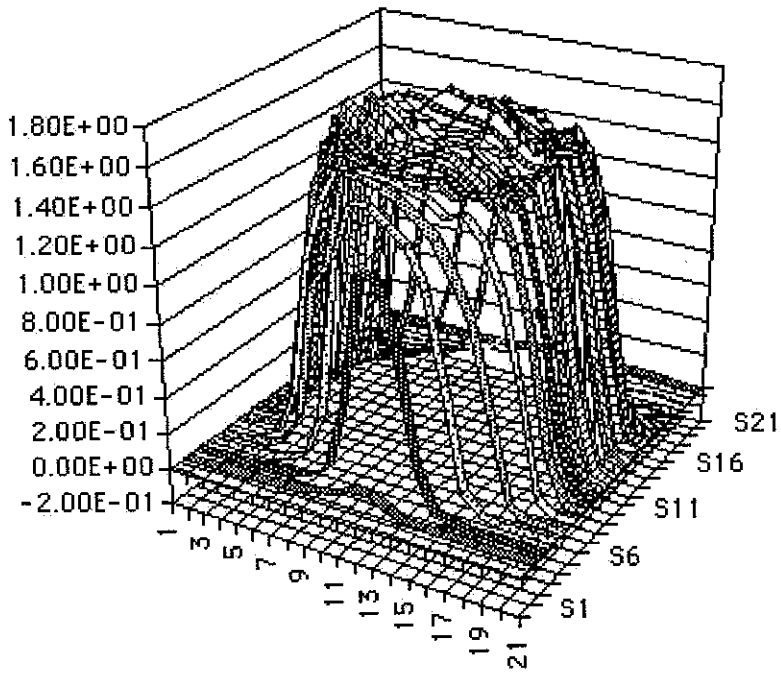

Figure 6.3: Tube response profile. Note the uniformity across the face and sharp drop off at edge. Axis units are linear and arbitrary.

6.2.6 Preamp Gain

Strictly speaking the preamps are part of the electronic amplification, but since each tube has one and they are placed at the base of the tube, it makes sense to refer to them here. Unfortunately, the design has significant nonlinearities at both the low end and the high end. The former is extremely relevant because a typical tube trigger is only a few qdc counts above threshold. Refer to section 6.5 for additional information.

6.2.7 Intermirror and Absolute Calibration

The intermirror and absolute calibration is performed with four well calibrated "standard" tubes which are moved from mirror to mirror. These tubes are calibrated to 2%.

6.3 Mirror Behavior

6.3.1 Mirror Reflectivity

The relative night to night variation in the absolute mirror reflectivity is measured by comparing the average phototube response for two situations. In the first, laser light is shined directly at the mirror via a fiber optic cup mounted in the center of the mirror. In the second case the fiber optic cups are mounted on the side of the cluster such that the light must first bounce off the mirror before entering the cluster. Unfortunately a series of tests conducted just before the prototype was disassembled revealed that small flexing of the teflon diffusers within the fiber optic cups could affect output on a nightly basis easily by 10% and likely worse. This may invalidate mirror reflectivity tracking.

The absolute mirror reflectivity is about 82%. It increases to about 90% when the mirrors are washed, which occurs about twice a year. Previous experience with the Fly's Eye mirrors, which were manufactured via the same process, indicates there is an apparent maximum dust accumulation achieved after one to two months running beyond which the reflectivity decreases rather slowly.

The output of the fiber optic cups is measured using a special device which covers the fiber cup and measures the light at a photodiode which is a fixed distance from the teflon diffuser. This provides one method of measuring mirror to mirror gain variations, but it is subject to the flexing problem mentioned above.

6.3.2 Mirror Spot Size

Imperfections in the mirror surface result in a central spot diameter of at least 0.5 degrees, equivalent to 2.0 cm on the cluster face. By comparison each phototube subtends 1.0 degree. A finite spot size is actually desirable because it reduces the variation in tube response along the track owing to dead space and variation along the tube face.

Because the mirrors are not parabolic and the focal region, i.e. the cluster, is too large to be considered a point, the size and shape of the spot vary across the cluster. The spot shape has been calculated with a raytracing program. Although the clover pattern of the mirror breaks azimuthal symmetry slightly, the effect is negligible. Therefore, the spot pattern can be characterized solely in terms of the angle from the mirror axis. Several cases are shown in Figure 6.4. As expected, towards the edges of the cluster, the spot coma grows worse and the central spot size grows slightly larger.

6.3.3 Mirror Crosstalk

It is possible for light from a given direction of the sky to bounce off the walls of the mirror sheds and silos and arrive at the wrong cluster. For the sheds the crosstalk is less than 1%. For the silos the problem was originally between 5% and 10%. After painting the interior a UV absorbing green, the problem was reduced to less than 1%.

6.4 Filter Response

The UV filters are 0.200 inches thick and cover the entire cluster. They were custom manufactured for HIRES in a single batch. The transmission of each was measured at several

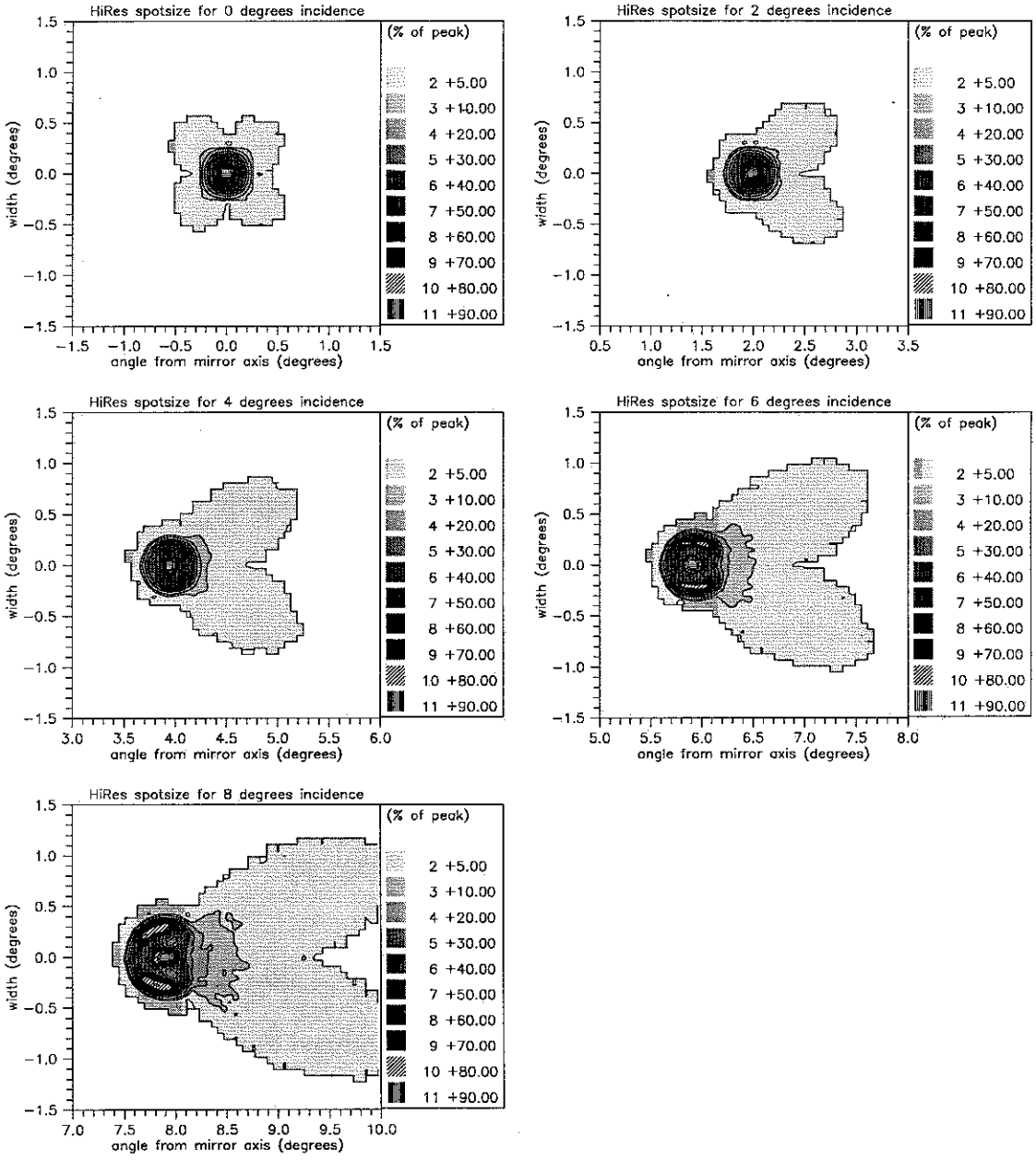

Figure 6.4: Mirror spot patterns for points laying 0,2,4,6, and 8 degrees away from the center of the cluster

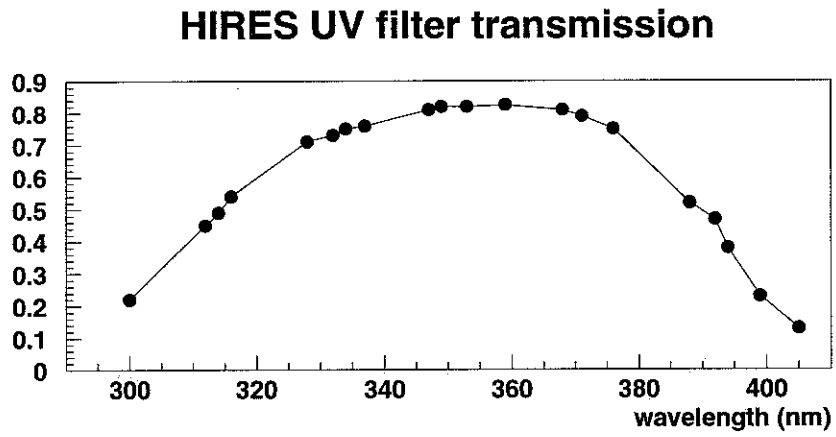

Figure 6.5: HIRES cluster UV filter transmission

locations. Average filter transmission at 355 nm ranges from 75% to 90%, averaging 86% over the entire detector. At present, the frequency dependence for each individual filter has not been measured. It is assumed to be the single measurement shown in figure 6.5 up to the normalization at 355 nm. The uniformity within each filter is about 3%. Figure 6.6 shows a typical mirror.

6.5 Electronic Response

The electronic system for each channel consists of a preamp in the phototube and one ommatidial board for every 16 tubes. A programmable pulser (PPG) board in each crate allows a square pulse of varying width and amplitude to be injected just before the preamp of each tube. By varying the pulse width and amplitude in software, the entire tube response can be mapped out. This is done both at the start and end of every run.

6.5.1 PPG and OMB linearity

The linearity of each PPG was checked against the integrated charge determined by a high quality digitizing oscilloscope. The deviations are small, but are nevertheless factored into the calibration. The OMB linearity is also quite good.

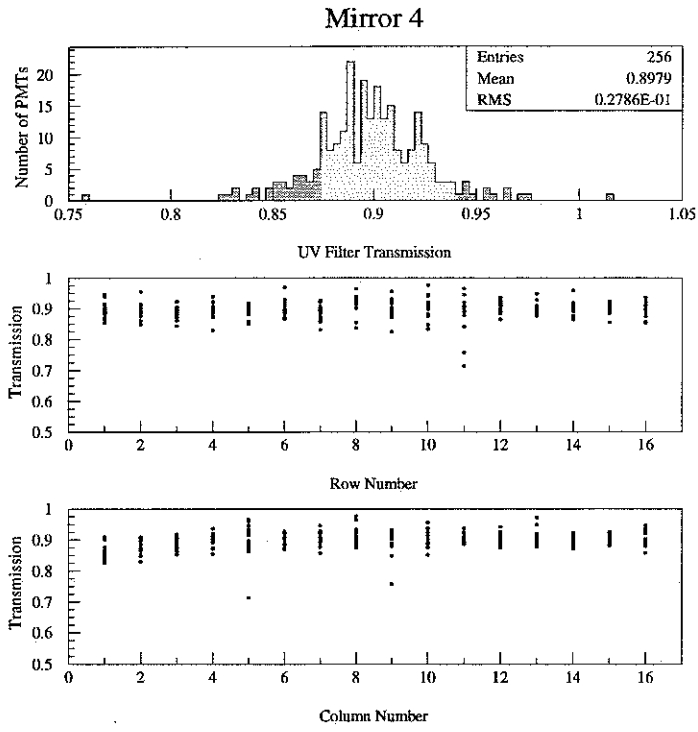

Figure 6.6: Tube to tube variation in filter transmission

6.5.2 Preamp linearity

Unfortunately, the preamp is nonlinear at both the high and low end of the qdc range. Figure 6.7 shows the typical response. This has been modeled by the three parameter functional form:

$$\text{gain} = (\text{asymptotic gain}) \times [1 - e^{(\alpha + amp)/\beta)}]$$

where α, β, and *asymptotic gain*, are constants for each channel. *amp*, the amplitude of the signal in volts, depends on the width of the signal. This in turn is estimated from the angular speed of the track across a mirror.

6.5.3 Pedestal Subtraction

The pedestal of each tube is calculated by running the system in a free triggering mode for 1 minute, collecting 300 snapshots per tube. These values should remain the same, whether

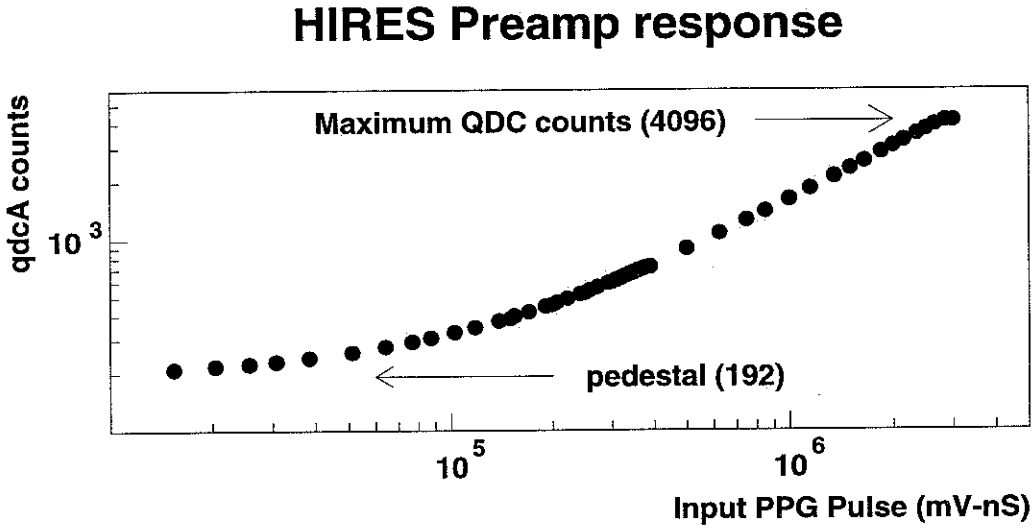

Figure 6.7: Representative preamp response in channel A to 500 nS PPG pulses of varying amplitude.

or not the tubes are exposed to the night sky. This is observed to be true to within 0.2 qdc counts.

6.5.4 Electronic Noise and Sky Noise

The RMS variation of the tube snapshots about the tube pedestal values gives a measure of the noise in the system. When data is collected with the tubes shielded from the night sky, the result reflects noise from the electronics. Typical qdcb RMS variations are 0.5 – 1.0 qdc counts. When data is collected with the tubes exposed to the night sky, the result reflects AC noise from the night sky added to the electronic noise in quadrature. Typical qdcb RMS variations are 4 – 6 qdc counts. After conversion to photoelectrons, these results give a background signal of 40 photoelectrons in the A channel and 200 in the B channel.

6.5.5 Time Slewing

While certain to exist, the issue of time slewing has not been well addressed. For the present work, with the additional constraints provided by MIA timing, time slewing is not a major issue. It is however important in monocular fitting.

6.6 Atmospheric Monitoring

Understanding the atmosphere is a difficult challenge. Clouds, temperature and pressure profiles, and the distribution of aerosols all affect light production and transmission. Fortunately, the relative proximity of the HIRES–MIA events limits the affect of the varying atmosphere as discussed in section 5.3.4. Therefore, the following discussion will primarily descriptive.

Prior to the start of 1995, HIRES relied upon an hourly weather code recorded by the operator and an array of ground based light emitters, called flashers, which fired every few minutes. The flasher events can be analyzed to understand the atmosphere. The idea is to determine how much light is scattered out of the flasher beam as a function of height. This allows determination of the density profile for aerosols. Besides cloud cover, the changing distribution of aerosols accounts for the greatest atmospheric variation. A major drawback is that the flasher observations are limited to a few select directions originating from a few points on the ground and therefore they only sample a small part of the sky.

Early in 1995, a LIDAR system was installed at the center of the CASA site. It consisted of a nitrogen laser beam which is directed upward to a rotating device which can send the beam in any skyward direction. The usual lidar scan pattern is eight equispaced azimuthal directions at 0, 30, 45, and 60 degrees away from vertical. The LIDAR system allows the entire atmosphere to be mapped out. Unlike the flashers, there is very little intrinsic beam spreading.

Basic meteorological data is also recorded and available from other sources. A weather station which records temperature, wind velocity, and direction, was installed at hires2 around January 1995. Considerable data is also available from the Dugway meteorological department.

6.6.1 Weather Code

The standard weather code, recorded by operators once an hour, consists of five digits. These are explained in table 6.1.

Table 6.1:

HIRES Weather Codes	
1st digit	Frost 0 = No frost on tubes 1 = frost on tubes
2nd digit	Atmospheric clarity 0 = negligible scattering 1 = moderate scattering 2 = heavy scattering 3 = socked in
3rd digit	Overhead Clouds in FOV 0 = no clouds visible 1 = < 1/2 sky cloudy 2 = > 1/2 sky cloudy
4th digit	Horizon cloudiness 0 = no clouds visible 1 = clouds visible
5th digit	Overhead cloudiness (all sky) 0 = no clouds visible 1 = < 1/4 sky cloudy 2 = 1/4 - 1/2 sky cloudy 3 = 1/2 - 3/4 sky cloudy 4 = > 3/4 sky cloudy

6.6.2 Flashers

The flashers are remote field devices which emit a flash of light at almost regular intervals. They are battery powered and recharge during the day by solar panels. There is a heating element across the face to melt snow during the winter. Recent flashers can be remotely controlled by radio using touch tone phone codes.

There is a flasher at each corner of the CASA-MIA ground array. These are aimed vertically. Furthermore, there is an "intersite" flasher, aimed at a shallow angle, which is visible from both hires1 and hires2. There is also an array of flasher consisting of two legs going out 10 km, which is only in the hires2 field of view.

6.6.3 Atmospheric Characterization

The atmospheric characteristics affect the generation and transmission of all light seen by the HIRES detector. The rate of direct scintillation production is a function of temperature and pressure. This dependence is rather mild for both parameters [44, 25, 19]. Cherenkov production also depends on the atmospheric density, since the energy threshold depends on density. Rayleigh scattering is affected only by the density of scattering sites.

The aerosol scattering is complicated. It is a strong function of atmospheric specifics. The aerosols come from dust kicked up off the desert floor. For some nights the aerosol scattering is almost nonexistent, but for other nights it contributes heavily to the light seen at the detector for many events. To a good approximation the aerosol density profile can be treated as an exponential falloff, parameterized by a ground density and a scale height, where these parameters vary as a function of time.

At present, the HIRES group has analyzed the intersite flasher for 179 run nights and broadly characterized them as belonging to one of the following categories:

- molecular: negligible aerosol scattering
- intermediate: worse than "molecular", but better than "standard"
- standard: aerosol concentration assumed in the USGS standard desert model
- worse than standard: as named

The percentage of run nights occupying these categories is 9%, 56%, 22%, and 13% respectively. Clearly the median night is better than the USGS standard desert model. The nights

falling under the "worse than standard" category range from bad to awful and are strong candidates for rejection.

Chapter 7

Trajectory Reconstruction

7.1 Introduction

Before considering the issue of reconstruction errors and biases for the shower observables, $X_{\max}$, Energy, and N_μ , it is important to examine trajectory reconstruction. HIRES determines the Energy and $X_{\max}$. MIA determines N_μ . Both of these measurements require finding the trajectory, which is a joint HIRES–MIA effort. Trajectory reconstruction errors and biases will contribute to the errors and biases of the shower observables.

Trajectory reconstruction involves finding the SD-plane (see Fig. 7.1) and subsequently finding R_p and Ψ within the SD-plane. This process may be iterated to refine the result. The errors and biases arising from this process are most naturally expressed in the (plane normal, R_p, Ψ) parameterization of the trajectory. Because the mirror locations vary, it is strictly proper to speak of the SD-plane formed with each mirrors. This results in a slightly different trajectory parameterization for each mirror. Since this is cumbersome, in practice it is best to use a single (plane normal, R_p, Ψ) parameterization involving the SD-plane formed with centroid of the mirror locations. This does not significantly affect any of the arguments below.

Plane fitting is affected only by HIRES. The following affect the plane normal error:

- Finite tube aperture
- More than one triggered mirror

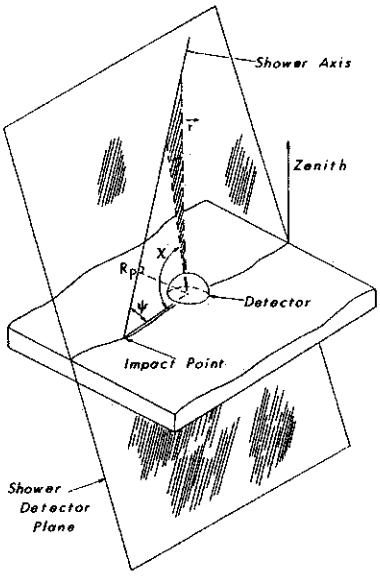

Figure 7.1: Shower reconstruction geometry

- Noise tubes
- Tube signal fluctuations near threshold

Of these, the finite tube aperture has the dominant impact.

R_p and Ψ are found together using timing data from HIRES and MIA. The following affect the R_p and Ψ errors:

- Tube trigger time slewing
- Mirror aberrations
- Fluctuations in muon arrival times
- Tube trigger time discreteness
- Muon counter time discreteness

For both detectors, the timing discreteness is dominated by the other effects.

7.2 Plane Fitting

The pattern of the triggered HIRES tubes is the primary determination of the shower detector plane. Tube amplitudes help refine the SD-plane.

The finite 1-degree tube aperture limits how accurately a track can be located within a tube. The most conservative approach is to assume it is only known whether a track triggered a tube; in other words tube amplitude information is ignored. Let p be the offplane angle, the distance between the tube center and the track. Assume that a tube triggers if $p < 0.5$ degrees. Assuming any p value in the range $[-0.5°, 0.5°]$ is equally likely, the mean square deviation is given by $\sigma^2 = \int_{-0.5}^{0.5} p^2 dp / \int_{-0.5}^{0.5} dp = 1/12 \Longrightarrow \sigma = 0.29°$. When tube amplitude information is used, σ is effectively reduced.

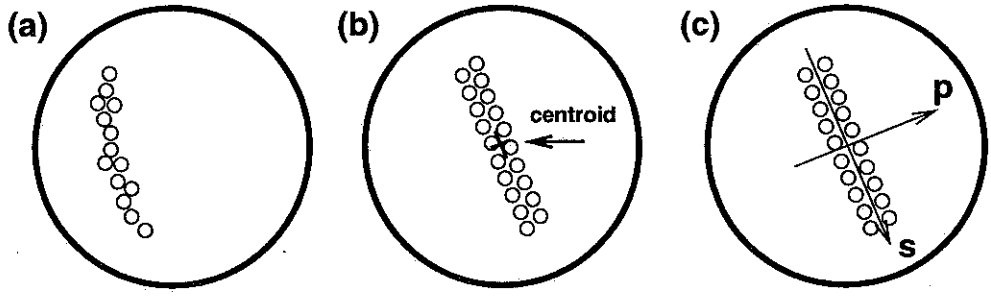

Figure 7.2: View of track on unit sphere

In a slightly simplified picture, plane fitting is essentially a line fit to a collection of points defined by the centers of the triggered tubes. Ignoring parallax, we can approximate the HIRES site as a point. If we define the directions seen by the tubes from HIRES by points on a unit sphere, the SD-plane passes through the center of the sphere and intersects the unit sphere on a great circle (see Fig. 7.2-a). The unit vectors representing directions of triggered PMTs are distributed near this great circle along an arc whose length is the angular range over which the shower is observed. For most projections of this track onto a plane, the projected arc is curved. However, there is a plane, whose normal is perpendicular to the centroid of the unit vectors of the triggered tubes. In this plane the projected arc is almost exactly straight (Fig. 7.2-b). This allows one to define projected coordinates s and p for the

pmt unit vectors. The coordinate s is defined as the path length along the projected arc, with $s = 0$ at the centroid. The coordinate p is defined perpendicular to s (see Fig. 7.2-c).

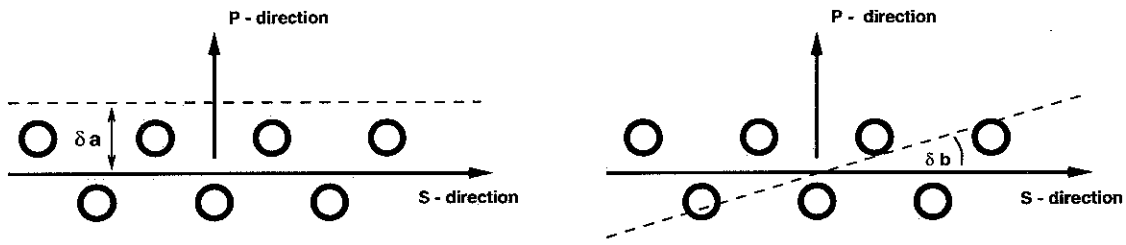

Figure 7.3: Illustration of plane fitting errors, δa and δb

Clearly, the s and p coordinates can not be determined perfectly without perfect knowledge of the track direction. In practice the track centroid is determined and the s direction is chosen to lie quite close to the projected track direction. At this point the SD-plane can be improved by making a linear fit, $p = a + bs$, where the parameters a and b are nearly zero. Conceptually a represents a shift in the trajectory and b represents rotation around the centroid (see Fig. 7.3). The plane fitting geometry errors are the errors, δa and δb, arising from the linear fit. In most cases the density of tubes along the track is nearly constant, therefore it is useful to introduce the parameter $\rho = N/L$ where N is the number of tubes in the the track and L is the length in degrees. Linear regression for the N measurements gives:

$$\sigma_b^2 = \frac{\sigma^2}{\sum s_i^2 - \frac{1}{N}(\sum s_i)^2} \tag{7.1}$$

The denominator can be carried over to the continuous limit. The second term will be nearly zero since there is an approximately equal density of tubes on either side of $s = 0$. The first term becomes:

$$\sum x_i^2 \Longrightarrow \int_{-L/2}^{L/2} \rho\, x^2\, ds = \rho L^3/12 \tag{7.2}$$

Therefore:

$$\sigma_b \text{ (radians)} \doteq \sqrt{12/\rho}\ (\sigma/L^{3/2}) \tag{7.3}$$

where σ is given above. This formula says that both track length and width improves the plane fitting accuracy with length making the greater contribution.

A shift by σ_a in a is very nearly equal to an equivalent shift of $\langle p \rangle$, as is evident from the relation $p = a + bs$ and the fact that $s = 0$ is near the center of the track. Therefore, we get:

$$\sigma_a \text{ (radians)} = \sigma/\sqrt{N} = \sigma/\sqrt{\rho L} \tag{7.4}$$

The SD-plane normal is approximately along the p axis shown in Fig. 7.2-c. A shift of a by σ_a produces a shift of the normal vector by σ_a in the $\vec{s} \times \vec{p}$ direction. A small shift σ_b moves the normal vector σ_b in the $-\vec{s}$ direction.

For a typical HIRES–MIA coincident track, 30° long with a density of 1 tube per degree, the result is $\sigma_b = 0.0061$ radians $= 0.35°$ and $\sigma_b = 0.0012$ radians $= 0.05°$. The actual result will be smaller because of the tube amplitude information.

7.2.1 Lesser effects

Three additional effects play a role in SD-plane determination. First, most events contain noise tubes. Based on a 200 Hz singles rate, the 35 μS holdoff time for triggered mirrors, and 256 tubes/mirror, the expected noise rate is 1.8/mirror. The plane fitting algorithm uses crude and conservative timing considerations to reject almost all noise tubes. At 3 km, an event requires $\approx 3\mu$S to cross a mirror. Even simply requiring noise tubes to be an entire mirror "away" from an expected location based on timing, reduces the number of noise tubes by a factor of ten.

In addition to the noise tubes, many HIRES–MIA events have tubes which are not far from the HIRES trigger threshold. This means some tube signals will fluctuate below the trigger level. This would throw off a plane fitter based solely on the triggered tubes. In practice the use of tube amplitude information insures that tubes near threshold do not

contribute strongly to the plane fit result. Since noise tubes are also typically near threshold, the few which get through have a minimal impact on the plane fit.

A final effect arises from parallax between the individual mirrors. Accounting for parallax requires knowing the distance of the shower from detector; in other words, it requires adjusting a shower trajectory rather than the SD-plane normal. In fact this is done in both the **hbrd_traj.run** and **gpln** programs. The parallax does provide some improvement. This can be more precisely stated. Consider an arbitrary point associated with the detector, say the centroid of all the mirror locations. The σ_a and σ_b for the SD-plane formed by the final trajectory and the detector centroid will be less than that formed by the original plane fit as described above.

7.3 Monocular Time Fitting for R_p and Ψ

Within the SD-plane there are two unknown parameters, R_p and Ψ. R_p is the distance of closest approach and Ψ is the angle between the trajectory and the ground (see Fig. 7.1). These are determined from HIRES tube and MIA counter timing information.

In principle both R_p and Ψ can be determined from the HIRES timing alone. This is called monocular time fitting. It is useful to examine monocular time fitting first in order to acquire a better understanding of what is gained from the MIA timing information. Monocular time fitting amounts to finding the least squares fit for R_p, Ψ, and an arbitrary time offset, t_0, given the tube triggering times, t_i and their directions within the shower SD-plane, χ_i. Mathematically, the fit is:

$$
\begin{aligned}
(t_i)_{\text{expected}} &= t_0 + \left(\frac{R_p}{c}\right) \tan\left(\frac{\pi - \Psi - \chi_i}{2}\right) \qquad (7.5)\\
\chi_i &= \text{direction of } i\text{'th tube (see figure 7.1)}\\
c &= \text{speed of light}
\end{aligned}
$$

Figure 7.4 shows the monocular timing fit for a typical HIRES–MIA event. Unfortunately, the R_p and Ψ errors are highly correlated. One way to see why this should be true is to realize that tan() is nearly linear for a small changes in angle. This effectively reduces equation 7.5 to a linear fit with three unknown parameters. Therefore, monocular time fitting relies on the curvature of the time fit data. Typical HIRES tracks are not long enough to show much curvature.

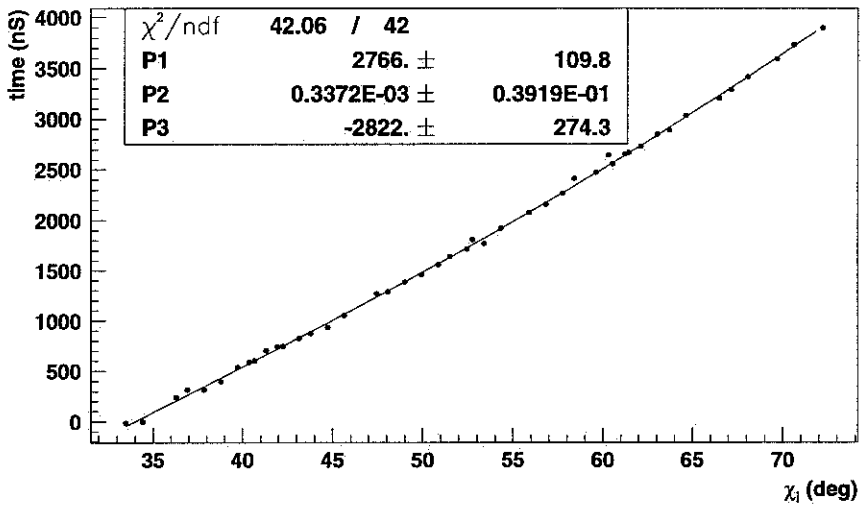

Figure 7.4: Monocular timing fit for a typical HIRES–MIA event (39° long, 45 tubes). The fitted parameters are R_p (meters), $\Delta\Psi$ (deg), and t_0 (nS). $\Delta\Psi$ is fitted rather than the first guess Ψ in order to overcome roundoff difficulties in computing the error matrix. The error on $\Delta\Psi$ is the same as the error on Ψ.

The highly correlated errors lead to much larger errors than would be the case individually if either R_p or Ψ was known independently. It is possible to derive a functional form for the track length dependence of σ_{R_p} and σ_Ψ for monocular fitting. Begin with the least squares sum:

$$\chi^2 = \sum \left(\frac{t_i - t_0 - \frac{R_p}{c} \tan\left(\frac{\pi - \Psi - \chi_i}{2}\right)}{\sigma_i} \right)^2 \tag{7.6}$$

For simplicity let $\sigma_i = \sigma_{\text{timing}}$ be the same for all tubes. Then the inverse of the covariance matrix becomes:

$$H = \frac{1}{\sigma_{\text{timing}}} \frac{R_p}{c} \begin{pmatrix} \frac{1}{R_p c} \sum \tan^2 W & \frac{-1}{2c} \sum \sec^2 W \tan W & \frac{1}{R_p} \sum \tan W \\ \frac{-1}{2c} \sum \sec^2 W \tan W & \frac{R_p}{4c} \sum \sec^4 W & \frac{-1}{2} \sum \sec^2 W \\ \frac{1}{R_p} \sum \tan W & \frac{-1}{2} \sum \sec^2 W & \frac{c}{R_p} N \end{pmatrix} \tag{7.7}$$

where $$W = \left(\frac{\pi - \Psi - \chi_i}{2}\right) \tag{7.8}$$

and $$N = \text{number of phototubes} \tag{7.9}$$

To achieve this form two negligible terms of the form $(t_i - t_0 - \frac{R_p}{c} \tan W)$ are dropped from the $\partial^2\chi^2/\partial\Psi^2$ and $\partial^2\chi^2/\partial\Psi\partial R_p$ matrix elements. In both case, these terms are dominated by a factor of at least $\sim R_p/(\sigma_{\text{timing}}\, c\, \sqrt{N}) \sim 1000$.

For the rest of the calculation, it is more convenient to express the χ_i as $\theta_i = \pi/2 - \Psi - \chi_i$. In this representation, $\theta_i = 0$ corresponds to the direction of closest impact (see Figure 7.5).

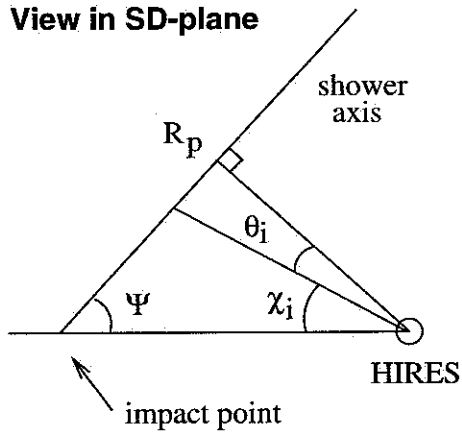

Figure 7.5: θ_i definition

W becomes $(\pi/4 + \theta_i/4)$. This make the Taylor expansion around $\pi/4$ simple.

In order to get a representative answer, consider a track with N tubes and a uniform tube density (tubes/radian), ρ, spanning the distance θ_A to θ_B (radian). Then each matrix element can be carried over to an integral of a Taylor series; for example:

$$\sum \tan W \Longrightarrow \int_{\theta_A}^{\theta_B} \rho \tan\left(\frac{\pi}{4}+\frac{\theta}{2}\right)\, d\theta \approx \int_{\theta_A}^{\theta_B} \rho\left(1+\theta+\frac{1}{2}\theta^2+\frac{1}{3}\theta^3+\frac{5}{24}\theta^4\ldots\right)\, d\theta \quad (7.10)$$

To lowest order in $(\theta_B - \theta_A)$:

$$\det H = \left(\frac{R_p}{\sigma_{\text{timing}}\, c}\right)^3 \frac{1}{4R_p c}\, \frac{1}{2160}\, N\, (\theta_B - \theta_A)^6 \quad (7.11)$$

Upon completing the inversion of H to determine the covariance matrix, one obtains:

$$\sigma_{R_p} = \frac{12\sqrt{5}\,(\sigma_{\text{timing}}\, c)}{\sqrt{N}\, L^2} = \frac{12\sqrt{5}\,(\sigma_{\text{timing}}\, c)}{\rho^{1/2}\, L^{5/2}} \quad (7.12)$$

$$\sigma_{\Psi} = \left(\frac{\sigma_{\text{timing}}\, c}{R_p}\right)\frac{12\sqrt{5}}{\sqrt{N}L^2} = \left(\frac{\sigma_{\text{timing}}\, c}{R_p}\right)\frac{12\sqrt{5}}{\rho^{1/2}L^{5/2}} \quad (7.13)$$

$$\text{where } L = \theta_B - \theta_A = \text{track length} \quad (7.14)$$

L is radians and ρ is in tubes/radian. For the typical event shown in Figure 7.4 and $\sigma_{\text{timing}} \sim$ 40 nS, these formulas yield $\sigma_{R_p} = 104$ meters, and $\sigma_{\Psi} = 3.7 \times 10^{-2}$ radians $= 2.1°$. This is in good agreement with the errors found by the minimization package.

So far nothing has been said about how σ_{timing} is determined. The 5 nS tube time resolution suggests $\sigma_{\text{timing}} \sim$ 2 nS. The 25 nS mirror–mirror time resolution via the 40 Mhz scaler appears to suggest $\sigma_{\text{timing}} \sim$ 12 nS. However, mirror–mirror time differences are clearly a systematic effect. An $M+2$ parameter fit for R_p, Ψ, and the slightly differing t_0 for each of M mirrors, loses only 1 degree of freedom per additional mirror, while leaving $\sigma_{\text{timing}} \sim$ 2 nS.

In actuality, time slewing is the dominant contribution to σ_{timing}. Arguably time slewing has both a random and systematic component. If enough events were studied, the time delay before crossing threshold could be modeled as a function of signal strength and the exact nature of the light spot crossing the tube. Photoelectron statistics would still lead to a random component. Perhaps such a study could push σ_{timing} to as low as 10 nS. In practice

this is quite difficult. It requires very precise knowledge of the tube pointing directions, mirror aberrations, and 2-dimensional tube response function. Tube directions may vary as much as $1/20^{\circ}$ due to the way they are held in the cluster. The response function varies from tube to tube. The effect of mirror aberrations has some dependence on the distance of the shower from the mirror. Finally, even if all these items were perfectly known, uncertainties in the plane fitting would still limit how well the expected time slewing could be determined.

Currently, very little work has been done to model the time slewing. In practice, there is enough variation in tube signals and the other items affecting time slewing along the track, that the timing fit residuals for typical events show a gaussian distribution. Figure 7.6 shows a histogram of individual tube time differences from the monocular fitted time for the HIRES–MIA dataset. This empirically yields $\sigma_{\text{timing}} \sim 40$ nS.

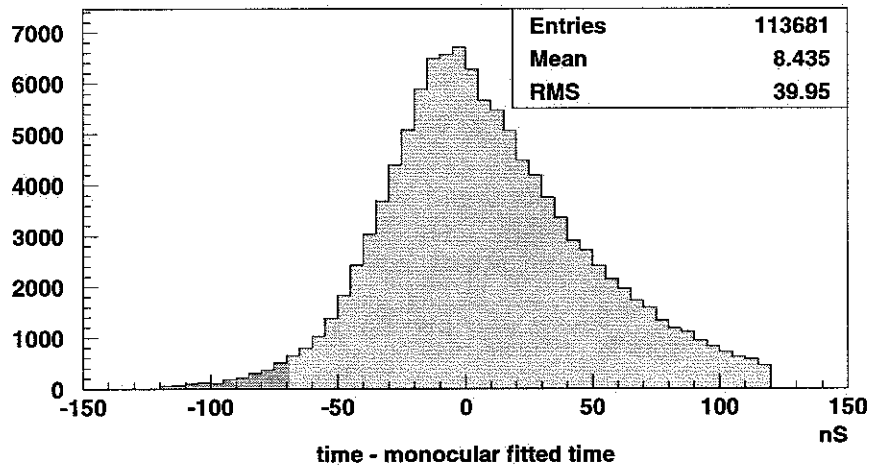

Figure 7.6: Distribution of tube timing residuals for the entire HIRES–MIA dataset using a monocular timing fit. The width of the distribution is σ_{timing}.

7.4 Hybrid Time Fitting for R_p and Ψ

The previous section demonstrated the limitations of monocular time fitting. Consider what would happen to σ_{R_p} if Ψ were known exactly. The monocular time fitting equation (7.5) would reduce to a linear least squares fit for R_p and t_0. This immediately yields:

$$\sigma^2_{R_p} = \frac{\sigma^2_{\text{timing}} c^2}{\sum x_i^2 - \frac{1}{N}(\sum x_i)^2} \tag{7.15}$$

As before part of the expression depends on the specific geometry of the track. Once again consider a track of length L and uniform tube density ρ. This quickly gives:

$$\sigma_{R_p} = \sqrt{2/N}\ \sigma_{\text{timing}}\ c \tag{7.16}$$

Given that $\sigma_{\text{timing}} \sim 40$ nS, the typical event examined during the monocular time fitting discussion would have $\sigma_{R_p} \approx 3$ meters, a thirty fold improvement.

The hybrid time fitting performed in **hbrd_traj.run** uses MIA timing information in addition to the HIRES timing information to better constrain Ψ. To roughly understand what this does, consider finding Ψ with only MIA timing information. To keep it simple, assume that the muons arrive on a plane front. Also assume the arrival time jitter is a constant value σ_{miatime}, rather than the actual nearly linear rise with perpendicular distance from the core. This leads to a linear timing fit, where the "slope" gives Ψ and the "intercept" is a timing offset. Therefore:

$$\sigma^2_{\text{slope}} = \frac{\sigma^2_{\text{miatime}}\ c^2}{\sum x_i^2 - \frac{1}{N}(\sum x_i)^2} \tag{7.17}$$

where each x_i is a perpendicular distance from the shower to the counter projected onto the SD-plane.

Roughly determining the denominator is somewhat of a hassle because the individual muon counters are grouped in patches. Also the density of muon hits is not even close to uniform over the array. This means simply assuming the event triggers a square pattern of

counters and going over to the continuous limit is not ideal. But if this approximation is made, then a shower with uniform muon density ρ covering a $L \times L$ detector area with N muon hits and inclination θ, has:

$$\sum x_i^2 \implies \int_{-L/2}^{L/2}\int_{-L/2}^{L/2} \rho\,(\cos\theta\, x')^2\, dx'dy' = \rho L^3/12 = NL/12 \tag{7.18}$$

$$\left(\sum x_i\right)^2 = \left(\int_{-L/2}^{L/2}\int_{-L/2}^{L/2} \rho\, \cos\theta\, x'\, dx'dy'\right)^2 \approx 0 \tag{7.19}$$

Here the coordinate system (x', y') is a rotated system where the x' direction is contained in the SD-plane. The result is:

$$\sigma_\Psi = \frac{\sigma_{\text{slope}}}{\sec^2\Psi} = \frac{\sigma_{\text{miatime}}\; c\; \cos\theta}{\sqrt{N/12}\; L\; \sec^2\Psi} \tag{7.20}$$

For the typical event shown in Figure 7.4, with muon hits $\sim$ 800 meters from the shower core, $\sigma_{\text{miatime}} \sim$ 60 nS. Furthermore, $N = 64$ and $L \sim$ 300 meters. This gives $\sigma_\Psi =$ .0105 radians = 0.60°. This is a clear improvement over the monocular time fitting result.

Since it is impossible to express the error for the hybrid timing fit in a simple analytic form without making the coarse approximations above, the errors for actual events are found using a bootstrap procedure. Figure 7.7 show the bootstrap results for 500 iterations of the sample event. Note that even for the hybrid reconstruction technique the correlation between R_p and Ψ remains. The width of the projections for R_p and Ψ yield their respective errors, i.e. $\sigma_{R_p} = 20$ meters and $\sigma_\Psi = 0.77$ degrees.

7.5 How MIA limits Hybrid Time Fitting

MIA limits the hybrid time fitting resolution because of arrival time fluctuations, time discreteness, and accidentals. The first reason completely dominates the effect of the other two.

Fluctuations in the muon arrival times are part of the intrinsic shower variations. Figure 7.8 shows the variation in muon arrival time as a function perpendicular detector distance

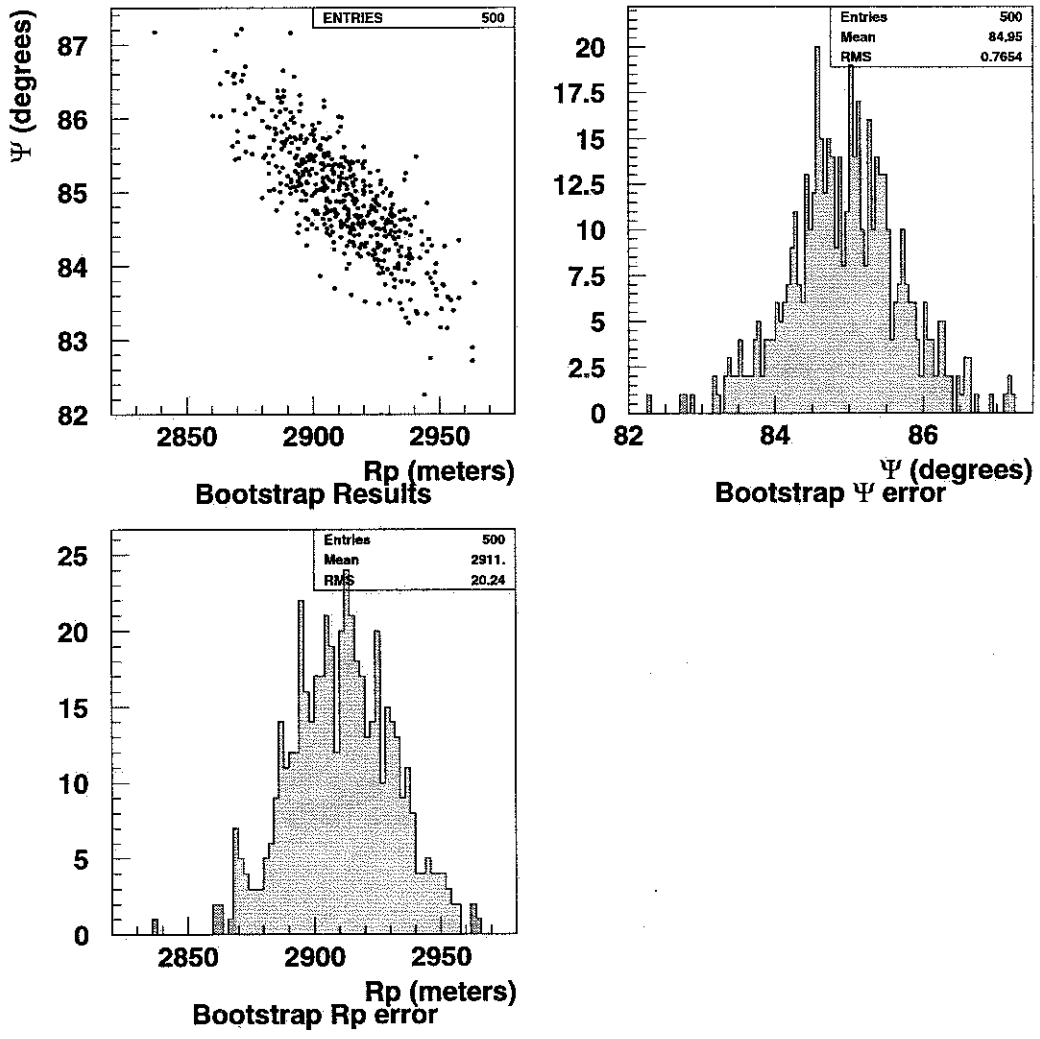

Figure 7.7: Bootstrap fitting result for a typical event. The upper left figure shows that even for hybrid fitting there is still a strong correlation between Ψ and R_p. The right and lower figures show projections for Ψ and R_p respectively. The width of these distributions give the errors on these two quantities.

from the shower core. This fit is empirically derived from the timing residuals for the HIRES–MIA dataset. The rolloff beyond 1000 meters is based on low statistics and is probably a selection bias arising from the assignment of intime muons. This rolloff is not precisely understood and therefore is the motivation for cutting out events with a significant fraction of muon counters beyond 1000 meters.

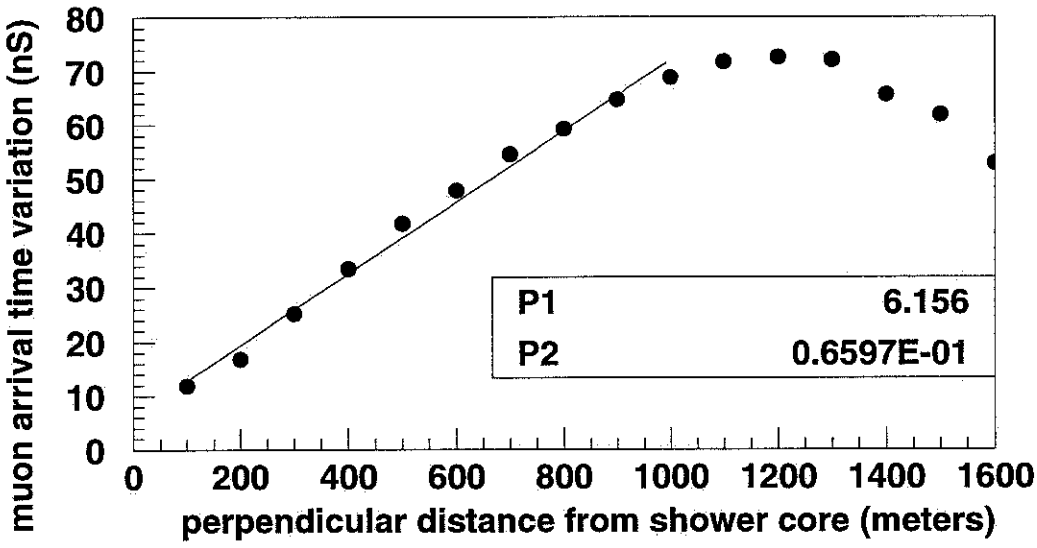

Figure 7.8: Variation in muon arrival time as a function of counter distance from the shower. This is obtained for entire HIRES–MIA dataset using the residuals to the timing fit.

Clearly the arrival time fluctuations dominate the MIA counter resolution of 4 nS at all distances.

Accidentals pose a minor problem. Given a counter pulse width of 5.2 μS, an accidental rate of $\sim$ 6 kHz, and $\sim$ 800 live counters, the expected background is about 20 counters per event. Most of these can be rejected with great confidence, but some lie close to the shower arrival front. Because the muons arrival times fluctuate from an average arrival front, it is difficult to narrow the assigned intime window to less than $\sim$ 340 nS. On average 1.4 accidentals will remain in the assigned intime window. Since the 50% of the HIRES–MIA

events have fewer than $\sim$ 110 muons, the affect of accidentals on trajectory reconstruction is not completely negligible, although it should not be have a strong impact for most of the events.

7.6 Systematic Timing Effects

Both the monocular and the hybrid time fitting methods assume that on average the tube triggers at the center with a variation given by σ_{timing} . In reality one expects on average that the tube will trigger closer to the leading edge. Limited investigations support this prediction. At worst, no track should be systematically reconstructed worse than 0.5° from its true Ψ value. The extent of this systematic shift should be greater for brighter tracks.

7.7 Core Location Error

The core location is critical for determining N_μ . Errors in the core location can be propagated from the errors on the more fundamental trajectory fitting parameters. The natural coordinate system for the core are the unit vectors parallel and perpendicular to the line of site between HIRES and the shower core. Errors in the perpendicular direction arise from plane fit errors. Errors in the parallel direction arise from errors in timing fit.

Let R_{ground} be the distance along the ground from HIRES and the core. Then:

$$\sigma_{\text{core}\,\perp} = R_{\text{ground}}\,\sqrt{\sigma_a^2 + \sigma_b^2} \tag{7.21}$$

where σ_a and σ_b are given by equations 7.3 and 7.4.

Finding $\sigma_{\text{core}\,\parallel}$, requires computing the covariance matrix element, $V_{12} = H_{12}^{-1} = \sigma_{R_p}^2/R_p$. Then propagation of errors yields:

$$\sigma_{\text{core}\,\parallel} = \left|\, \sigma_{R_p}/\cos\theta \;-\; \cot\Psi\csc\Psi \,\right| \tag{7.22}$$

where θ is the inclination of the shower.

Chapter 8

N_μ , $X_{\max}$, & Energy Reconstruction

8.1 Introduction

Consider the measurement of many showers of a fixed energy and composition. The reconstructed shower observables, $X_{\max}$, Energy, and N_μ will vary considerably. Fluctuations in the reconstructed values arise for two broad reasons: intrinsic shower fluctuations and detector limitations. The former are discussed in chapter 3. For protons these fluctuations turn out to be similar to the detector limitations, while for iron they are considerably less. A detector monte carlo is used to determine detector based statistical errors.

Systematic errors arise from several sources. The most important systematics involve the HIRES detector. These are the overall average phototube sensitivity and the fluorescence efficiency. For MIA, uncertainties in both the scintillator efficiency and the turn on threshold are systematic effects. Additional systematic effects may arise from the reconstruction techniques used. These will be explored via the detector monte carlo.

Based on the results below a complete list of cuts to be used for the final results will be presented. A list of systematics will also be presented.

8.2 Fitting for N_μ

In order to determine N_μ , we make the assumption that the normalized lateral distribution is given by the normalized AKENO lateral distribution, i.e. equation 3.7 divided by N_μ :

$$\rho_\mu(R) = (0.325/R_0^2)\, r^{-0.75}\, (1+r)^{-2.52}\, \{1 + (R/800\text{ m})^3\}^{-0.6} \tag{8.1}$$

where $r = R/R_0$ and R_0 is a characteristic length slightly dependent on shower inclination. We also assume that this function is independent of energy and composition.

In chapter 9, we compare the normalized AKENO lateral distribution with the normalized distribution from the HIRES–MIA dataset. The energy independence issue is also tested. Since the LDFs agree well, it makes sense to use the one derived from the best statistics. AKENO comes out ahead here because it has a large event set and energy resolution, the major weakness of ground arrays, is irrelevant.

Given equation 8.1, finding N_μ is a one parameter fit. This is done using a maximum log likelihood where the logarithm of the likelihood, $\mathcal{L}$, computed from both the hit and unhit counters is given by:

$$\log \mathcal{L}(N_\mu) = \sum_{hit} \log(1 - P_{unhit}) + \sum_{unhit} \log(P_{unhit}) \tag{8.2}$$

$$P_{unhit} = \exp(-E_i)\, \exp(-\text{expected background}) \tag{8.3}$$

$$E_i = N_\mu \times \rho_\mu(R_i) \times \text{Area} \times \text{Eff}_i \tag{8.4}$$

Here E_i is the expected number of muons at a counter with a perpendicular distance R_i from the shower core given the lateral distribution. Eff_i is the counter efficiency. P_{unhit} is the probability that a counter is not hit taking into account both poisson statistics for the expected number of muons and the background within the in time window.

8.3 Source of N_μ Reconstruction Errors and Biases

Almost all N_μ reconstruction errors and biases arise from MIA. Nevertheless, HIRES has a small impact because the HIRES data contributes to the shower core reconstruction which in turn affects fitting for N_μ. The following affect N_μ reconstruction in a systematic manner:

- Limited muon sampling
- Muon arrival time variation
- Accidental muon hits
- Core location error (statistical and systematic)

The muon sampling is limited both in area and resolution. The muon array was designed to cover the area seen by CASA. Together the 1024 1.3×1.9 m^2 counters cover only 1.0% of the .25 km^2 spanned by CASA. Furthermore, most HIRES–MIA event cores fall outside the CASA–MIA array so that there is no coverage near the core. Also the muon counters are binary in nature, making no distinction between one or more muons. The muon sampling directly limits how well N_μ is reconstructed.

The arrival time fluctuations are discussed in section 7.5. At large distances from the core, where the arrival time fluctuations increase, it becomes difficult to determine which muons are in time. When muons which actually belong to the shower are rejected as out of time, N_μ is systematically reconstructed low.

Just as accidentals have a minor effect on trajectory reconstruction, they also have a minor effect on N_μ reconstruction. Most accidentals fall outside the in time window, but 1.4 remain within it on average. Since this background rate is taken into account during the reconstruction, accidentals lead to a statistical rather than systematic effect.

The main muon systematic reconstuction error arises from uncertainty in the counter efficiency. Although we use the 93% mentioned in section 4.2, there is evidence that the efficiency has decreased with time. Splitting the difference between the extreme value of 93% and the 80% discussed in section 4.2 leads to a 6.5% systematic. Uncertainties in counter turn on behaviour also lead to systematics. The GEANT simulation shows that full turn on occurs over a range of only 0.12 GeV. Combining the results of table 3.1 yields a systematic of less than 2%, even if the details of the turn on region are totally misunderstood. Therefore, this systematic is always dominated by the counter efficiency systematic.

8.4 Detector Monte Carlo

A detector monte carlo was developed in order to study reconstruction and aperture issues. This monte carlo is a combination of the standard HIRES monte carlo and a detailed simulation of the comparatively simple MIA array.

The input shower physics is rather simple. The number of muons above the detector threshold at ground level is assumed to be 8×10^5 for a 10^{17} eV "iron" primary and half this amount for a "proton" primary. It is also assumed to scale as $E^{0.80}$. Although these assumptions are tuned toward the final result, the monte carlo has been run under a variety of assumptions. It turns out that for reconstruction statistical errors and biases, the variation with muon multiplicity is fairly slow. Any reasonable set of assumptions give almost the same answers. This is also true for the aperture issues, because we are concerned with relative aperture rather than absolute aperture.

The electromagnetic shower profiles are taken from a shower library which gives the number of charged particles every 20 g/cm^2. The shower libraries are generated by the Todor Stanev's KNP model based monte carlo [36] and distributed over a given energy range with a spectral index similar to that experimentally observed. All showers were generated at 45° inclination. It is straightforward to rotate a given shower into the desired trajectory. Since we are concerned with only the electromagnetic component rather than the muonic, this procedure is very nearly the same as generating a shower at the desired inclination, and it saves computation time. There are separate libraries for proton and for iron primaries.

The average muon arrival time as a function of distance is assumed to depart from a plane front arrival time by the amount:

$$T(R) = 0.0655\ R + 0.0001199\ R^2 \tag{8.5}$$

Here R is in meters and the T is in nS. This result [58] was empirically derived from the large CASA–MIA dataset and is assumed to extend beyond the $\sim$ 350 meter maximum obtainable from CASA–MIA events, whose cores lie within the array.

The muon arrival time is assumed to fluctuate about the form given above in a gaussian manner with a σ which is dependent on R:

$$\sigma_t(R) = 6.2 + 0.66\ R \tag{8.6}$$

This result is derived from the HIRES–MIA dataset as discussed in section 7.5.

For each muon counter, an expected number of muons is computed based on equation 8.1. The actual number generated is poisson distributed about the expected value, with arrival times given by the previous equations. The number of accidental muons expected for each counter is 5 kHz times the several microsecond simulation window centered on the arrival time of the shower. The number of accidentals generated is poisson distributed about this expected value, with arrival times equally distributed within the simulation window.

Simulating the MIA trigger is easy. Each muon hit is treated as a current pulse which rises at the hit time and falls 5200 nS later. Then these pulse edges are time sorted taking into account the known cable length delays. Each pulse edge is examined in temporal order. Patch level pulses are simulated when the 3 counter/patch requirement is met. When a rising pulse edge is encountered for a counter which is still high, the pulse is deleted since this muon could not have triggered a muon counter. When the counter level time scan is finished, each patch level trigger is treated as a current pulse which rises at the trigger time and falls 2500 nS later. The patch level triggers are then time sorted. An array trigger is declared if and when the patch level current sum reaches six patches. A common stop delay of 2000 nS is added to this trigger time to give the common stop time. This simulates the trigger holdoff. Every counter which has a high pulse at the common stop time is marked as triggered and the trigger time is the leading edge of the pulse. These times are then discretized to 4 nS to simulate the finite timing resolution of the MIA counters.

The MIA information is packed into a standard MUON bank. Also the beginning of a monte carlo output file contains one MDED bank, specifying the dead counters. This is taken from an actual data file midway through the dataset. This is representative because the real muon counters die at a fairly constant rate over the HIRES–MIA dataset, starting with 59 dead and ending at 175 dead. Patches 2 and 4, which have a known cross talk problem, are simulated as though there was no problem. The muon information from these patches is discarded in **hbrd_traj.run**, just as it is for the actual data.

HIRES phototube simulation begins with the profile from the shower library. Given this profile, the light production and atmosphere are modeled in the same manner as the profile reconstruction program, **pfl**, as described in section 5.3.4. In order to model the affects of mirror aberration and time slewing, the light production is divided into 0.04 degree angular bins along the shower track. A raytracing table is used to divide the light from each bin amongst the appropriate tubes. This yields an electronic signal profile as a function of time for each tube.

The electronic signal profiles for each tube are now modified by adding sky noise fluctuations to each time bin. These profiles are sent through an RC filter routine to simulate the RC filtering on the OMBs. The resulting profiles are checked to see if the signal has crossed the monte carlo set threshold, typically 800 mV. If so, the tube is tagged as triggered and the threshold crossing time is recorded. Unlike the actual detector, where tube thresholds vary continuously during normal operation, the monte carlo thresholds are held fixed.

Noise tubes are not included in the events. This is not important because in the real data almost all noise tubes are easily removed before final reconstruction begins with **hbrd_traj.run**. See section 7.2.1 for details.

The resulting pattern of tubes is checked to see if the mirror triggers based on the standard subcluster and mirror trigger requirements. The triggered tube information is stored in a RAW1 bank. A default calibration is applied to produce a corresponding PHO1 bank. An MCPR bank stores the monte carlo trajectory, energy, shower profile, and other generation

parameters for comparison with the reconstructed values. PLN1 banks are added later using a DST version of the plane fitter.

The resulting DST file is then processed using the standard analysis programs described in section 5.3.

8.5 Monte Carlo results for N_μ biases and errors

Figure 8.1 shows the distribution of core locations for monte carlo generated events which triggered HIRES and MIA and passed successfully through the reconstruction programs. This includes the important 15° track length cuts and the 40 in time muon cuts. "Proton" and "iron" primaries are shown for three different energy ranges. Events were generated to lie within a $4 \times 4\,\mathrm{km}^2$ region centered on MIA uniformly distributed in solid angle stopping at inclination of 60°. The growth in aperture as a function of energy is apparent. Table 8.1 lists the aperture numerically, 1-3 $\times 10^{17}$ eV has been normalized to one for protons.

Table 8.1:

HIRES–MIA relative aperture			
	1–3 $\times 10^{17}$	3–10 $\times 10^{17}$	1–3 $\times 10^{18}$
"proton"	1.00	1.55	2.36
"iron"	1.36	1.95	2.90

Figure 8.2 shows the difference between reconstructed and input N_μ where only the limited detector area is considered. No accidentals are generated and equation 8.5 is used without timing jitter. The events are reconstructed assuming no accidentals, i.e. the second term is dropped from equation 8.3. Furthermore, the actual trajectory is used for both the direction and core in order to compute the R_i distances to each counters. The basic sampling limitation is an 11% effect. This is nearly independent of energy because at higher energies more events are seen further from MIA.

Tables 8.3 and 8.4 summarize the statistical error and bias of reconstructed N_μ in percentage for several cases. Sampling effects are included in all cases. "acc", "tjit", "traj", refer respectively to adding the impact of accidental muons, muon arrival time variation, and using the reconstructed shower core rather than the monte carlo shower. The last line in each table represents the sum of all effects.

These results are sensible. The addition of accidentals without fluctuating the muon arrival times has almost no impact because it is easy to isolate the accidentals. Fluctuating the muons arrival times contributes about 6% to the statistical error. It also causes a systematic downward bias because some shower muons fall outside the timing window. Once the muon arrival times are fluctuated, it is more difficult to isolate the accidentals which then contribute about 1% to the statistical error and substantially effect the downward bias. The trajectory reconstruction errors add another 12% or so to the statistical error.

In general the N_μ shift distributions which give the numbers in tables 8.3 and 8.4 are quite gaussian. However two systematic effects are notable. Figure 8.3 shows the N_μ reconstruction bias as a function of the number of hit counters. As expected the statistical error declines as the number of counters increases. Because two patches are rejected during reconstruction because of a crosstalk problem and the because the monte carlo simulates a realistic number of dead counters, full saturation in these plots occurs at 814 hit counters. About 100–200 counters from saturation a strong systematic downward bias kicks in. This effect arises when the muon arrival times are fluctuated. These plots are the basis for the 700 counter saturation cut made during the data analysis presented in chapter 9. This cut tends to eliminate events near the center of MIA.

The second systematic effect is shown in figure 8.4. In this set of simulations, the muon arrival times are fluctuated but no true accidentals are generated. The plots show what fraction of the shower muons are rejected as accidentals as a function of the distance along the ground between the shower core and the center of MIA. Rejecting shower muons systematically biases the N_μ reconstruction downward. Clearly the problem quickly becomes severe

after 1000 meters. Furthermore, figure 7.8 indicates that muon arrival time fluctuations are probably not understood for counters more than 1000 meters from the shower trajectory. Due to these effects, a 1000 meter distance cut is made.

Tables 8.5 and 8.6 are analogous to tables 8.3 and 8.4 following the application of the two cuts discussed above. The final statistical N_μ error, with all effects included, is reduced from about 30% to 20%. Figure 8.5 shows the resulting differences between the reconstructed and generated N_μ .

Naturally these cuts change the aperture. Table 8.2 shows the new values with 1-3 $\times 10^{17}$ eV normalized to one.

Table 8.2:

HIRES–MIA relative aperture			
	1–3 $\times$ 10^{17}	3–10 $\times$ 10^{17}	1–3 $\times$ 10^{18}
"proton"	1.00	0.95	0.78
"iron"	1.00	0.65	0.57

Table 8.3:

Statistical N_μ reconstruction error (%)						
Monte Carlo conditions	1–3 $\times$ 10^{17}		3–10 $\times$ 10^{17}		1–3 $\times$ 10^{18}	
	p	Fe	p	Fe	p	Fe
none	10.6	9.8	10.1	10.2	10.0	9.4
acc	10.6	10.5	10.4	11.4	11.1	12.0
tjit	16.9	19.2	17.1	20.9	18.2	19.2
traj	17.7	14.4	17.2	15.8	18.7	15.9
acc + tjit	17.5	17.8	17.8	20.0	18.8	18.3
acc + traj	22.2	19.2	21.7	20.3	25.1	24.4
tjit + traj	23.2	22.7	23.4	23.3	24.1	22.8
acc + tjit + traj	28.7	29.4	30.8	29.0	32.3	29.5

Table 8.4:

N_μ reconstruction bias (%)						
Monte Carlo conditions	$1–3 \times 10^{17}$		$3–10 \times 10^{17}$		$1–3 \times 10^{18}$	
	p	Fe	p	Fe	p	Fe
none	-1.3	-1.7	-1.3	-2.5	-2.0	-2.5
acc	-1.9	-0.4	-3.7	-6.4	-7.2	-10.1
tjit	-7.0	-7.5	-6.8	-7.6	-7.8	-8.4
traj	-2.0	-2.0	-4.1	-4.8	-5.0	-5.7
acc + tjit	-9.7	-11.0	-11.7	-14.8	-14.8	-17.5
acc + traj	-0.3	-1.4	-2.2	-5.0	-6.9	-10.1
tjit + traj	-7.5	-7.5	-9.3	-9.6	-10.7	-11.3
acc + tjit + traj	-6.0	-8.3	-10.8	-13.6	-14.2	-16.8

Table 8.5:

Statistical N_μ reconstruction error (%) (with cuts)						
Monte Carlo conditions	$1–3 \times 10^{17}$		$3–10 \times 10^{17}$		$1–3 \times 10^{18}$	
	p	Fe	p	Fe	p	Fe
none	10.2	8.0	7.7	5.9	5.3	5.1
acc	10.2	8.1	7.9	6.1	5.5	5.4
tjit	14.3	8.8	9.1	6.4	6.9	5.9
traj	17.4	13.3	17.3	14.5	16.3	14.3
acc + tjit	15.0	9.4	9.4	6.4	6.1	5.8
acc + traj	21.7	15.1	19.2	16.0	16.2	13.7
tjit + traj	21.2	14.6	17.8	15.0	18.2	16.4
acc + tjit + traj	24.2	18.4	20.7	16.7	17.0	14.9

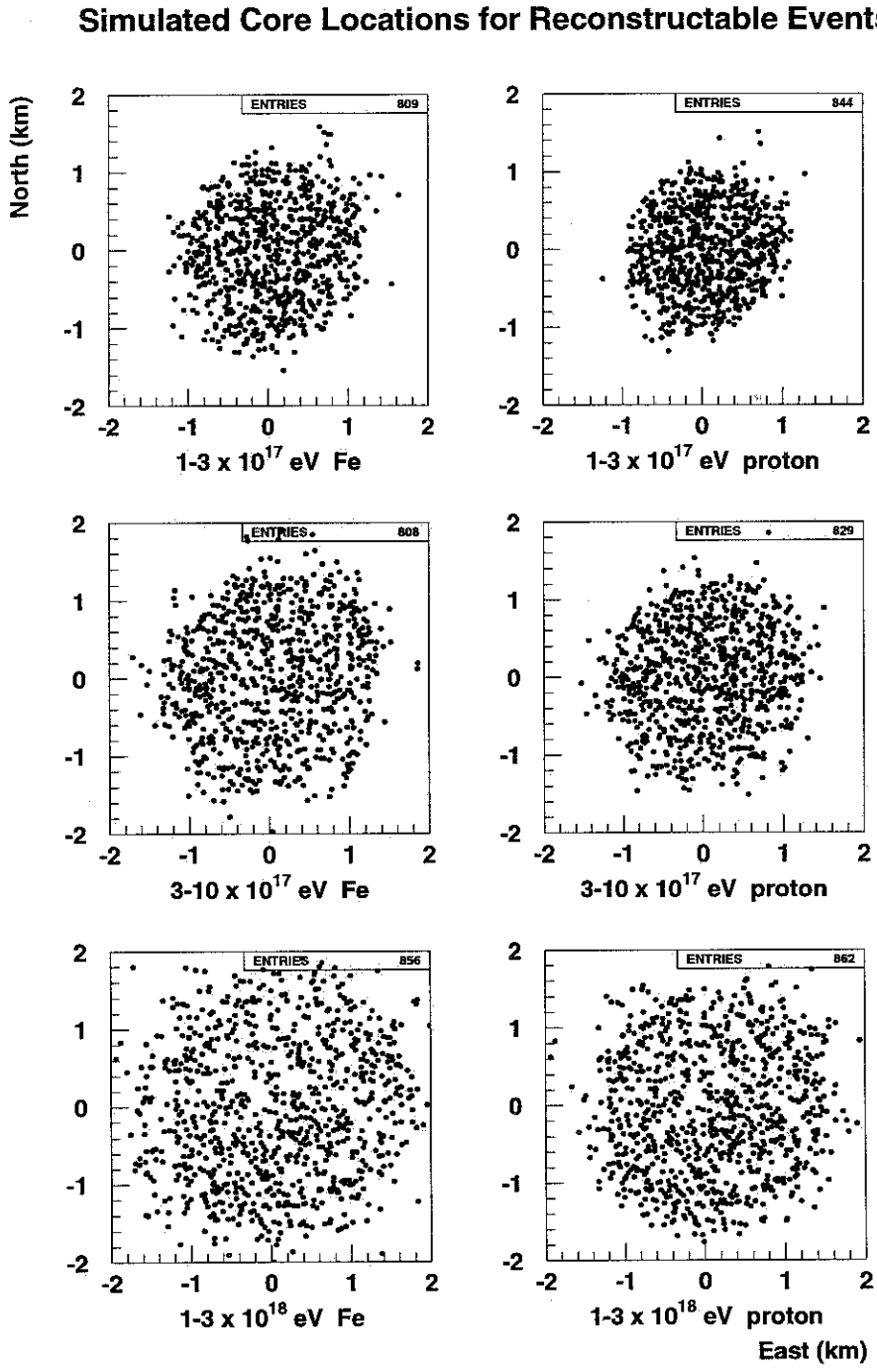

Figure 8.1: Monte Carlo core locations of generated events.

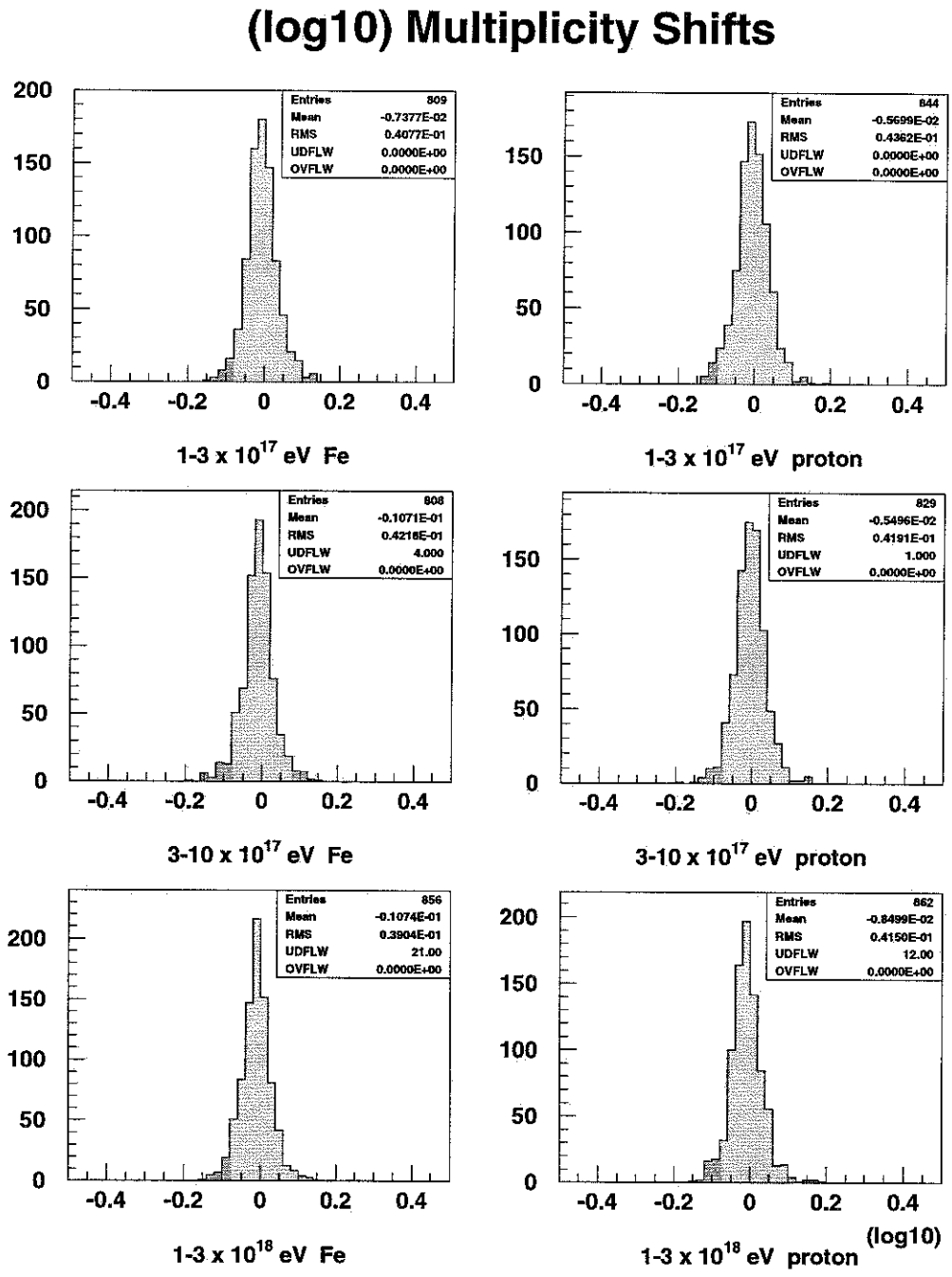

Figure 8.2: Difference between reconstructed and input $\log N_\mu$ for monte carlo simulated events. These plots show only the effect of the limited MIA detector coverage. The effects of accidentals, arrival time jitter, and trajectory reconstruction error are not included.

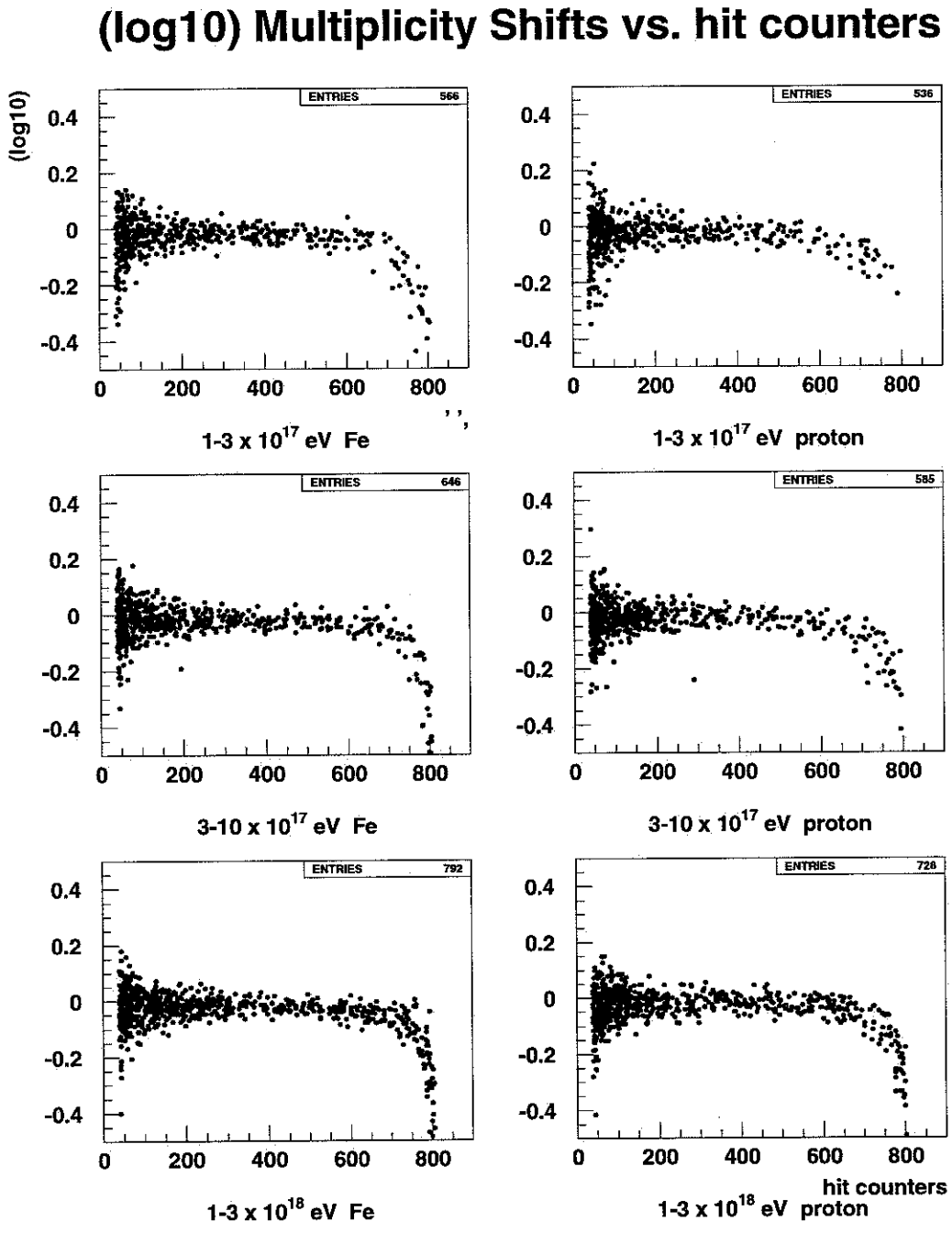

Figure 8.3: Systematic N_μ reconstruction bias near detector saturation. In this simulation the muon arrival times are fluctuated, but no accidentals are generated and the monte trajectory is used during reconstruction.

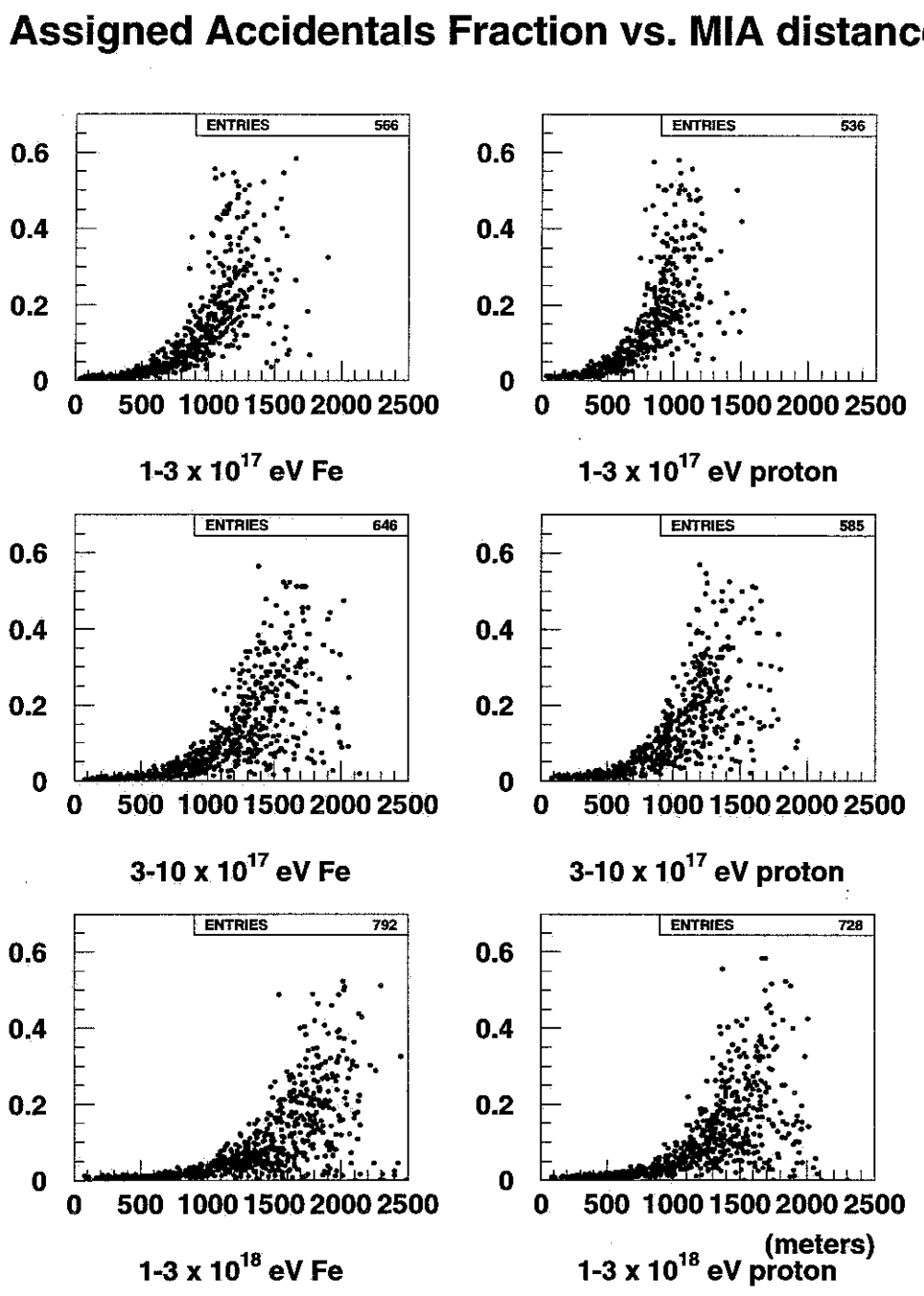

Figure 8.4: Fraction of hit counters determined to be accidentals as a function of shower core distance from the center of MIA. In this simulation the muon arrival times are fluctuated, but no true accidentals are generated. Beyond 1000 meters the rejection of shower muons quickly becomes severe.

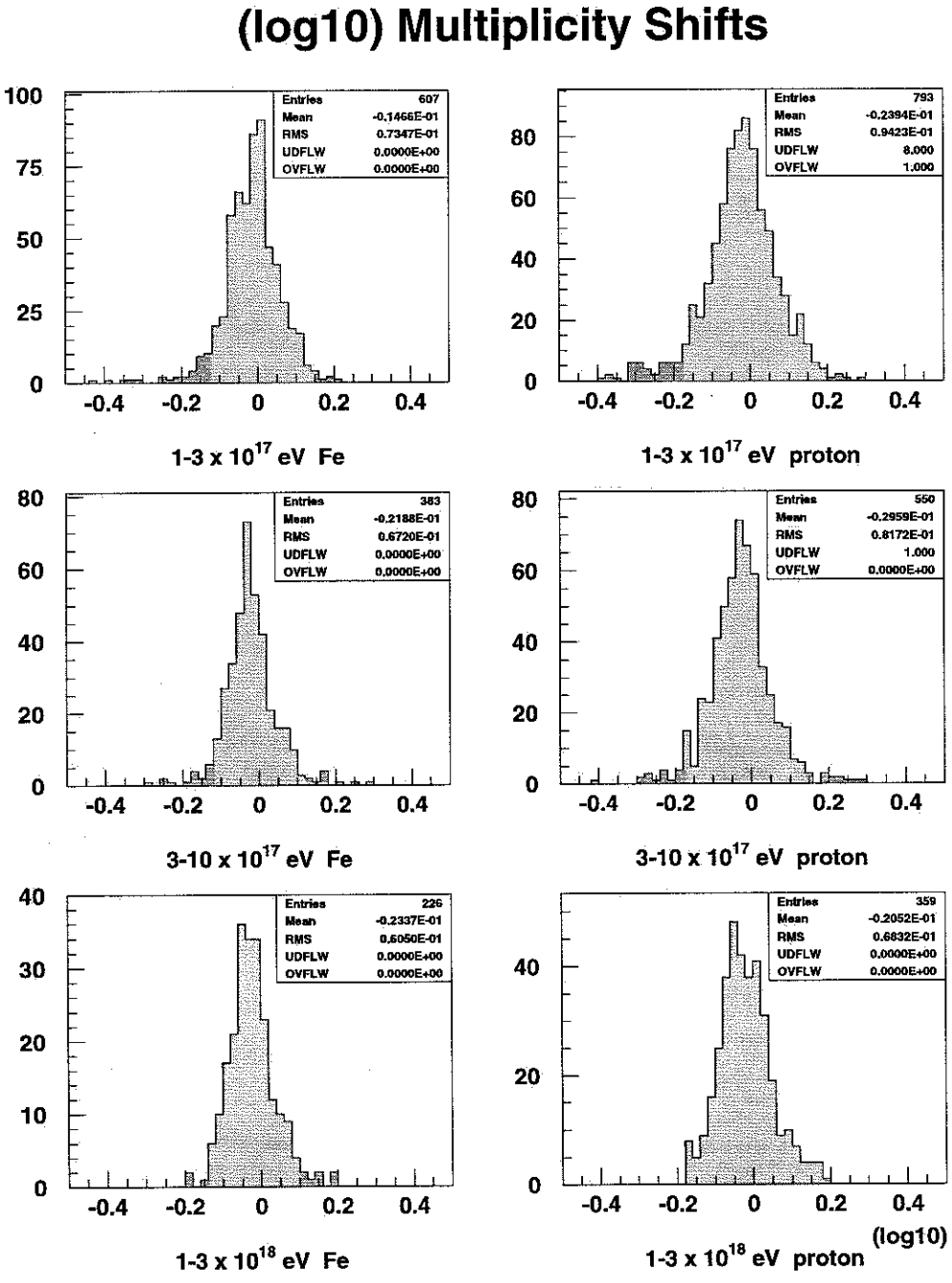

Figure 8.5: Difference between reconstructed and input $\log N_\mu$ for monte carlo simulated events with saturation and distance cuts applied. The effects of accidentals, arrival time jitter, and trajectory reconstruction error are included.

Table 8.6:

N_μ reconstruction bias (%) (with cuts)						
Monte Carlo conditions	1–3 $\times 10^{17}$		3–10 $\times 10^{17}$		1–3 $\times 10^{18}$	
	p	Fe	p	Fe	p	Fe
none	-1.7	-1.9	-2.2	-2.3	-2.5	-4.8
acc	-2.2	-3.2	-3.4	-3.5	-3.8	-4.5
tjit	-7.1	-5.1	-5.5	-6.2	-5.7	-7.9
traj	-2.5	-1.9	-4.9	-4.2	-5.3	-5.5
acc + tjit	-8.9	-6.6	-7.2	-8.0	-7.2	-9.6
acc + traj	-0.5	-0.5	-1.8	-0.0	-0.5	-1.5
tjit + traj	-7.6	-5.4	-7.9	-8.4	-7.9	-7.9
acc + tjit + traj	-5.4	-3.3	-6.6	-4.9	-4.6	-5.2

8.6 Monte Carlo results for trajectory reconstruction

In this section we consider the monte carlo events remaining after the two cuts discussed in the previous section.

The main error in the reconstructed core location lies along the line connecting HIRES and the core, which is generally close to the HIRES–MIA direction. Figure 8.6 shows the core error in the HIRES–MIA direction. The cores are systematically reconstructed closer to HIRES by about 30 meters. This is probably the result of not accounting for HIRES time slewing. Eliminating the bias would only slightly improve the N_μ statistical error, since the statistical core error would continue to affect N_μ reconstruction.

Figure 8.7 shows the difference in R_p reconstructed and input. Showers are reconstructed systematically closer to HIRES by $\sim$ 15 meters. Since $E \propto R_p$, the R_p reconstruction bias will result in an energy reconstruction bias of $15/\overline{R}_p \approx 15/3000 \approx 0.5\%$. Figure 8.8 shows the difference in reconstructed and input θ. This parameter is reconstructed to $\sim 0.6°$.

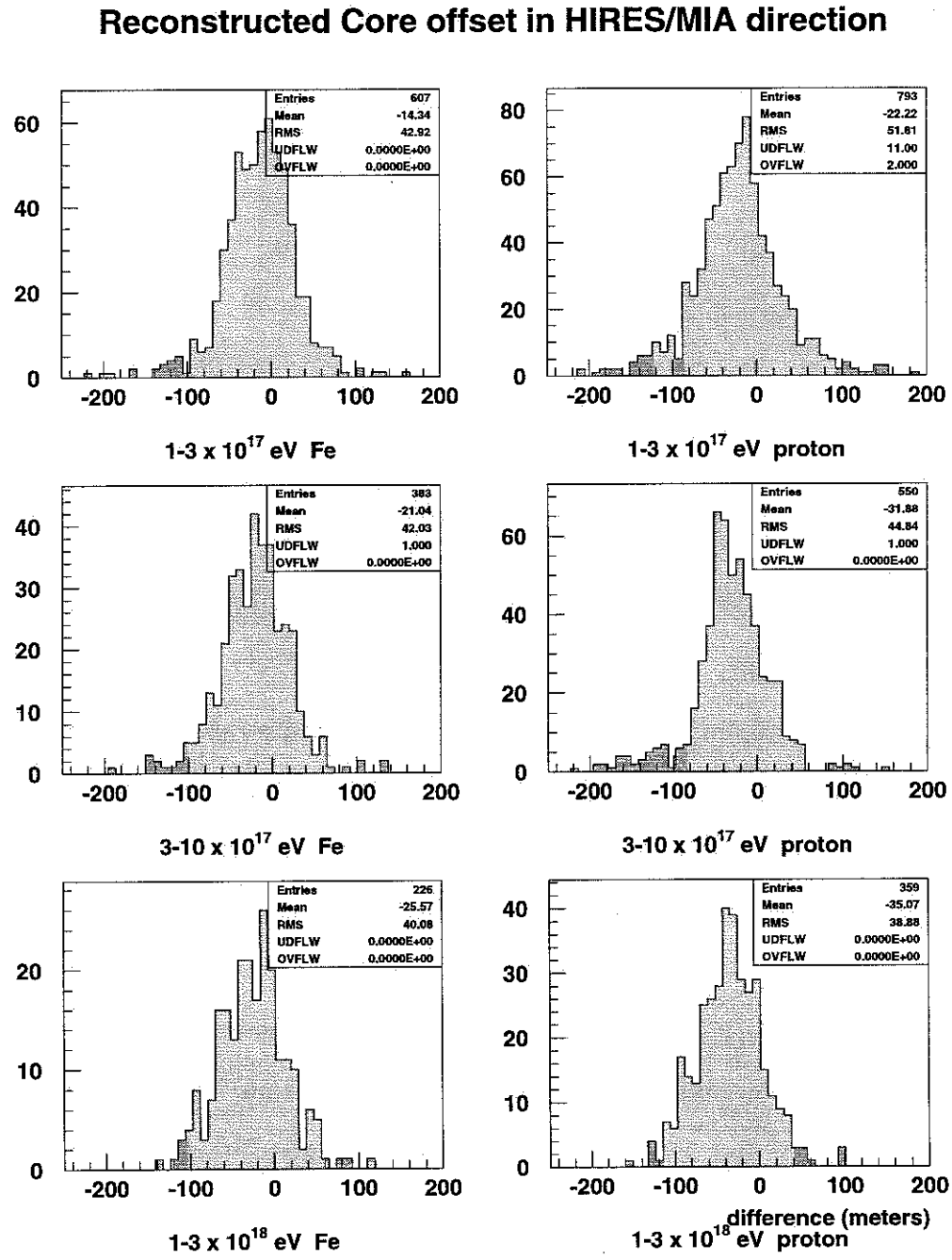

Figure 8.6: Difference between reconstructed and input core locations along the HIRES–MIA direction.

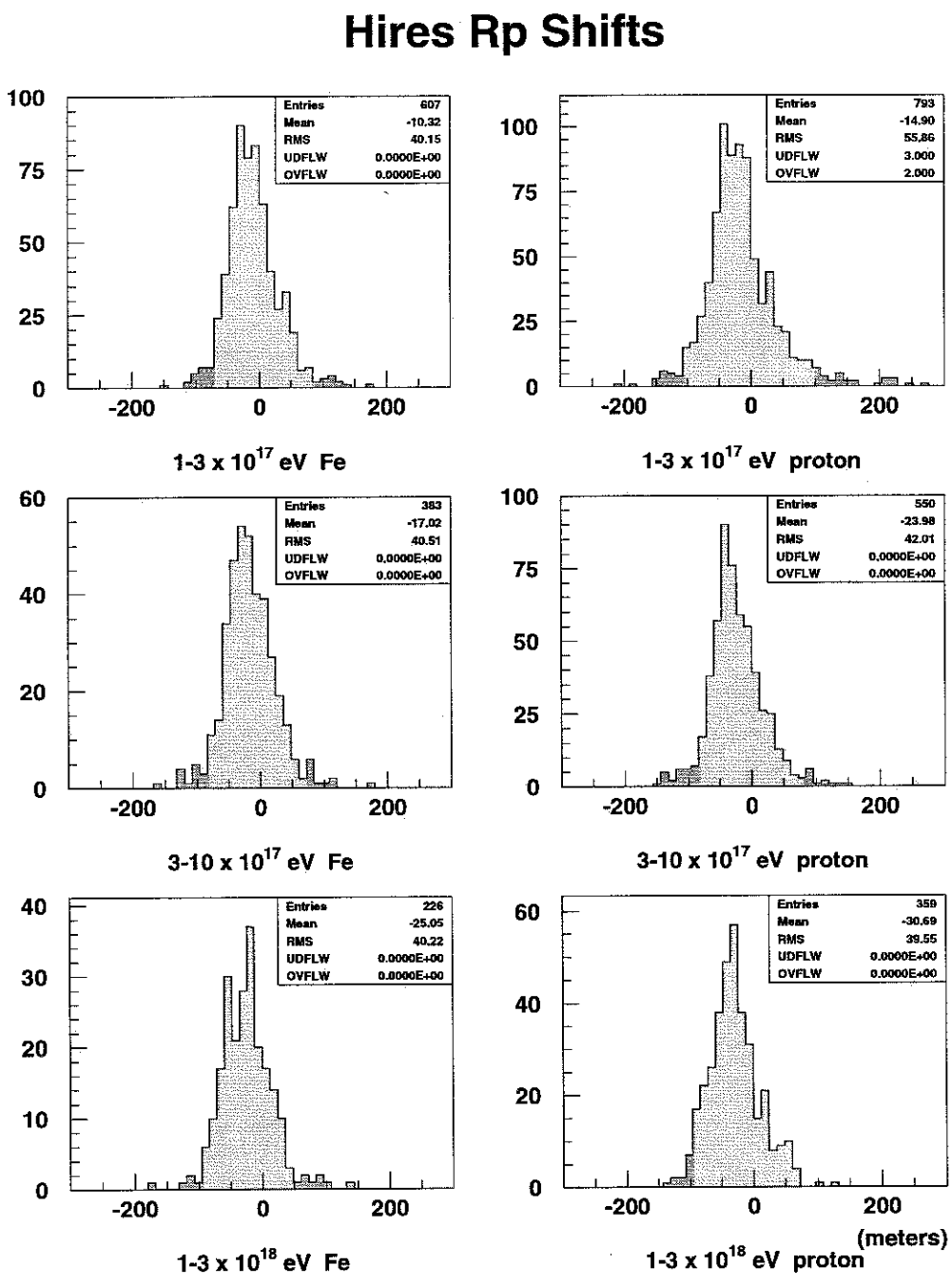

Figure 8.7: Difference between reconstructed and input R_p.

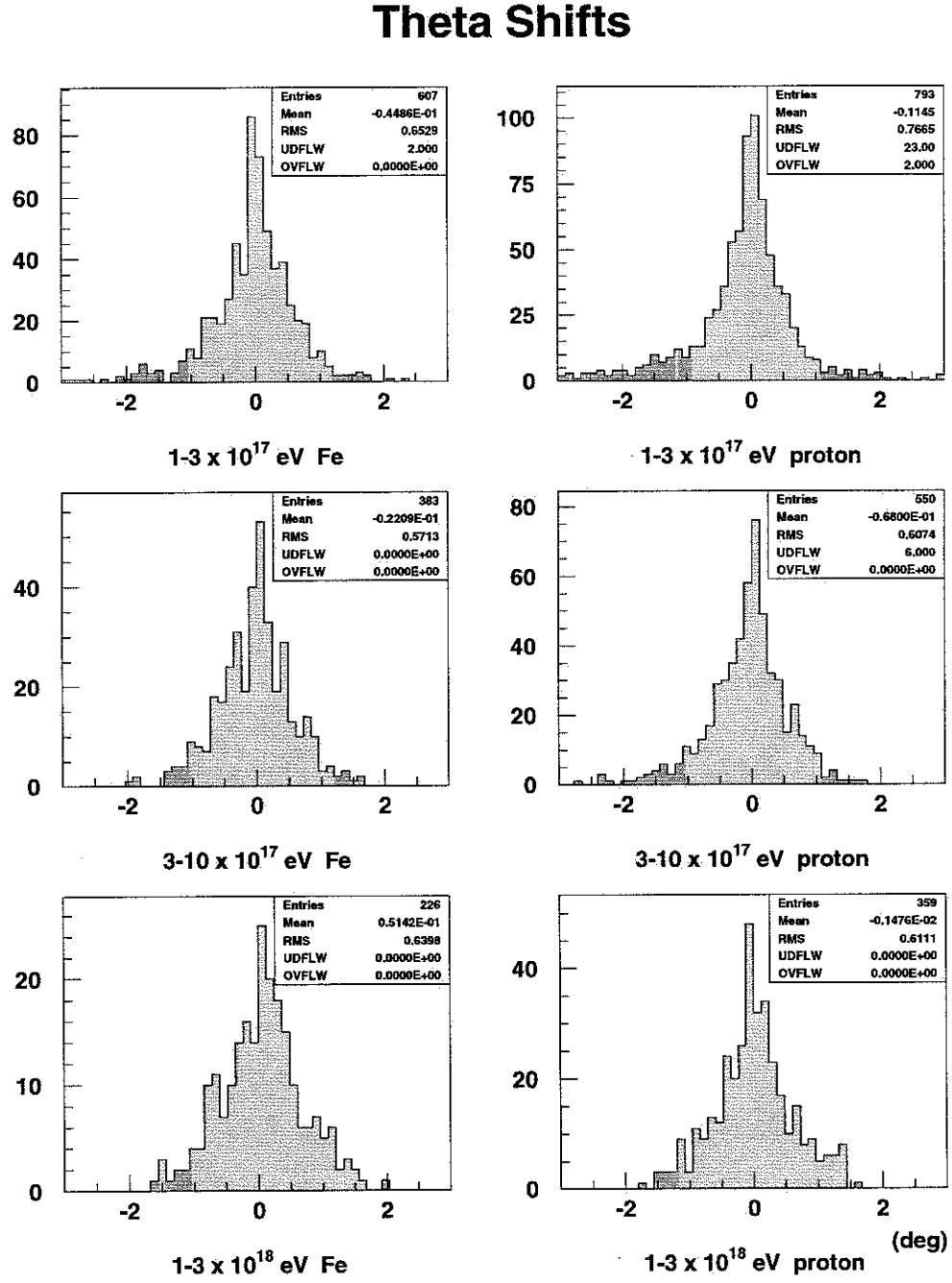

Figure 8.8: Difference between reconstructed and input trajectory theta.

8.7 Quality Cuts

It is desirable to cut on the statistical errors of the quantities of interest. Figure 8.9 shows three distributions following the application of the cuts suggested previously. The following cuts eliminate the obvious tails:

- Statistical $X_{\max}$ error less than 50 g/cm^2
- Statistical Energy error less than 20%
- Statistical $\log_{10}(N_\mu)$ error less than 0.15

These cuts eliminate 28% of the events remaining after the cuts in the previous section.

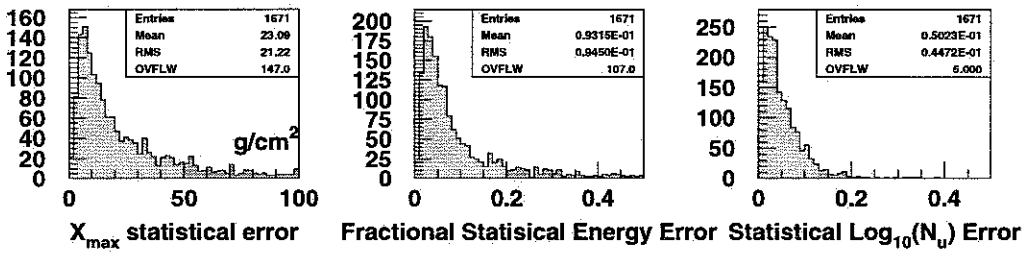

Figure 8.9: Distributions used as basis for Quality Cuts.

8.8 $X_{\max}$, $N_{\max}$, and Energy biases

The fitting done for $X_{\max}$, $N_{\max}$, and X_0 and the derived parameter Energy has been discussed in section 5.3.4. Possible atmospheric effects were also discussed and shown to be rather limited even under ridiculously extreme cases.

The presentation here covers systematic effects arising from the fitting method. For plane fitting and trajectory fitting, the length of the track in degrees was the major determination of how well the track could be reconstructed, with the number of measurements, i.e. the

number of tubes making a small contribution. For reconstructing the shower parameters, the grammage traversed by the visible portion, i.e. the part seen by the detector, is the natural limitation. For instance, even though a nearby shower at half a kilometer may span 60 degrees in the detector, it would only span about 90 g/cm^2. Such a shower would not be reconstructable for $X_{\max}$, $N_{\max}$, and X_0 . Another important issue is what part region of the shower is visible. It is far better to observe the region surrounding $X_{\max}$, where both the rise and fall of the shower can be seen, than to see only the rise or the fall. Extreme Cherenkov contamination presents another problem. When this is the case, the exact nature of the buildup of the Cherenkov beam becomes important. Since this depends strongly on X_0 , which is poorly determined, it is best to reject these events.

In the following discussion the MIA based cuts and the quality cuts have already been applied. There is almost no correlation between the MIA based cuts and the cuts discussed below. However, having applied the quality cuts does significantly reduce the reconstruction bias shown on several plots below.

Figure 8.10 shows some qualities of the dataset useful for interpreting the impact of the cuts to be proposed based on the monte carlo results.

Figures 8.11 and 8.12 show the reconstruction bias for $X_{\max}$ and Energy as a function of track length in gammage. There is limited monte carlo data below 300 g/cm^2, but what data exists, suggests there is an $X_{\max}$ bias in the important low energy range where most of the actual data lies. Besides acting as a bias cut, the track length cut acts as an additional quality cut by eliminating marginal events.

Figures 8.13 and 8.14 show the reconstruction bias for $X_{\max}$ and Energy as a function of the first visible point, X_F along the track before applying the track length cut. Figures 8.13 shows that a eliminating bias in the important low energy range means rejecting events with $X_F > 500$ g/cm^2. The growing $X_{\max}$ bias for larger values of X_F results from the fact that $X_{\max}$ is increasingly before or very near the edge of the visible region for

larger X_F. This makes accurate $X_{\max}$ reconstruction more difficult. In general there is an $X_{\max}$ reconstruction bias towards the visible part of the track.

The track length cut is essentially independent of the X_F cut and the Cherenkov cut below.

It is also sensible to cut on the last visible point, X_L. A reasonable cut is $X_L > 1100$ g/cm^2. Since there is a not unexpectedly strong correlation between X_F and X_L, this cut removes only 7% of the events that are not already removed by the track length and X_F cut.

Eliminating Cherenkov dominated events means eliminating events which are headed nearly directly towards the detector. The viewing angle for a tube is defined as the angle between the tube direction and the shower direction. Figure 8.15 shows the viewing angles for the first and last tubes along a track, V_F and V_L respectively. Since most tracks are first visible high in the atmosphere, V_F tends to be small. This alone does not usually indicate Cherenkov contamination because the Cherenkov beam has not become sufficiently strong at depth X_F. But tracks which have a small V_L will have small viewing angles along the entire track which imply a high Cherenkov contamination. The peak around 30 degrees in the V_L distribution is due to Cherenkov events. Examination of events shows that a cut of $X_F < 35$ degrees is reasonable.

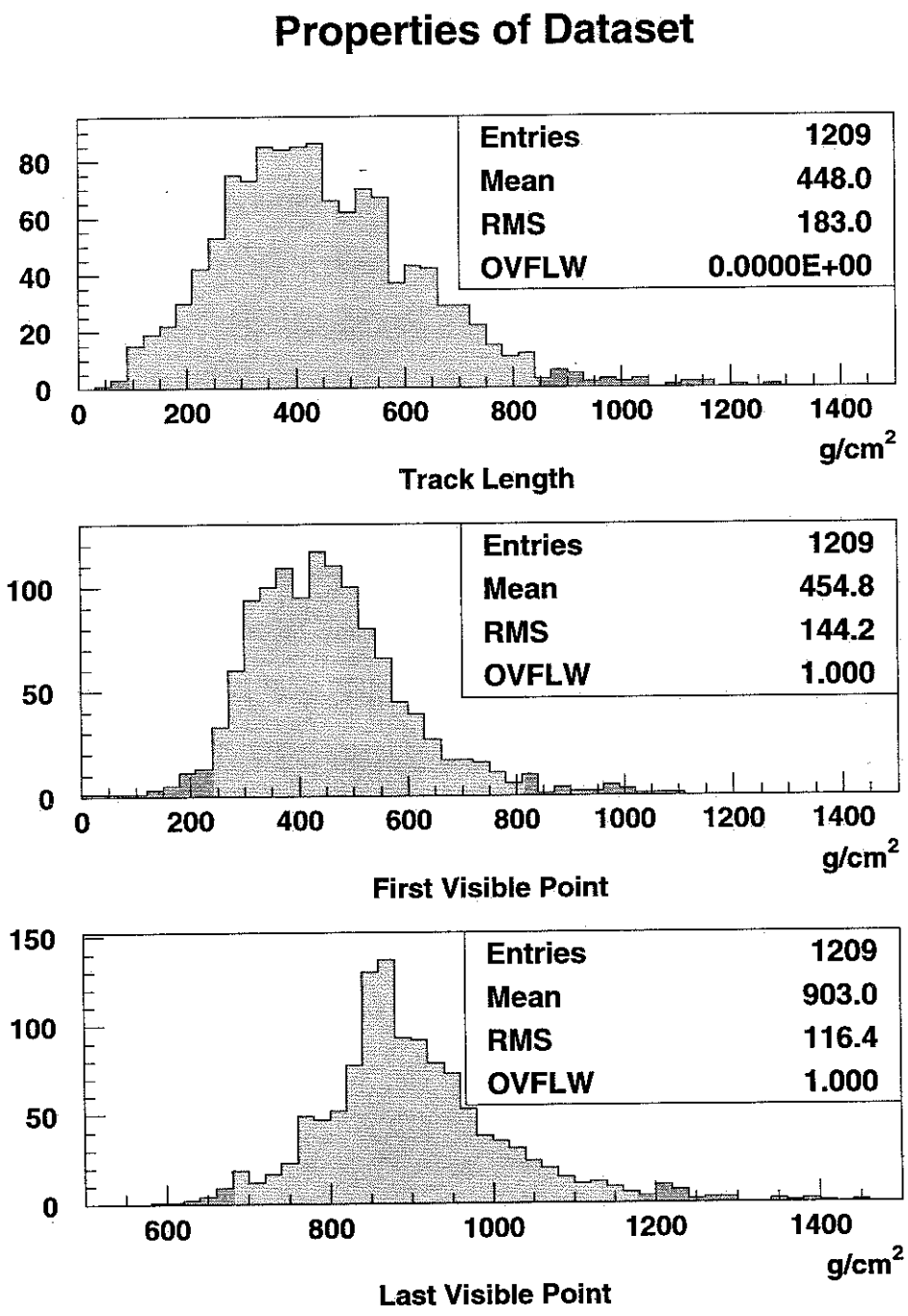

Figure 8.10: Distribution of track length, the first visible point, and the last visible point following MIA based cuts and quality cuts.

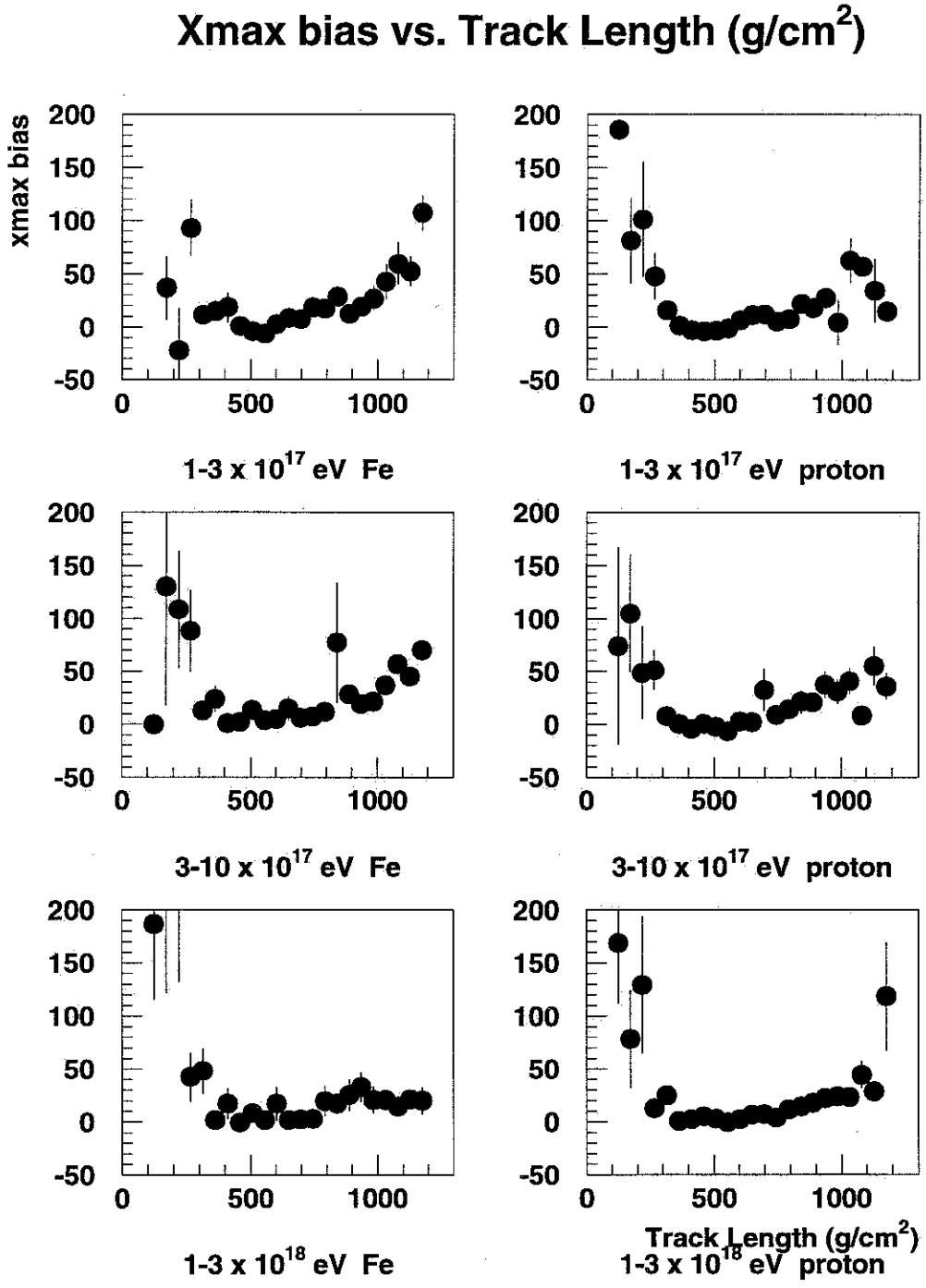

Figure 8.11: Difference between reconstructed and input $X_{\max}$ as a function of track length in grammage.

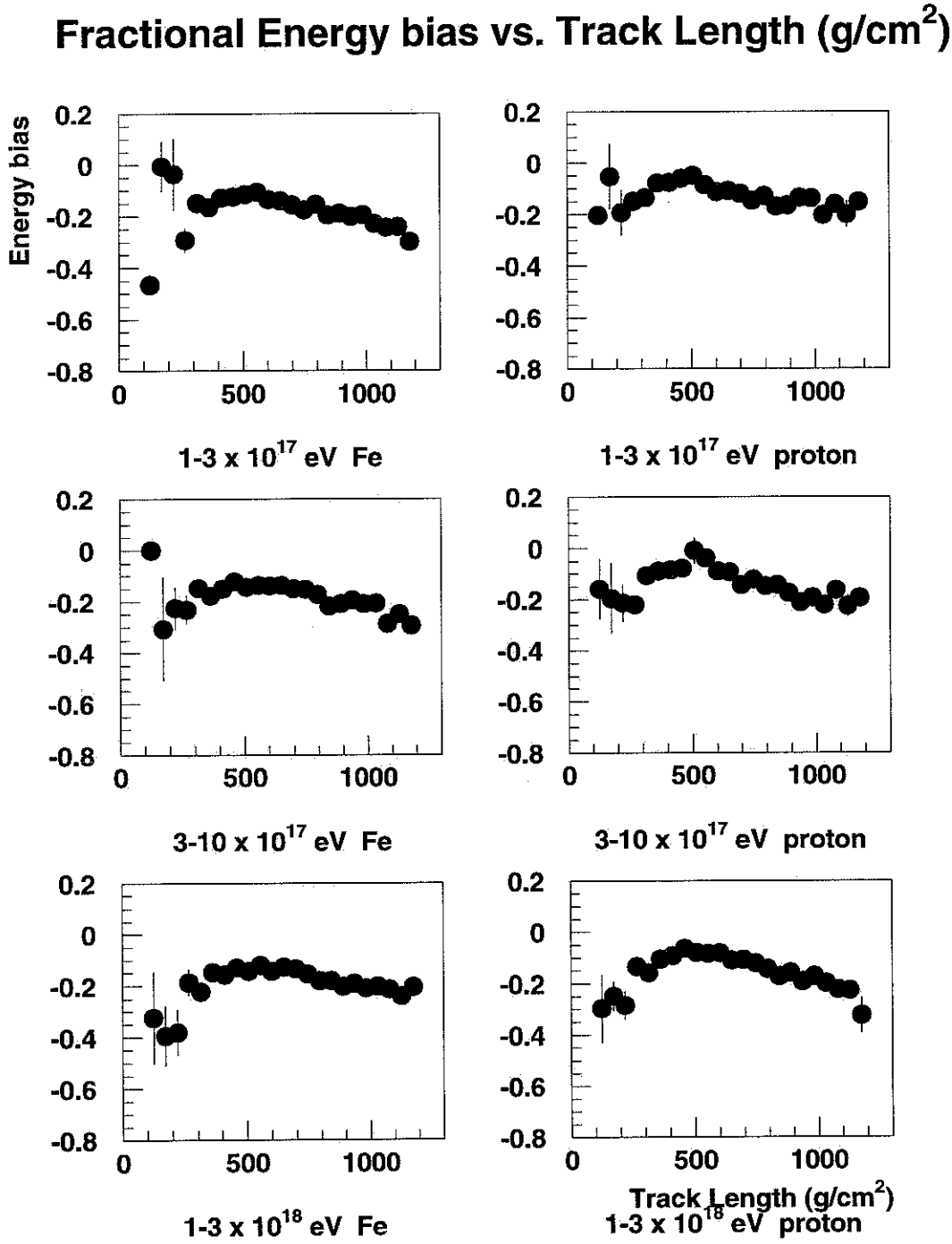

Figure 8.12: Difference between reconstructed and input Energy as a function of track length in grammage.

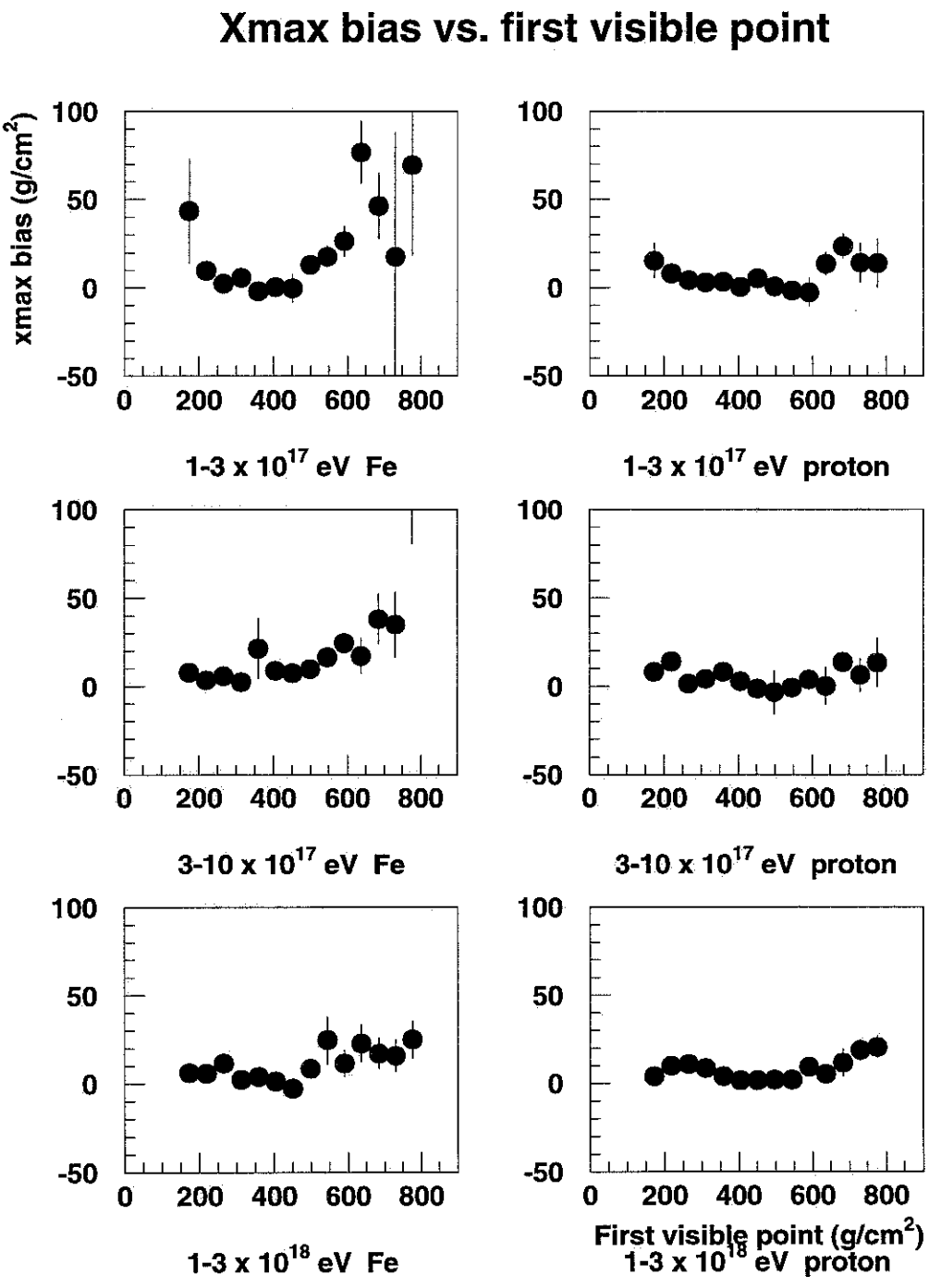

Figure 8.13: Difference between reconstructed and input $X_{\max}$ as a function of the first visible point in grammage.

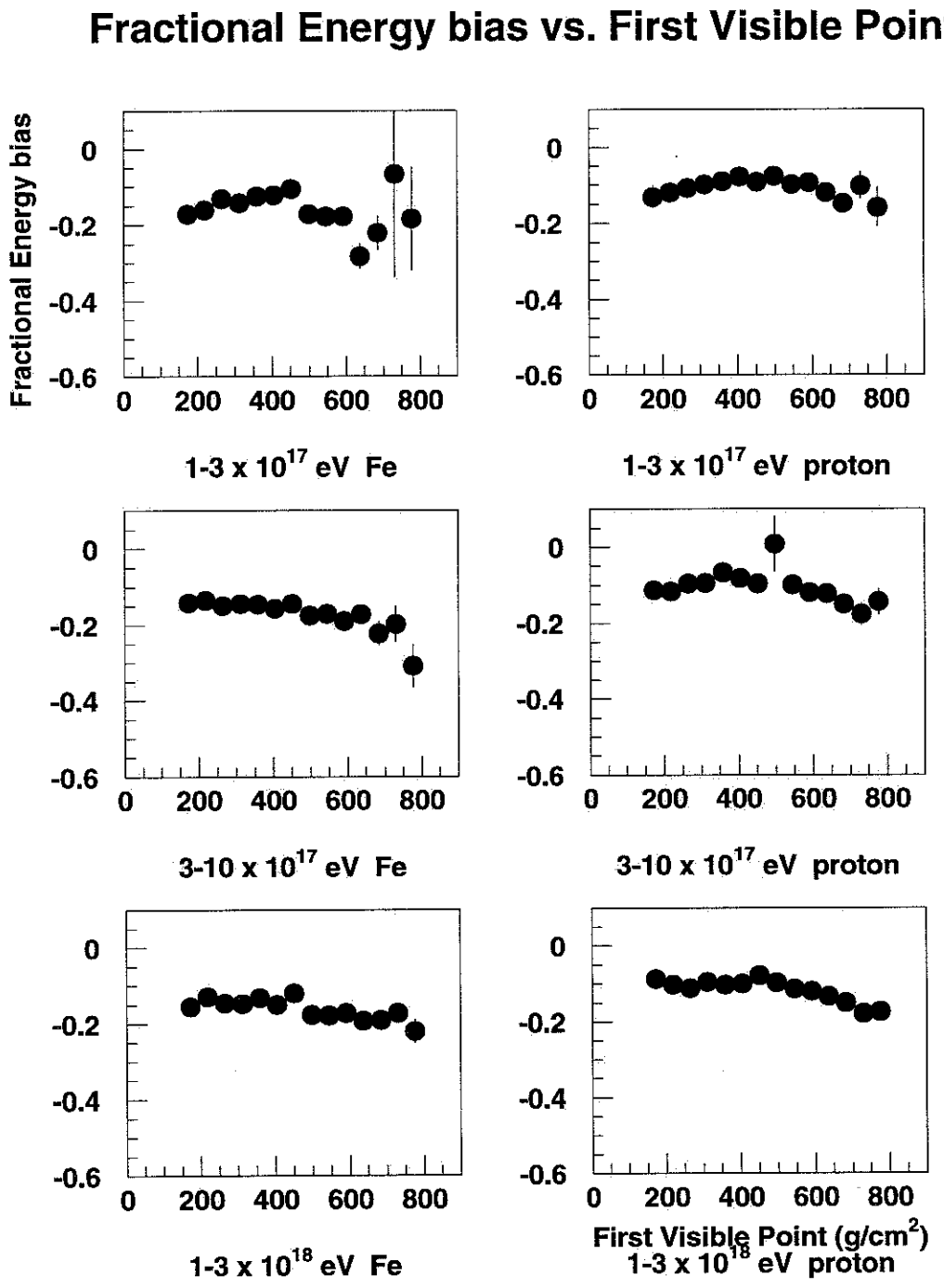

Figure 8.14: Difference between reconstructed and input Energy as a function of the first visible point in grammage.

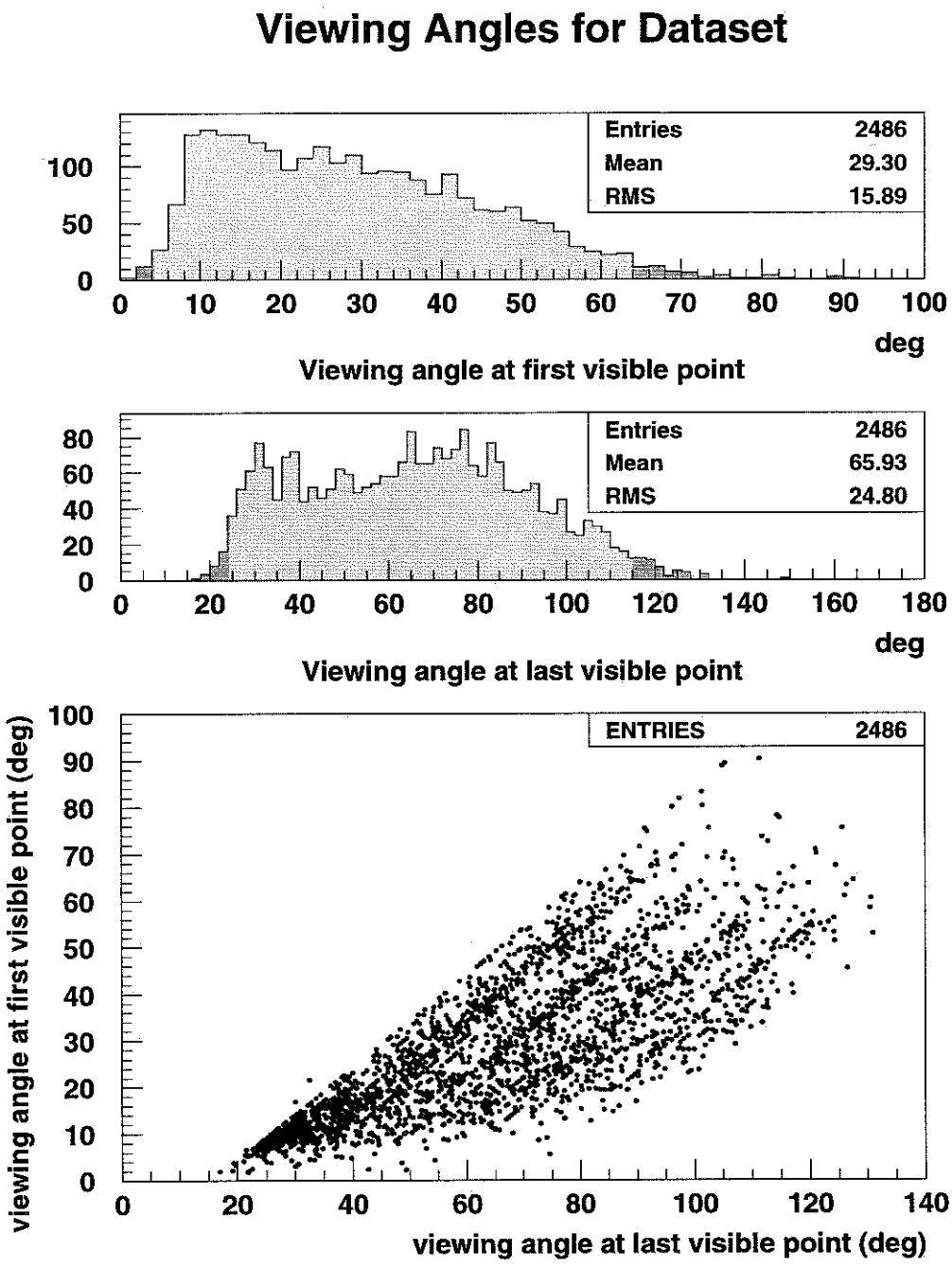

Figure 8.15: Viewing angles for the first and last visible points of each shower. The peak in the middle plot between 20 and 40 degrees is due to Cherenkov events. In the scatter plot, the sharp top diagonal is the result of the 15 degree track length cut. The banding effect is a trigger bias effect from triggering by mirrors.

8.9 Summary

The following is the full list of cuts which will be applied to the data before presenting physics results in the next chapter. They may be grouped as Basic cuts, MIA Antibias cuts, Qualtity cuts, and HIRES Antibias cuts. The Basic cuts are:

- 15 degree minimum track length
- 40 intime muon minimum for HIRES–MIA events
- 80 intime muon minimum for HIRES–MIA–CASA events
- Failed events

The failed events refer to problems encountered **hbrd_traj.run**, **gpln**, **bindata**, and **pfl**. This is an infrequent occurrence and is usually the result of a non coincident event masquerading as a coincident event. The Basic cuts leave 2516 events.
The MIA Antibias cuts are:

- Number of hit muon counters less than 700
- Shower core within 1000 meters of MIA center

After applying these cuts 1671 events remain.
The Quality Cuts are:

- Statistical X_{max} error less than 50 g/cm^2
- Statistical Energy error less than 20%
- Statistical $\log_{10}(N_\mu)$ error less than 0.15

After applying the these cuts, 1209 events remain.
The HIRES Antibias cuts are:

- Track length greater than 300 g/cm^2
- $X_F < 500$ g/cm^2
- Cherenkov cut: $V_L < 35$ degrees

There is almost no correlation between the MIA Antibias cuts and the HIRES Antibias cuts. Together these cuts leave 559 events. For this set of cuts, the monte carlo derived acceptance normalized to one at 1-3 $\times 10^{17}$ eV are shown in Table 8.7. The dependence on energy and composition remains small.

Table 8.7:

HIRES–MIA relative aperture			
	1–3 $\times 10^{17}$	3–10 $\times 10^{17}$	1–3 $\times 10^{18}$
"proton"	1.00	1.15	1.40
"iron"	1.15	1.25	1.13

The following are the systematic errors for N_μ :

- 5% reconstruction error
- 7% average counter efficiency uncertainty
- 2% counter turn on related uncertainty

The following are the systematic errors for Energy:

- 18% reconstruction error
- 13% fluorescense yield [44]
- 5% mirror reflectivity
- 2% standard tube calibration

Chapter 9

Physics Results

9.1 N_μ – Energy correlation

The N_μ– Energy correlation is very strong and evident even after only the Basic cuts. Figure 9.1 shows the correlation for both the Basic cuts and the full set of cuts. The best fitted line has a slope of 0.81 ± 0.03 (stat) with an intercept of 5.90 ± 0.05 (stat) ± 0.09 (sys) at 10^{17} eV. The dominant systematic error is due to an energy reconstruction bias. If this were understood, then the nitrogen fluorescence would become the dominant systematic and the systematic error would fall below 0.07.

The AKENO/AGASA group, relying on the 1 km^2 Akeno detector (A1) combines their N_e–E and N_e–N_μ relationships to obtain [40]:

$$\log_{10} N_\mu = (0.84 \pm 0.02) \log_{10} E - (8.38 \pm 0.35) \tag{9.1}$$

for data obtained in the range $10^{7.0} \leq N_e \leq 10^{8.5}$ which corresponds to $10^{16.5}$–$10^{17.8}$ eV. The slight $\sec\theta$ dependence of the N_e–N_μ relationship is taken for the case of vertical showers. This yields an intercept of 5.90 ± 0.35 at 10^{17} eV. We are solidly in agreement with their intercept and consistent with their slope.

Table 9.1 summarizes the slope and intercept found by experiments with at least 200 m^2 muon coverage. We are in serious disagreement with the Yakutsk data. It should be noted

that their errors are the statistical errors from the line fit and do not include systematic energy shifts.

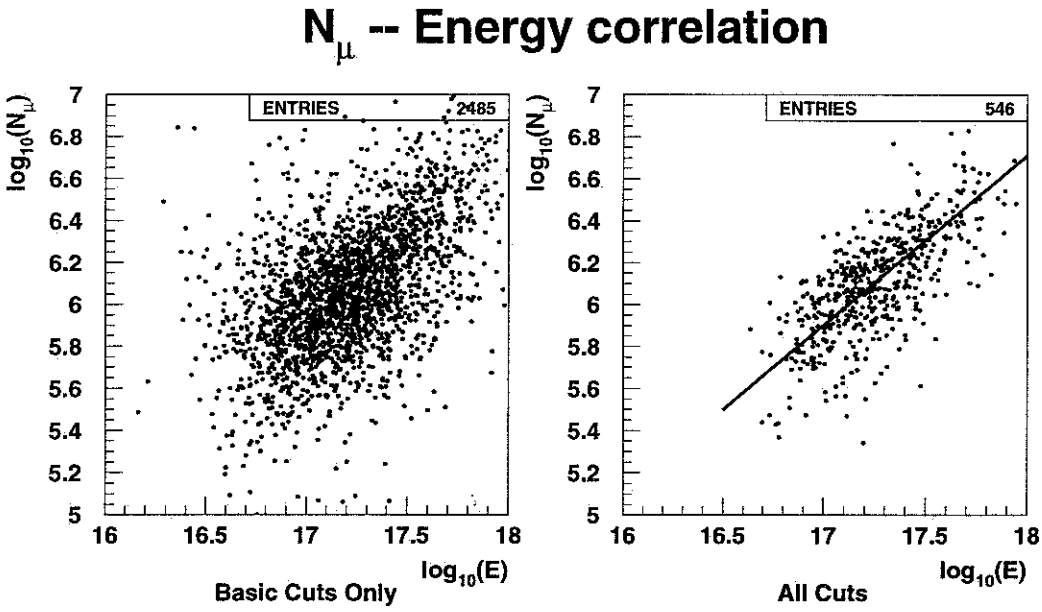

Figure 9.1: N_μ vs. Energy correlation

Table 9.1:

N_μ - **Energy relationships for several arrays**				
Detector	$\log_{10}(E(\text{eV}))$ intercept at 10^{17} eV	slope	Energy range $\log_{10}(E(\text{eV}))$	Threshold (GeV)
HIRES–MIA	$5.90 \pm 0.05 \pm 0.09$	0.81 ± 0.03	16.7–17.9	1.0
AKENO/AGASA [40]	5.90 ± 0.35	0.84 ± 0.02	16.5–17.8	1.0
Yakutsk [63]	5.64 ± 0.02	0.90	15.0–18.5	1.0
Yakutsk [63]	5.73 ± 0.01	0.90	15.0–18.5	0.3

9.2 Composition

Figure 9.2 shows the $X_{\max}$ – Energy correlation. It is not nearly as strong as the N_μ – Energy correlation. The relevant $X_{\max}$ distance scale is the nearly 100 g/cm^2 proton–iron

separation given by all three hadronic models, KNP, Minijet, and Statistical, discussed in chapter 3. Intrinsic shower fluctuations and statistical uncertainties in $X_{\max}$ can span half this range.

It is more revealing to bin the average $X_{\max}$ values as a function of energy as shown in Figure 9.3. In addition to the data points, reconstructed $\langle X_{\max} \rangle$ values are shown for monte carlo simulations of the detector which use proton and iron shower libraries generated assuming the KNP model. The $\langle X_{\max} \rangle$ reconstruction bias for the monte carlo showers is less than 5 g/cm^2 following the application of the same cuts that are applied to the real data.

The actual data consistently falls about 20–25 g/cm^2 below even the iron reconstructed KNP events. This is only partly understood. Assuming the minijet model or even the unlikely statistical model only leads to a greater discrepancy. However, in discussing the Fly's Eye results, Gaisser [36] points out that their KNP monte carlo produces systematic increases in $X_{\max}$ on the order of 10 g/cm^2 due to the use of Greisen's formula for modeling the electromagnetic component of the shower once particle energy falls below a certain threshold.

It is also possible that the detector is subject to an $\langle X_{\max} \rangle$ bias which affects the actual data more than the monte carlo data because the real data is subject to some degrading effects which are not fully incorporated in the detector monte carlo. Nevertheless, it is difficult to imagine a systematic $\langle X_{\max} \rangle$ shift of more than 20 g/cm^2 from such effects. Even a simulated bad survey of several mirrors leads to less than a 10 g/cm^2 shift.

The data clearly indicate a predominantly heavy composition over the entire experimental range $10^{16.8}$–$10^{17.8}$ eV. The elongation rate is 69 g/cm^2. This is slightly larger than the 52–60 g/cm^2 given by the various models for an unchanging composition. However, this does not indicate that the composition is getting lighter with increasing energy because at the same time the detector reconstructed $\langle X_{\max} \rangle$ for monte carlo events is also growing slightly faster than the input model $\langle X_{\max} \rangle$. The data indicates an unchanging composition.

Comparisons with the Fly's Eye results must be made with care because the Fly's Eye detector was subject to detector reconstruction biases which are not present for the HIRES–MIA experiment. In particular iron showers were reconstructed 23 g/cm^2 deeper in the atmosphere. Table 9.2 shows a comparison of HIRES–MIA derived $\langle X_{\rm max} \rangle$ data to adjusted Fly's Eye data, assuming an iron composition in the range of interest.

Even after accounting for this difference, Fly's Eye and the present $X_{\rm max}$ values disagree until $10^{17.8}$ eV. Besides a systematic shift, the shapes of the two E-$X_{\rm max}$ plots do not agree. Fly's Eye saw a sharp change in elongation rate from 30 g/cm^2 to 80 g/cm^2 at $10^{17.5}$ eV continuing to at least 10^{19} eV. They interpreted this as a lightening of the composition beginning at $10^{17.5}$. Physically this fit well with leaky box model discussed in chapter 2. The kink at $10^{17.5}$ is not present in the HIRES-MIA data. However, this does not rule out the leaky box hypothesis because a change in elongation rate may occur shortly after the energy region seen by HIRES–MIA. Measurements of the strength of the galactic magnetic field spread over a factor of 10. Also the conditions required for escape of locally produced cosmic rays depend on field orientation and point of production. Therefore, the leaky box hypothesis can not make an exact prediction of the energy at which high energy iron should leak out of the galaxy.

Table 9.2:

Comparison of HIRES–MIA and Fly's Eye $\langle X_{\rm max} \rangle$

Energy	$\langle X_{\rm max} \rangle$ (g/cm^2)		
($\log_{10}$(eV))	HIRES–MIA	Fly's Eye (adjusted)	Fly's Eye
16.8	554 ± 10	No data	No data
17.0	578 ± 5	600 ± 2	623 ± 2
17.2	587 ± 5	613 ± 1	636 ± 1
17.4	609 ± 9	618 ± 1	641 ± 1
17.6	617 ± 15	631 ± 1	654 ± 1
17.8	633 ± 32	636 ± 1	659 ± 1

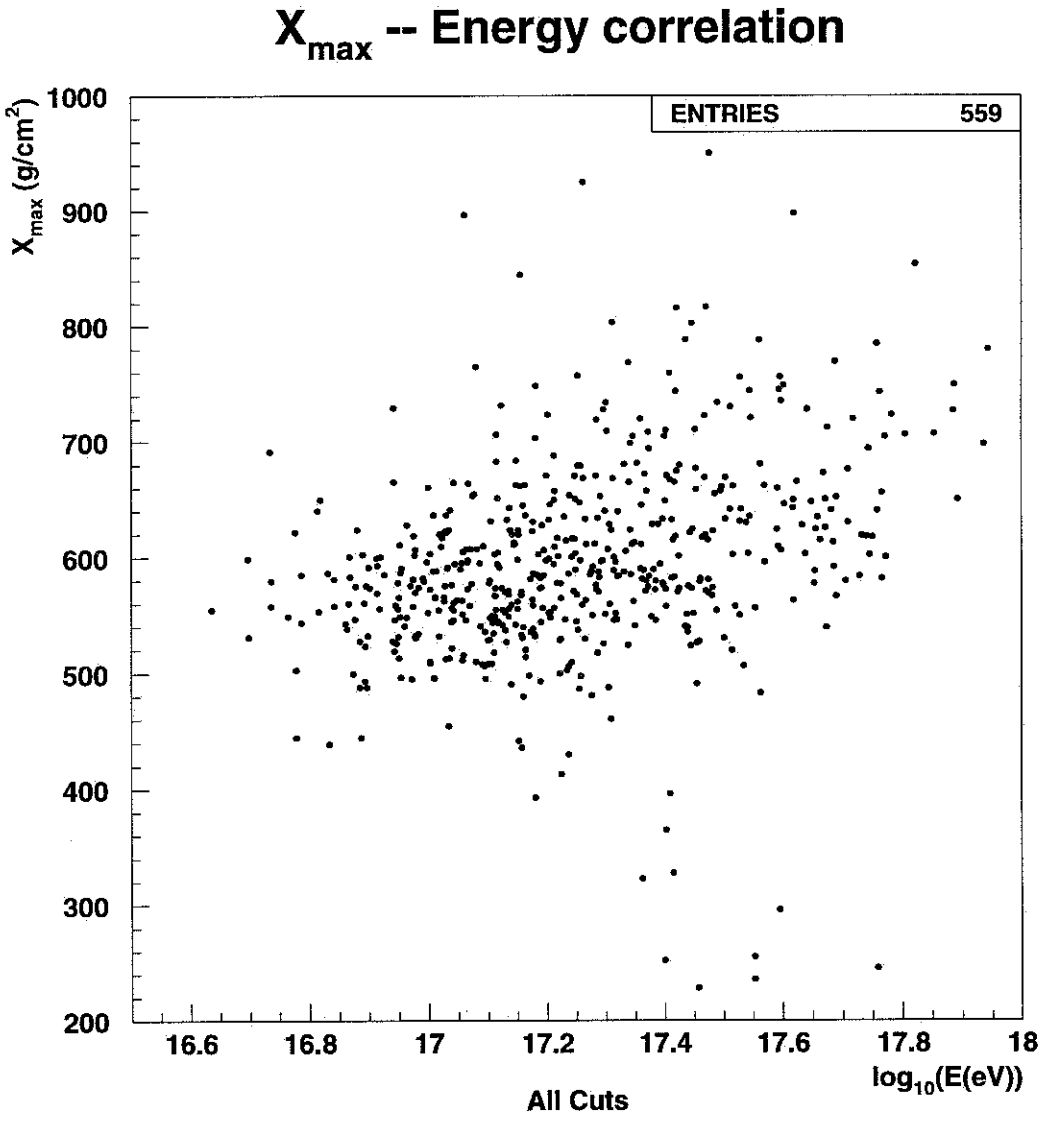

Figure 9.2: $X_{\max}$ vs. Energy correlation

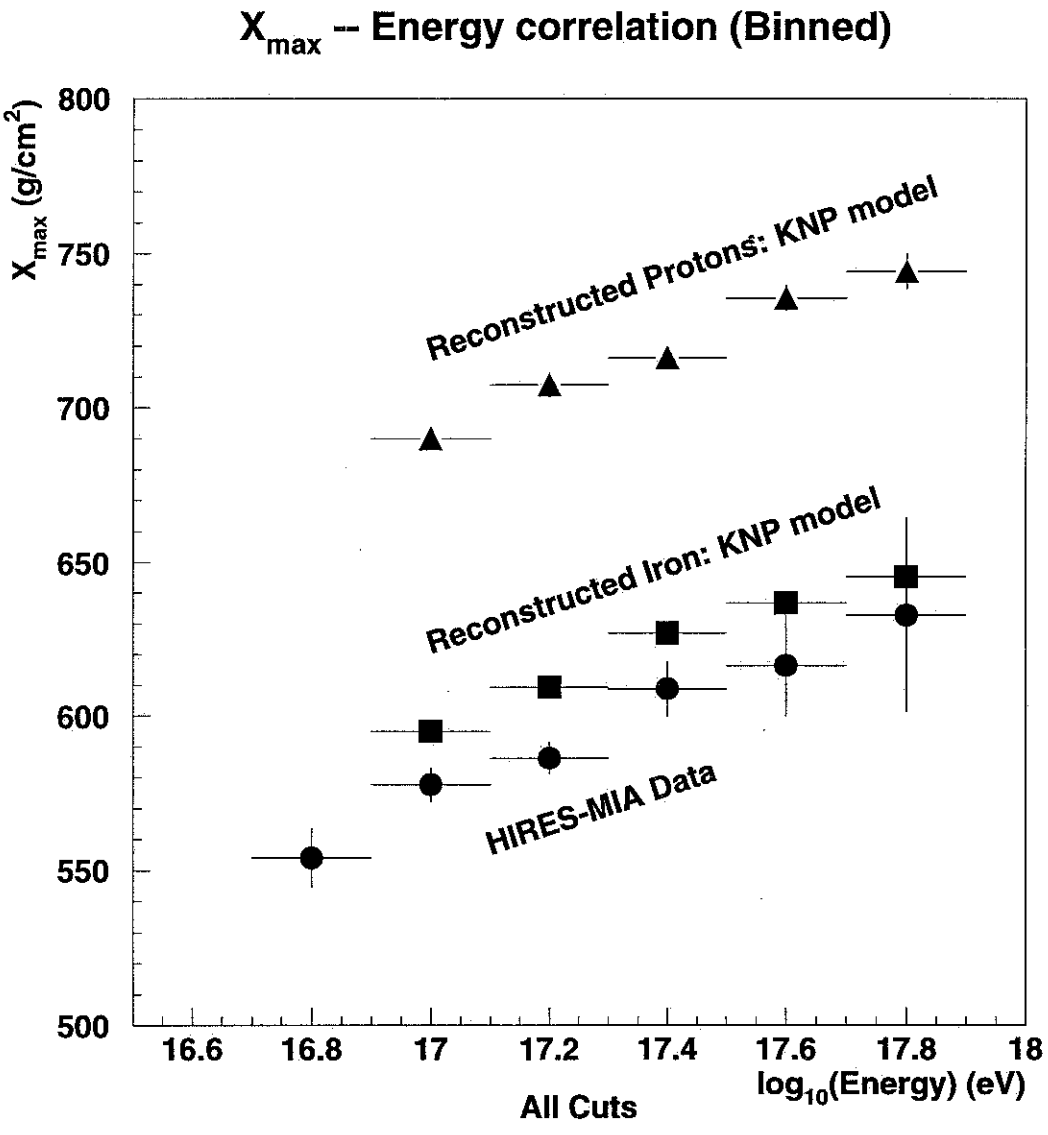

Figure 9.3: Binned $X_{\max}$ vs. Energy correlation. The circles show the data. The triangles and squares are from reconstructed monte carlo shower for pure proton and iron showers respectively. The monte carlo simulations use showers generated assuming the KNP hadronic model. The same cuts are applied to all three datasets.

9.3 $X_{\max} - N_\mu$ correlation

Figure 9.4 shows the $X_{\max} - N_\mu$ scatter plot, where all events have been adjusted to 10^{17} eV. The N_μ adjustment is made using the $N_\mu \propto E^{0.81}$ relationship found in section 9.1. The $X_{\max}$ adjustment is made assuming a composition neutral elongation rate of 55 g/cm^2. In principle this number depends very slightly on composition. As discussed in chapter 3, Gaisser [36] quotes composition neutral elongation rates of 60 ± 2, 55 ± 1, and 52 ± 2 g/cm^2 for the statistical, minijet, and KNP models in the energy range 10^{16}–10^{19} eV. Since the HIRES–MIA data spans little over a decade in energy, the average model dependence of the correction will be less than 3 g/cm^2. This is insignificant in the face of the $X_{\max}$ reconstruction error and the intrinsic shower fluctuations.

There is little evidence for a correlation based on heavier primaries interacting higher in the atmosphere (lower $X_{\max}$) and producing more muons at a fixed energy. This does not challenge existing physics arguments, because the predominance a heavy composition over the entire range of the dataset as evidenced in the previous section, precludes seeing the correlation if it exists. It is interesting that there is the barest hint of a light composition at greater average $X_{\max}$ and lower N_μ . Clearly greater statistics are needed before any firm conclusion can be reached.

9.4 Muon Lateral Distribution Function

The muon lateral distribution function (LDF) has long been of interest to researchers. Greisen [38] proposed his form in 1960 based on measurements out to 1000 meters by several early experiments [61, 24, 2]. Haverah Park made measurements [10] over the range 10^{15}–10^{20} eV reconfiguring their detector several times to cover the wide range of energies. A major limitation was that their muon coverage never exceeded 40 m^2. The Sydney Array (SUGAR) used the total muon number as an energy calibration. This in turn requires some knowledge of the LDF. The Yakutsk array has also measured the LDF in the range 10^{17}–10^{19}

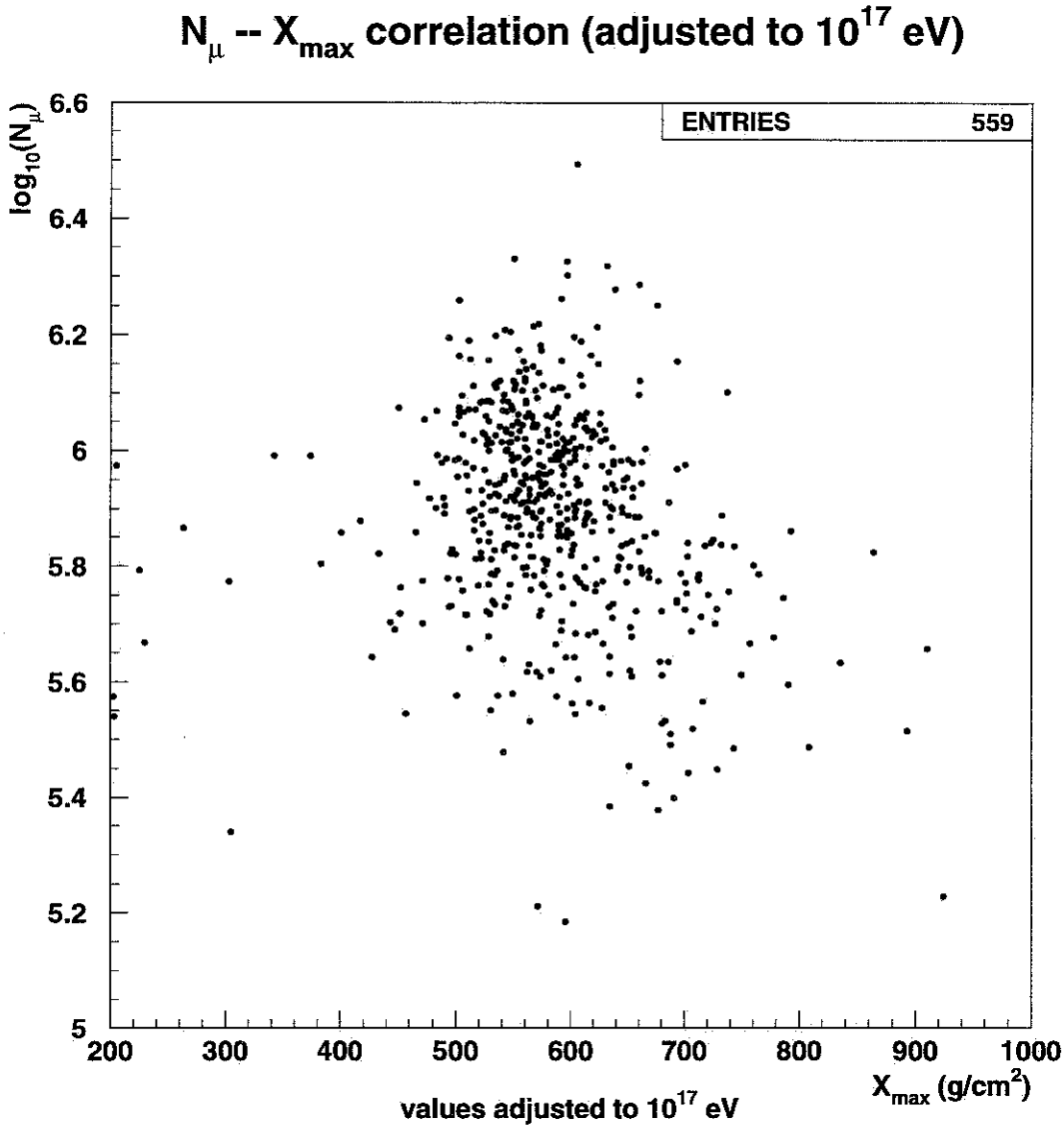

Figure 9.4: N_μ vs. $X_{\max}$ correlation. Events have been adjusted to 10^{17} eV.

eV [27] and later above 10^{19} eV [28]. Their muon coverage is 116 m^2. The AKENO/AGASA arrays, which were discussed in chapter 3, have a 454 m^2 muon coverage. This compares with the approximately 2000 m^2 usable MIA coverage. But this difference is not as great as it may seem because the AKENO/AGASA counters generate a signal proportional to the logarithm of the number of muons, while the MIA counters yield only a binary result.

Theoretically, the distribution gives some indication of the transverse momentum of the parent pions and kaons in the initial hadron interaction and the height at which the parent particles decay. Hillas [41] has shown that Coulomb scattering accounts for no more than 2% of the angular deflection. He also showed geomagnetic effects were insignificant except for highly inclined showers ($\theta > 60°$). For experimentalists, the lateral distribution is an important parameter in the design of large ground arrays. Previous measurements of the distribution have exclusively involved ground arrays, with the usual drawback of large event by event energy uncertainty. HIRES–MIA easily overcomes this limitation.

In order to measure the average LDF over many events it is necessary to normalize by the total number of muons in the event on an event by event basis. Using the N_μ found from the log likelihood to the AKENO form would result in a rather circular procedure that would bias the result. Therefore we use the HIRES determined energy for each event and the simple power law relationship between the HIRES energy and the total muon number found in section 9.1. number of muons for each event.

The region perpendicular to the shower core is divided into logarithmically equispaced annular bins. The number of live counters falling within each bin varies from shower to shower depending on the core location and trajectory. Computation of the perpendicular distance to each counter uses the trajectory found by the standard program which is based partly on muons taken from a carefully determined intime window. By contrast the muons used for computing the LDF are taken from a broader uniform 1000 nS window because the background is straightforward.

For each shower, a density is computed for each bin which has at least one counter hit during the intime window. After being normalized by the total number of muons, the value constitutes one measurement for the bin.

The density is computed based on the method described in section 8.2. Maximizing the log likelihood gives:

$$\rho_\mu = (-\log(1-f) - b)/A \tag{9.2}$$

where f is the fraction of alive counters which triggered in the bin, b is the background rate, and A is an effective area which factors in the decreased area seen by inclined showers and the average muon counter efficiency. A minimum measurable nonzero density, based on only one counter in a bin triggering, is also tracked so that possible minimum density problems can be monitored. This value varies from event to event according to the number of live counters counters in the bin. An error is found for each density measurement based on where the log likelihood value falls by 1/2.

Figure 9.5 shows the result for the final dataset. The AKENO and Greisen LDFs are also shown. It is clear that when the two functions depart significantly at larger radial distances, the data track the AKENO function quite well. The departure from both curves at small distances from the core is a saturation effect.

HIRES–MIA provides an excellent opportunity to test the energy dependence of the LDF. Figure 9.6 shows the result after dividing the dataset at the median energy of 169 PeV. The values of $\langle \log_{10} E \rangle$ for the two subsets are 17.05 and 17.49. Some energy dependence is evident but it is considerably smaller than the separation between the AKENO and Greisen LDFs. The mean minimum measurable density in each bin is also plotted. This does not cause a problem until the last bin, where it probably pushes up the low energy measurement. Beyond 1200 meters this effect dominates the density measurements making reliable measurements difficult if not impossible.

The dual energy range plot shows the effect of saturation at small distances more clearly. Not unexpectedly, the high energy sample is the most affected. To a small extent the breakaway is a result of the 700 muon counters cut made to obtain N_μ accurately. On average this cut removes events which would have nearly saturated annular bins. However, even if this cut is removed, most of the breakaway remains and is quite evident as well in monte carlo simulations. Without the cut, the high energy sample has average muon occupancies greater than 95% for the first three bins. This is typically only a couple of muons counters away from complete saturation.

It is also desirable to obtain the composition dependence of the muon LDF. Unfortunately the predominantly heavy composition and considerable $X_{\max}$ statistical errors do not allow this to be done in a statistical meaning manner.

9.5 Discussion

There has long been doubt about comparing results from the nitrogen fluorescence technique with those from ground arrays. This is a very important concern because the near term future exploration of cosmic rays above 10^{18} eV will be carried out with HIRES like detectors and the AGASA 100 km^2 (A100) ground array. It is expected that two fully instrumented HIRES detectors, separated by 12.6 km and operating in conjunction, will be online in one to two years. There is also current discussion about a 4 to 12 site HIRES in the vicinity of Dugway Provings Ground which would cover hundreds of square kilometers. Furthermore, the proposed Auger cosmic ray observatory will incorporate three fluorescence detectors.

The muon multiplicity results presented here show that HIRES and AGASA are obtaining consistent results even though the techniques used are quite different. In fact, the agreement between the two experiments is probably even better than indicated in table 9.1. Rather than working with N_μ and the difficult to determine energy, The AGASA collaboration prefers to use S(600) and $\rho_\mu(600)$, the charged particle density, and the muon density 600 meters from the shower core respectively. This is a common ground array technique. Hillas [35] argued on

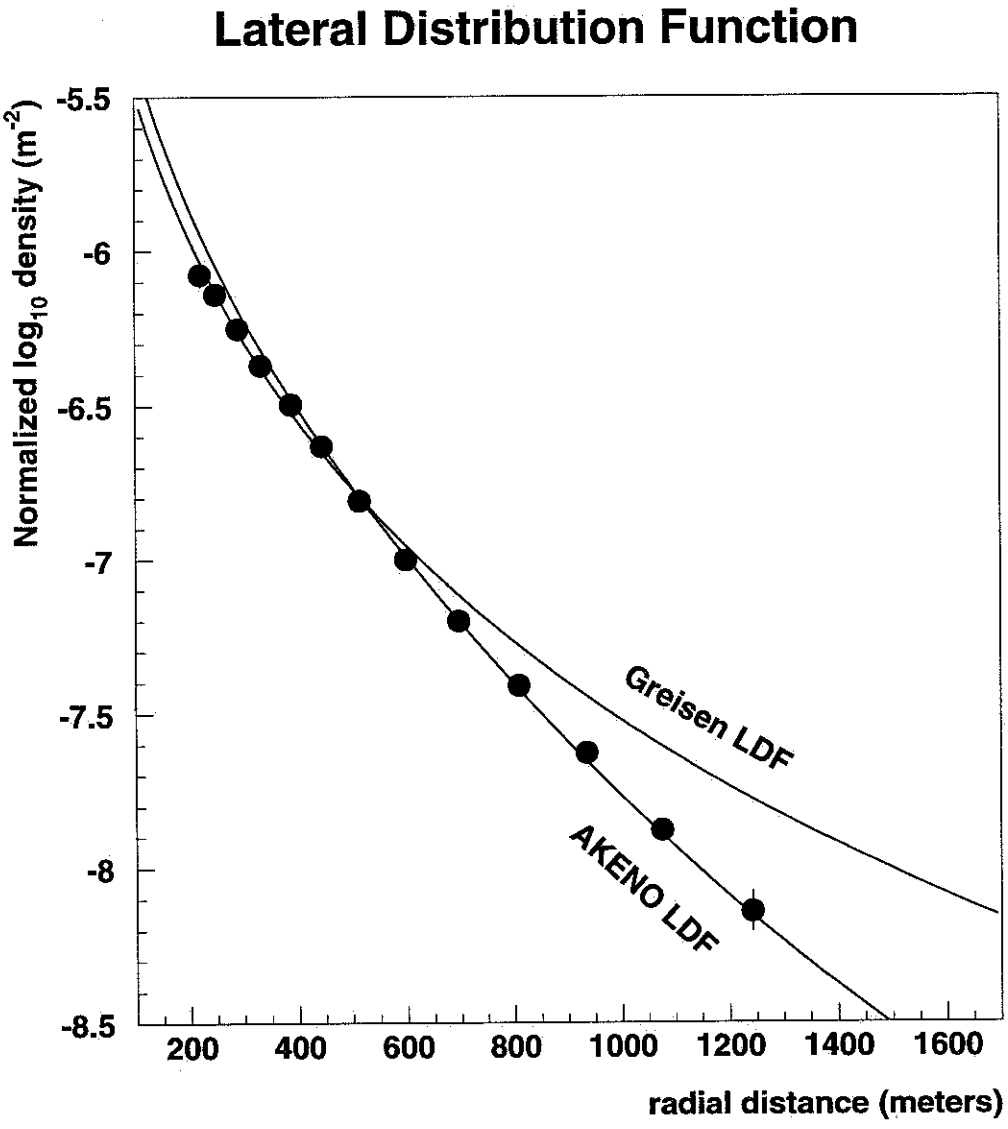

Figure 9.5: Muon Lateral Distribution Function derived from the normalized muon density. The Greisen and Akeno functions are shown for comparison.

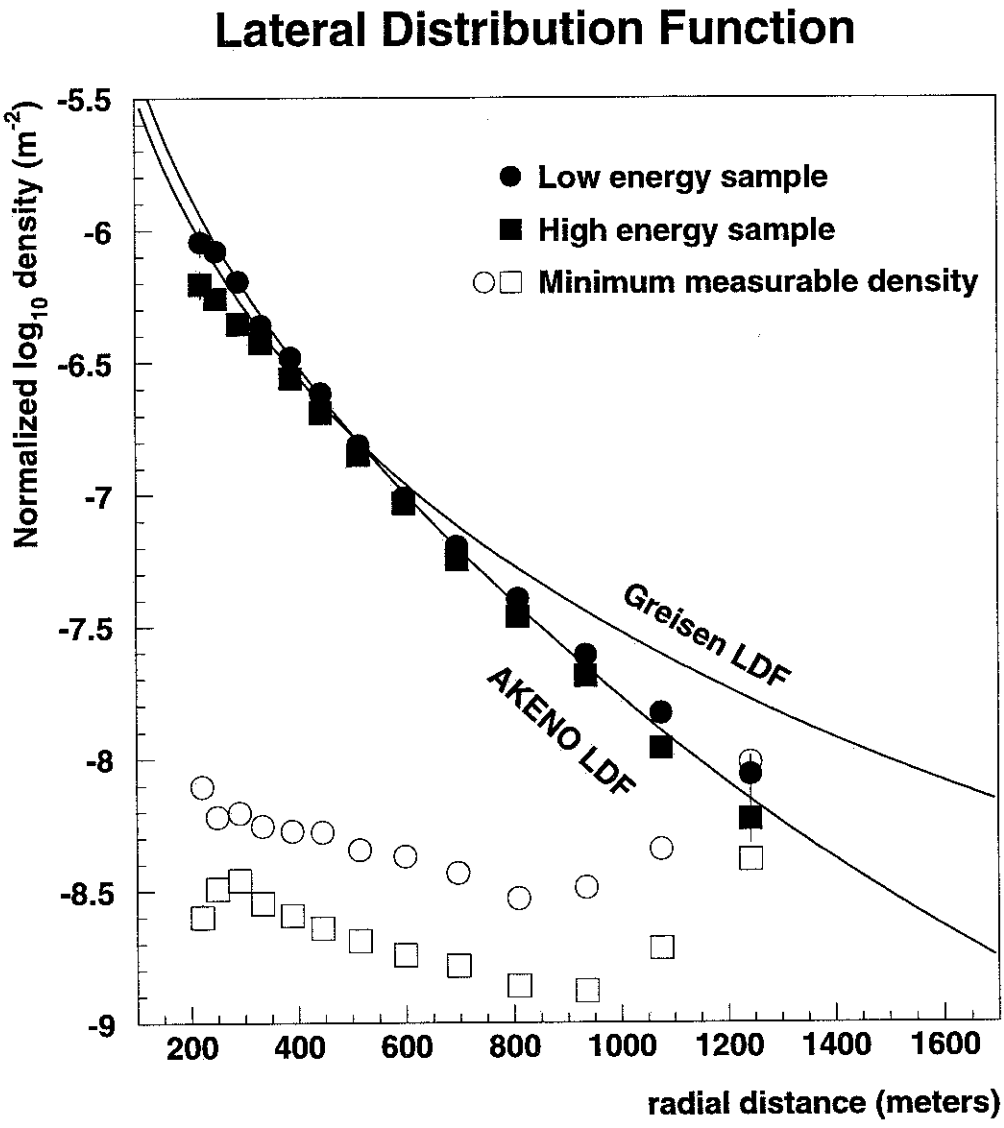

Figure 9.6: Muon Lateral Distribution Function as a function of energy. The low and high energy ranges include events below and above 214 PeV ($\log_{10}(E) = 17.33$) respectively. The minimum measurable density is also shown.

the basis of simulations that fluctuations in measured density should be minimized around 600 meters from the core. The Akeno/AGASA energy estimator is $E = 2.0 \times 10^{17}\ S(600)$ eV, where the S is in particles/m^2. For the A1 array they report:

$$\rho_\mu(600) = (0.16 \pm 0.01) \times S(600)^{0.82 \pm 0.03} \tag{9.3}$$

$$\Longrightarrow \rho_\mu(600) = (0.16 \pm 0.01) \times (5.0\ E(\mathrm{EeV}))^{0.82 \pm 0.03} \tag{9.4}$$

$$\tag{9.5}$$

Using this set of parameters their error bars are much smaller. At 10^{17} eV, the above formula gives $N_\mu = \rho_\mu(600)/\mathrm{LDF}(600) = 9.1 \times 10^5$; hence, $\log_{10} N_\mu = 5.95 \pm 0.03$. With the reduced errors, this is still very consistent with HIRES–MIA data. It indicates that S(600) is in fact a reasonable energy estimator for ground arrays.

Confirmation of the LDF has some implications for the proposed Auger array. The current design proposal calls for 10 m^2 water Cherenkov counters, hexagonally spaced 1.5 km apart. It will not be unusual for the nearest detector to be 800 from the core, where $\rho_\mu(800) = 4 \times 10^{-8}$ /m^2. For a 10^{19} eV shower, the nearest detector will detect an average of 13 muons provided the relationship found in section 9.1 holds up.

9.6 Summary

We find a clear correlation between the muon size and energy of showers in a one decade energy range centered around $10^{17.3}$ eV. The best fit has a slope of 0.81 ± 0.03 (stat) and an intercept of 5.90 ± 0.05 (stat) $\pm$ 0.09 (sys) at 10^{17} eV. Our slope and intercept are in agreement with the results found by the AKENO group.

Over the range $10^{16.7}$–$10^{17.9}$ eV, we find that the composition is predominantly heavy. This agrees with the basic Fly's Eye result. We do not see the kink at $10^{17.4}$ eV, where the Fly's Eye claims the composition begins to lighten. Although, there is some uncertainty regarding $\langle X_{\mathrm{max}} \rangle$ biases from the HIRES detector and some uncertainty regarding hadronic

model $\langle X_{\max} \rangle$ predictions, it seems very unlikely that the composition could be seen as predominantly light.

There is little evidence for a correlation between N_μ and $X_{\max}$. The predominantly heavy composition precludes the possibility of seeing a significant effect.

The measured muon lateral distribution function agrees well with the modification to the Greisen form proposed by the AKENO group based on their data. Our data is clearly inconsistent with the Greisen form. The measured energy dependence of the LDF is modest.

Bibliography

[1] U. Amaldi, *Fluctuations in Calorimetry Measurements*, Physica Scripta, Vol. 23, pp. 409–424, 1981.

[2] E. L. Andronikashvili and R. E. Kasarov, *Proc. Moscow Cosmic Ray Conf.*, **II**, pg 149–151, 1960.

[3] R. M. Baltrusaitis *et al*, *Arrival Direction of Cosmic Rays of* $E > 0.4$ *EeV*, App. J., **303**, pg 333–335, 1986.

[4] R. M. Baltrusaitis *et al*, *The Utah Fly's Eye Detector*, Nuclear Instruments and Methods in Physics Research **A240**, pg. 410–428, 1985.

[5] H. Bilokon, B. D'Ettorre Piazzoli, T. K. Gaisser, *et al*, *Monte Carlo Simulation of Muon Bundles in Underground Detectors*, 21^{st} ICRC, 1990, HE 4.5-6, pg. 366–369.

[6] D. J. Bird *et al*, *The Cosmic Ray Energy Spectrum Observed by the Fly's Eye*, Astrophysics Journal, **424**, pg 491–502, 1994.

[7] D. J. Bird *et al*, *The Calibration of the Absolute Sensitivity of Photomultiplier Tubes in the High Resolution Fly's Eye Detector*, Nuclear Instruments and Methods in Physics Research, **A349**, pg. 592–599, 1994.

[8] D. J. Bird *et al*, *Evidence for Correlated Changes in the Spectrum and Composition of Cosmic Rays at Extremely High Energies*, Physics Review Letters, Nov. 22, 1993.

[9] D. J. Bird *et al, The HiRes Fly's Eye Prototype Detector — A Status Report*, 23^{rd} ICRC, OG 10.2.4, pg. 462–465, 1993.

[10] P. R. Blake and W. F. Nash, *Muons in Extensive Air Showers: I. The lateral distribution of muons*, J. Phys G., **21**, pg 129–143, 1995.

[11] P. R. Blake *et al, Time Dispersion of Muons in EAS*, J. Phys G., **16**, pg 755–768, 1990.

[12] A. Borione, *et al.*, *A Large Air Shower Array to Search for Astrophysical Sources*, Nuclear Instruments and Methods in Physics, **A346**, pg 329–352, 1994.

[13] A. Borione, *et al.*, *A Search for Ultrahigh Energy Gamma–Ray Emission from the Crab Nebula and Pulsar*, Astrophysical Journal, May 20, 1996.

[14] A. Borione, *et al.*, Phys. Rev. D, **55**, pg 1714, 1997.

[15] A. Borione, *et al.*, 24^{th} ICRC, **2**, pg. 439, 1995.

[16] E. M. Burbidge, G. R. Burbidge, W.A. Fowler, F. Hoyle, *Synthesis of the Elements in Stars*, Rev. Mod. Phys, **29**, 4, pg 547–649, 1957.

[17] M. Catanese, *et al.*, *Constraints on gamma ray emission from the galactic plane at 300 TeV*, submitted to the Astrophysical Journal, 1997.

[18] S. N. Bozlev, *On the Multiplicity Fluctuations of High Energy Muons Generated by Primary Cosmic Ray Nuclei*, 22^{nd} ICRC, HE 4.2.2, pg. 556–559, 1991.

[19] A.N. Bunner, thesis, Cornell University, 1964.

[20] T. H. Burnett, *et al*, Nuclear Instruments and Methods in Physics Research, **A251**, pg 583–595, 1986.

[21] G. L. Cassiday, *Observatory for Ultra High-Energy Processes: The Fly's Eye*, Ann. Rev. Nucl. Part. Sci., **35**, pg 321–349, 1985.

[22] G. L. Cassiday *et al*, *The Muon Content of Extensive Air Showers*, 21^{st} ICRC, HE 3.4.1, pg. 94–97, 1989.

[23] M. A. Catanese, *A Search for Ultra–High Energy Gamma Rays from Active Galactic Nuclei*, Thesis, University of Michigan, 1994.

[24] G. Clark, *et al*, *Nuovo Cimento*, **8**, Suppl. 2, pg 623–652, 1952.

[25] G. Davidson and R. O'Neil, J. Chem Phys. **41** (1964) 3946.

[26] B. R. Dawson, *Some MOCCA Simulations of* 10^{19} *eV EAS*, private communication, July 1993.

[27] M. N. Dyakonov *et al*, *Results of Study of EAS Structure on Measurements of the EAS Different Components with* $E_0 = 10^{17}$–10^{19} *eV*, 20^{th} ICRC, HE 3.1-34, pg. 486–489, 1987.

[28] N. M. Efimov *et al*, *Lateral Distribution of Electrons and Muons in Giant EAS*, 22^{nd} ICRC, HE 3.3-3, pg. 339–342, 1991.

[29] J. W. Elbert, *Possible Experiments Using Fly's-Eye-Type Detectors With Other Detector Types*, Sofia Meeting on Cosmic Ray Cascades, 1980.

[30] J. W. Elbert and T. K. Gaisser, *Sensitivity of EAS Particle Fluxes to Primary Composition*, 16^{th} ICRC, **8**, pg. 42–47, 1979.

[31] G. N. Fowler, *et al.*, Phys. Rev D **35**, 870 (1987).

[32] T. K. Gaisser, *Cosmic Rays and Particle Physics*, Cambridge University Press, 1990.

[33] T. K. Gaisser, *Proceedings of Air Shower Workshop*, Bartol Research Institute, pg. 57, 1979.

[34] T. K. Gaisser and A. M. Hillas, 15*th* ICRC, vol 8, pg. 353, 1977.

[35] A. M. Hillas, *et al*, 12*th* ICRC, vol 3, pg. 1001, 1971.

[36] T. K. Gaisser, *et al*, *Cosmic-ray Composition around* 10^{18} *eV*, Phys Rev D, **47**, pg. 1919–1931, 1993.

[37] T. K. Gaisser and T. Stanev, *Mini-Jets in Minimum–Bias Events*, Physics Letters, 219B, pg. 375, 1989.

[38] Greisen, *Annual Review Nuclear Science*, **10**, 63, 1960.

[39] N. Hayashida, *et al*, *Characteristics of Giant Air Showers above* 10^{17} *eV*, 22^{nd} ICRC, 4, HE 3.3-1, pg 331–334.

[40] N. Hayashida, *et al*, *Muons* $\geq$ *1 GeV in large extensive air showers of energies between* $10^{16.5}$ *eV and* $10^{19.5}$ *eV observed at Akeno*, J. Physics G: Nuclear Particle Physics, **21**, pg 1101–1119, 1995.

[41] A. M. Hillas, *et al*, 11^{th} ICRC, **3**, pg. 533, 1970.

[42] M.H.A. Huang, *Anisotropy of Extremely High Energy Cosmic Rays*, thesis, University of Utah, 1996.

[43] P. J. Huber, *Robust Statistics*, Wiley, 1981.

[44] F. Kakimoto *et al*, *A Measurement of the Air Fluorescence Yield*, submitted to Nuclear Instruments and Methods, Nov. 1995.

[45] F. Kakimoto *et al*, *Longitudinal development of air-shower muons studied from the arrival time distributions measured at 900 m above sea level*, J. Phys. G, **12**, pg. 151–160. 1986.

[46] J. Knapp, D. Heck, G. Schatz, *Comparison of Hadronic Interaction Models Used in Air Shower Simulations and of their Influence on Shower Development and Observables*, Forschungszentrum Karlsruhe Report, FZKA 5828, 1996.

[47] J. J. Kolodziejczak, *The Gamma Ray Content of Ultra High Energy Cosmic Radiation*, Thesis, University of Michigan, 1990.

[48] B. Z. Kopeliovich *et al*, *Rising cross sections in QCD and the cosmic–ray data*, Physics Review D, 39, pg. 769, 1989.

[49] H. A. Krimm, *A Search For Point Sources of Ultra-High Energy Gamma Rays with an Emphasis on the Binary System Cygnus X-3*, Thesis, University of Chicago, 1991.

[50] G. b. Kristiansen, $19^{th} ICRC$, **9**, pg. 487, 1985.

[51] M. A. Lawrence, R.J.O. Reid, and A. A. Watson, *J. Phys. G*, **17**, pg 733, 1991.

[52] D. F. Liebling *et al*, *An investigation of cosmic–ray shower depths of maximum using the atmospheric Cherenkov pulse–width technique*, Journal of Physics G, 10, pg. 1283, 1984.

[53] J. Linsley, $19^{th} ICRC$, **9**, pg. 487, 1985.

[54] M. S. Longair, *High Energy Astrophysics*, Vol. 2, pg. 209–215, Cambridge University Press, 1994.

[55] N. Lund, *The Abundances in the Cosmic Radiation (The Elements Lighter than Ge)*, Cosmic Abundances of Matter, AIP Conference Procedings 183, pg 111, 1988.

[56] D. S. Matthewson and V. L. Ford, *Mem. R. Astron. Soc.*, **74**, pg 143, 1970.

[57] W. R. Nelson, H., Hirayama, and D. W. O. Rogers, *The EGS4 Code System*, SLAC–Report–265, 1985.

[58] D. Nitz, *Improvements to the muon selection and fit algorithms*, University of Michigan Astrophysics Memorandum, March 8, 1993.

[59] M. Pritchard, *Muon Counter Efficiencies*, UMC Group internal note, August 7, 1995.

[60] H. Rebel *et al*, *Arrival time distribution of muons from extensive air showers as signature of the mass composition of cosmic rays*, J. Phys. G, **21**, pg 451–472, 1995.

[61] B. Rossi, *Proc. Moscow Cosmic Ray Conf.*, **II**, pg 18–29, 1960.

[62] D. Sinclair, Nuclear Instruments and Methods in Physics, **A278**, pg 583, 1989.

[63] V. R. Sleptsova, *Characteristics of Low Energy Hadrons and Muons of* 10^{15}–$3 \cdot 10^{19}$ eV *at Different Atmospheric Levels*, HE 3.3-4P, 22^{rd} ICRC, 1991.

[64] P. Sokolsky, *Introduction to Ultrahigh Energy Cosmic Ray Physics*, Addison–Wesley, 1989.

[65] P. Sokolsky, *The Cosmic Ray Composition Above 0.1 EeV*, Highlight Talk, 23^{rd} ICRC, 1993.

[66] M. Teshima, in *Proceeding of the 23rd ICRC:: Invited, Rapporteur, and Highlight Papers*, eds. D. A. Leahy, *et al*, World Scientific Pub. Co. Pte. Ltd., Singapore, 257, 1994.

[67] U. of Utah, U. of Illinois, Columbia U., *Proposal to Construct a High Resolution EYE (HiRes) Detector*, NSF Proposal, 1990.

[68] University of Utah, *Proposal for Operating the Utah High Energy Cosmic Ray Observatory (Fly's Eye I, II, and HiRes)*, NSF Proposal, 1991.

[69] University of Utah, *Staged Construction Proposal for the High Resolution Fly's Eye (HiRes) Detector*, NSF Proposal, Sep. 10, 1993.

[70] A.A Watson, *A Review of Measurements Relating to the Origin of Cosmic Rays above* 10^{18} eV., Nuclear Physics B (Proc. Supple.) 28B, 1992.

[71] J. Wdowczyk and A. W. Wolfendale, *Nature*, **306**, pg. 347, Nov 24, 1983.

[72] M. M. Winn *et al*, *J. Phys. G*, **12**, pg 653, 1986.

Vita

Matthew John Kidd was born in Washington D.C. on October 19, 1969. Oceanography research at the Naval Research Lab during the summers of 1987 and 1988 led to his first publication in 1990. He obtained a B.S. in physics and mathematics from the California Institute of Technology in 1990. There he worked with Steve Schindler and Richard Mewaldt on the High Energy Isotope Spectrometer Telescope (HEIST) gaining his first experience with cosmic ray physics.